Dynamic Arterial Spin Labeling Measurements of Physiological Parameters

Permeability and Oxygenation

Dissertation
submitted to the
Combined Faculties for the Natural Sciences and Mathematics
of the Ruperto-Carola University of Heidelberg, Germany
for the degree of
Doctor of Natural Sciences

Johannes Gregori

Referees:
Prof. Dr. Matthias Günther
Prof. Dr. Josef Bille

Heidelberg 2009

--- für Dorothee ---

Thema

Arterial Spin Labeling (ASL) ist eine Technik der MR-Bildgebung, welche es ermöglicht, ohne Kontrastmittel lokal die Gewebeperfusion bzw. Durchblutung des Gehirns zu messen. Dabei wird einfließendes Blut markiert, indem die Magnetisierung der Wassermoleküle im Blut invertiert wird. Während das Blut durch den Gefäßbaum und in das Kapillarbett strömt, kann das Signal zu verschiedenen Einflusszeiten gemessen werden. Dabei zerfällt die Magnetisierung mit T1. Ein noch nicht eingehend untersuchter Aspekt dieser Technik ist es, das Perfusionssignal auf weitere dynamische Änderungen während des Einfließens hin zu untersuchen. In der vorliegenden Arbeit wird die dynamische Entwicklung des Perfusionssignals bezüglich der Parameter T2 und T2' untersucht. Die dazu verwendeten Auslesesequenzen wurden im Rahmen der Arbeit entwickelt: eine 3D-GRASE Auslese mit variabler Echozeit für die T2-Bestimmung sowie eine Spin/Gradienten Doppelecho-Doppelspiral 3D-GRASE Auslese zur Bestimmung von T2'. Des Weiteren wurde ein Modell entwickelt, das die Entwicklung des Perfusionssignals in Abhängigkeit der Einflusszeit sowie der Echozeit beschreibt, unter Berücksichtigung der kapillaren Permeabilität. Mit den gewonnenen Daten ist es möglich, direkt lokal die Wasser-Permabilität der Kapillarwand abzuschätzen. Die erhobenen T2'-Daten ermöglichen eine Abschätzung der dynamischen Änderung der Oxygenierung in der direkten Umgebung der Blut-Wasser-Spins. Die Doppelecho-Spiralsequenz in Verbindung mit einer ASL-Sequenz ermöglicht die simultane Bestimmung von Perfusion und Oxygenierung und ist daher prädestiniert für einen Einsatz in der funktionellen Bildgebung. Beide Techniken erlauben tiefe Einblicke in grundlegende lokale Aspekte der Physiologie.

Abstract

Arterial Spin Labeling (ASL) is an MR imaging technique which can measure the brain perfusion locally without contrast agent. The inflowing blood is labeled by inverting the magnetization of the water molecules. During the blood flow through the vascular tree and the capillary bed, the signal can be acquired at different inflow times. Thereby, the signal decays with T1. An aspect which has not yet been investigated is the dynamics of further MR parameters during the inflow. In the present work, the dynamics of the parameters T2 and T2' of the perfusion signal are investigated. The employed MRI sequences have been developed and are presented in this thesis: a 3D-GRASE readout with variable echo time for T2 quantification, and a spin/gradient double echo double spiral 3D-GRASE readout for T2' estimation. Further, a model has been developed which describes the behavior of the perfusion signal which includes permeability, depending on the echo time. With the acquired data it has been possible to directly derive an estimate for the local water permeability of the capillary wall. The T2' data allows an estimation of dynamical changes of oxygenation and local apparent venous volume in the direct vicinity of the inflowing blood water spins. The double echo spiral sequence in conjunction with ASL can in principle acquire perfusion and oxygenation simultaneously and is therefore predestined for functional imaging applications. Both techniques allow deep insights in basic local perfusion mechanisms.

Table of content

Table of content 8

List of figures 11

List of tables 16

1 Preface 17

1.1 Content 19

2 Theory 20

2.1 Magnetic Resonance 20

2.1.1 The spin in a magnetic field 20

2.1.2 RF pulses 22

2.1.3 The Bloch equations, T1 and T2 24

2.1.4 Solutions to the Bloch equations 25

2.1.5 T2’ and T2* Relaxation 28

2.1.6 The spin echo 28

2.2 MR imaging and readout techniques 30

2.2.1 Spatial encoding 30

2.2.2 Image reconstruction and k-space formalism 33

2.2.3 Gradient echo and spin echo sequences 36

2.2.4 EPI – Echo Planar Imaging 38

2.2.5 3D-GRASE: Gradient and Spin echo 40

2.2.6 SEPI: Spiral Echo Planar Imaging 41

2.3 Arterial Spin Labeling 45

2.3.1 Two basic techniques: Continuous and Pulsed Arterial Spin Labeling 45

2.3.2 Blood flow and perfusion: the General Kinetic Model 47

2.3.3 Magnetization Transfer: STAR and FAIR 48

2.3.4 Background suppression 50

2.3.5 Effect of varying BAT and Q2TIPS 51
2.3.6 An optimized pulsed ASL labeling and readout scheme 53
2.3.7 ASL time series 54
2.4 Advanced physiological perfusion aspects 56
2.4.1 ASL two-compartment models 56
2.4.2 BOLD: the effect of deoxygenated venous blood on R2' 60

3 ASL and T2: blood water transfer time and blood brain barrier permeability 67

3.1 Theory: Derivation of a two compartment perfusion model including T1 and T2 decay 68
3.1.1 T1 dependent signal evolution 68
3.1.2 T2 dependent signal evolution 71
3.2 Methods: Development of the modified 3D-GRASE-readout module for T2 quantification 78
3.2.1 Modified 3D-GRASE for T2 measurement 78
3.2.2 Stimulated echoes 79
3.3 T2 measurement protocols and trials 81
3.4 Perfusion quantification 83
3.5 Results: Blood water transfer and blood brain barrier permeability 85
3.6 Possible sources of error 93
3.6.1 Bolus dispersion 94
3.6.2 Partial volume effects 95
3.7 Summary 96

4 ASL and T2': dynamic blood oxygenation measurements 99

4.1 Theory: R2' oxygenation dependence at 3 Tesla 99
4.2 Methods: Development of a Spin/Gradient dual echo double spiral 3D-GRASE readout module for T2' quantification 102
4.3 T2 star measurement protocol and trials 104
4.4 Data processing and evaluation 105
4.4.1 R2' contrast and OEF calibration 105

4.4.2 Temporal preprocessing 108

4.5 Results: Dynamic blood oxygenation measurements 110

4.6 Summary 114

5 General Summary and Conclusion 116

5.1 ASL T2: Permeability measurements 116

5.2 ASL T2': Oxygenation measurements 117

5.3 Outlook: clinical applications 117

Appendix A: Physiology 119

A.1 The vascular tree 119

A.2 The Blood Brain Barrier 121

A.3 Brain tissue 122

Appendix B: T1, T2 and T2* values 123

B.1 T1 values 123

B.2 T2 values 125

B.3 T2* values 127

References 128

Software References 133

Acknowledgements 134

List of figures

Fig. 1: Theoretical signal decay in IR (upper) and FID (lower) experiments. T1=800 ms and T2=100 ms have been chosen. 27

Fig. 2: Schematic plot of the $M_{\perp}$ magnitude part (green). The blue line indicates pure T2 decay. A refocusing pulse is applied at TE/2, a spin echo formed at TE. 29

Fig. 3: Encoding scheme with: Slice encoding G_z simultaneously to the rf preparation pulse, phase encoding G_y, frequency encoding G_x simultaneously to the readout. Letters refer to Fig. 5. 32

Fig. 4: Two-dimensional k-space acquisition; the corresponding fourier transform is a T2-weighted brain image 35

Fig. 5: Concept of spatial encoding in two dimensions in k-space, and acquisition of one Fourier line (red): Beginning in the k-space center A, the phase encoding gradient prepares the coordinate k_y (B). Before the readout, a gradient in the negative k_x direction prepares C in k-space. The readout gradient sweeps the system to E. Simultaneously, signal is acquired at discrete time points (red arrow). The k-space center is reached again during readout at D, where a gradient echo can be observed. For the encoding gradients, cf. Fig. 4. 36

Fig. 6: Schematic drawing of a spin echo (a) and a gradient echo sequence (b), taken from [Bernstein et al. - 2004]. Below, theoretical signal evolution (without gradients applied) is shown (green curve). 37

Fig. 7: Schematic signal magnitude during a spin echo train. T2=220ms, T2'=30ms; with refocusing pulses at 25, 75, 125 and 175ms; the first spin echo occurs at TE=50ms. 38

Fig. 8: EPI pulse diagram. The phase encoding consists of small "blips" which move to the next k-space line. During each line acquisition, a gradient is observed. Image taken from [Bernstein et al. - 2004]. 39

Fig. 9: EPI k-space encoding scheme. After an initial preparation (black arrow), line acquisitions are done (red dashed arrows). In each line at $k_x = 0$, the spins are rephased in respect to k_x, and a gradient echo is formed. 39

Fig. 10: Signal evolution and 3D-GRASE readout. 40

Fig. 11: Schematic k-space slab with 3D-GRASE centric encoding. The partitions in z-direction are acquired alternating, beginning in the k-space center. For the temporal order, cf. Fig. 34. 41

Fig. 12: Gradient shapes and k-space coverage with an Archimedean spiral; 42

Fig. 13: Principle of segmented spiral readout; The k-space is acquired in several measurements. The data is combined before the fourier transform. From [Bernstein et al. - 2004] 43

Fig. 14: Surface plots of calculated pointspread fuctions of a single shot spiral sequence (left) and a single shot EPI (right). Matrix size is 256 x 256, acquisition time 3 x T2*; from [Amann - 2000].....44

Fig. 15: Sketch of the two basic ASL techniques; in PASL, a larger region is labeled for a short time; the readout module can in both cases be chosen arbitrarily 2- or 3-dimensional.....46

Fig. 16: Theoretical ASL signal from one voxel depending on the inflow time TI; labeled blood arrives in the voxel at TI=BAT (bolus arrival time); at later TI, the PASL curve shows T1 decay while CASL reaches a steady state.....46

Fig. 17: Symbolic representation of the free (dotted line) and bound (solid line) water proton pools in brain tissue. An off-resonant rf pulse can excite bound water molecules, which can exchange their magnetization with the free water pool. Image taken from [Tofts - 2003].....49

Fig. 18: The FAIR labeling scheme 50

Fig. 19: Schematic magnetization curves with and without background suppression; blood signal starts at $M_{||}$=-1 after inversion and decays with $T1_{blood}$=1500 ms. Tissue signal starts at $M_{||}$=0 after post-labeling saturation and relaxes with $T1_{tissue}$=800 ms.....51

Fig. 20: Characteristic inflow curves of three voxels, with different arrival times and perfusion values. 52

Fig. 21: Schematic pulse diagram of the optimized PASL-FAIR scheme A: The inversion pulse is slice selective in case of the control image and non-selective for the labeling image. B: After inversion, the readout region is saturated. This prepares a homogenous uniform magnetization in the readout region and also saturates any possible MT-effects there. C: Stationary tissue is suppressed by two background suppression 180° pulses which are optimized to null tissue signal at t = TI. D: At t=BL (bolus length), the blood bolus is truncated by application of Q2TIPS saturation pulses. Also, signal from outside the readout slab is suppressed. E: At t = TI, a 3D-GRASE single shot readout module acquires an image with whole-brain coverage.....53

Fig. 22 ASL time series dataset; Inflow time steps range from TI =100 ms to TI =2000 ms, with a step size of 100 ms. In the first images, voxels with larger vessels appear bright. As blood is delivered to the tissue via the capillaries, on the later time steps the signal is more uniformly distributed in the tissue. 55

Fig. 23: Typical data points from one voxel. The Buxton model from Equ. (40) can be fitted to the voxel data along the inflow time axis.....55

Fig. 24: Sketch from[St Lawrence et al. - 2000]. 57

Fig. 25 Figure from [Li et al. - 2005]; In the single-capillary four-phase model derived in this publication, arterial, capillary and tissue phases are considered. The exchange between capillary and tissue is governed by PS (b). The effect of PS on the classic ASL signal is shown in (a). 59

Fig. 26: Direct comparison between two models with fast exchange ("FPOCK", four-phase one-compartment Kety) and restricted permeability ("FPSCS", four-phase single-capillary stepwise model) with typical data points, depicting the difficulty to measure PS based on the T1 weighted signal. From [Li et al. - 2005]. 60

Fig. 27: Schematic BOLD and CBF response curves in one voxel showing brain activation in response to an external stimulus. Image taken from [Tofts - 2003] 61

Fig. 28: Model of two adjoining cylinders in a grey matter voxel perfused by two capillaries. At the bottom, the relief of theoretical oxygen concentration is shown in the capillaries and surrounding tissue. From [Purves - 1972].....64

Fig. 29: Schematic pulse diagram of the GESSE sequence ("Gradient Echo Sampling of the Spin Echo"). In the signal intensity is shown in the green curve. A spin echo is formed at TE. The readout gradient encodes the same Fourier line multiple times for different times relative to TE. Image taken from [Yablonskiy, Haacke - 1997] 65

Fig. 30: Representative maps of brain parameters obtained with a low-resolution (64x64) GESSE sequence at 3T. Top left: high-resolution anatomic image. Rest of the maps: DBV fraction (deoxygenated blood volume , corresponds to ξ, in %), OEF (%), $R2$ for brain tissue (1/s), CSF volume fraction, CSF frequency shift (Hz), R2 of brain tissue (1/s), brain deoxyhemoglobin concentration (μM). Image taken from [He, Yablonskiy - 2007].....66

Fig. 31: Schematic diagram of an MR voxel; There are two compartments, a blood (considered purely capillary), and an extra vascular compartment, both with their appropriate relaxation constants. The measured R1 and R2 values will be a mixture from signal of both compartments. 68

Fig. 32: Theoretical curves showing S_{bl} (red), S_{ex} (green) and S (blue) from EQU… The plots are calculated with f =175 ml/100g/min, BAT =600 ms, BL =1000 ms, $T1_{bl}$ =1500 ms, $T1_{ex}$ =1100 ms and $T_{bl\to ex}$ =300 ms.....71

Fig. 33: Two-dimensional plots showing blood component (red), extra-vascular component (green) and total signal (blue) from (64). Signal decay due to T2 along the te axis is fast for the extravascular component and slower for the blood component. The plots are calculated with f =175 ml/100g/min, BAT =600 ms, BL =1000 ms, $T1_{bl}$ =1500 ms, $T1_{ex}$ =1100 ms and $T_{bl\to ex}$ =300 ms. 76

Fig. 34: Readout scheme of the modified 3D-GRASE for T2 measurements; the readout blocks are shifted to later echo times TE after the 90° preparation pulse. 79

Fig. 35: Primary spin echoes and stimulated echoes: For two different rf pulse timings, extended-phase graphs are shown. In blue, the echo pathways of the primary spin echo are shown. The green and red dashed lines are possible pathways after the second rf pulse, the green later forming a stimulated echo. On the left, the stimulated echo occurs before the primary spin echo after the third rf pulse. On the right, with optimized pulse spacing, the echoes coincide. 80

Fig. 36: ASL difference image dataset (some images skipped in ti direction); Along the *ti* axis, the inflow of blood can be seen first in areas around large vessels (e.g. MCA). At later *ti* the signal diffuses and is assumed to come predominantly from tissue. Also, signal decays with T1. Along the *te* axis, T2 decay can be observed. Flow artifacts occur at ti=450 ms (black dots). 86

Fig. 37: Data and fit from and fit from a voxel with fast exchange. Blood signal is zero all the time. The total signal curve is built up only from the extra-vascular signal. 87

Fig. 38: Data and fit from a voxel with slow exchange. The blood signal rises fast with *ti* until the end of the bolus is reached. The extra-vascular signal rises much slower. 87

Fig. 39: 2d plots from a voxel with apparent fast exchange showing data and fitted total signal curves (top), for all three echo times. The percentage of signal origin is shown (bottom). All of the signal is coming from the extra-vascular compartment most of the time. A slow exchange voxel is shown in Fig. 40. 89

Fig. 40: ASL curves as in Fig. 38, from a voxel showing significant permeability. Signal originates from the blood compartment in the beginning. Blood signal drops with *ti* even faster when $BAT + BL$ is reached and no fresh labeled blood replenishes the blood compartment. 90

Fig. 41: Derived maps for one 91

Fig. 42: $T_{bl\to ex}$ map and corresponding fitting error; typical values are shown in the ROI analysis. The SMA appears bright in the left image (red ROI) indicating high $T_{bl\to ex}$ values. 91

Fig. 43 T1 weighted images, $T_{bl\to ex}$ maps; 92

Fig. 44: Time-to-peak (TTP): concept of deriving parameter TTP 94

Fig. 45: Left to right: T1 weighted anatomical image, Grey matter segmentation, Time-to-peak maps derived from an ASL time series dataset. Typical values are shown (blue arrows). 95

Fig. 46: Grey matter probability map; the GM map has been Gaussian smoothed (sigma 1.1); typical values (blue arrows, left to right): 0.7, 0.8, 0.5, 0.8 96

Fig. 47: Schematic voxel depicting the *OEF* model. The tissue voxel is perfused by several capillaries. Inside the capillary, *OEF* rises towards the venous end asymptotically (cf. [Purves - 1972]). 101

Fig. 48: The perfused voxel with schematic assumed labeled water distribution (blue) over different ASL inflow times TI. Because of the small inter-capillary distance, water is expected to be in equilibrium between capillaries after approximately 100 ms (cf. Ch. 2.4.2). Conversely, the capillary bed is traversed along the capillary direction in a time range of several seconds (cf. [Tofts - 2003]). Along the capillary direction, no change in relative vascular compartment size is assumed.....102

Fig. 49: Schematic pulse diagram and contrast mechanism of the spin/gradient dual echo double spiral 3D-GRASE readout. Spiral readouts start at $t = TE$ on the spin echo center and at $TE - \delta TE$ on the rising slope. 103

Fig. 50: Anatomic (upper) and $R2^+$ (lower) images. The scaling is in 1/s. Bright regions indicate high field inhomogeneities and dominant $R2'$. 106

Fig. 51: Apparent OEF map with fixed parameters $R2$ and ξ. The value in ROI A is reasonable. Large differences between the ROIs point to external field inhomogeneities, especially in the frontal area.....107

Fig. 52: T1 weighted image, perfusion and BAT maps. There is a strong dependence of perfusion on tissue type (white / gray matter). BAT values differ from 100 to 1500 ms. The lower images indicate typical perfusion and BAT values. The BAT map has been smoothed with a Gaussian filter, sigma = 0.6. 109

Fig. 53: Gradient and spin echo images from the spin/gradient dual echo double spiral 3D-GRASE (ns+ss average, TI=2000ms). Signal loss due to susceptibility inhomogeneities can be seen at the frontal sinus (blue arrows)..110

Fig. 54: Typical time series of $R2^+$ values. Two slices are shown. The windowing is chosen such that positive values appear yellow and negative values blue. The data is already corrected for BAT. This leads to the white spots at later time steps where no further signal evolution has been acquired. In the first row, a lower slice has been chosen. High R2' values can be seen in the area of the frontal sinus. 111

Fig. 55: Typical maps from three subjects; from left to right: T1 weighted anatomical image, ASL fitted perfusion image, $R2^+$ image (yellow: R' dominant), $R2^+$ change over TI (yellow: increase). In the first perfusion image, the MCA and PCA can clearly be seen.....112

Fig. 56: From left to right: anatomic image, apparent OEF averaged over all relevant time steps, linear trend of apparent OEF development. Values lie between zero and one in the temporal and occipital lobes and yield reasonable results. In the same areas, the linear regression over TI shows has a positive slope (shown in red). 113

Fig. 57: Typical OEF curves (upper) and corresponding inflow curves (lower). OEF values are scaled such that zero corresponds to no susceptibility effects due to de-oxygenation, and one corresponds to the OEF found from the tissue signal. The inflow curves show the perfusion weighted signal. Noise artifacts in the OEF estimation are more likely at early and late TI with low SNR. 113

Fig. 58: Arteries of the neck; the right ICA and the Vertebral Artery are interconnected in the Circle of Willis. Image on Wikipedia, from the 20th U.S. edition of Gray's Anatomy of the Human Body, originally published in 1918 120

Fig. 59: Schematic diagram of the vascular system around the Circle of Willis. Blood is flowing in through the Vertebral and Basilar arteries and the ICAs. From there it is delivered to the brain by the MCAs and other smaller arteries. Blue dashed arrows indicate blood flow direction. Image from Wikipedia, public domain.....121

Fig. 60: From left to right: T1 weighted image, segmented Gray matter, segmented White matter. In T1 weighted images, Grey matter appears grey, white matter white, CSF black. Segmentations hve been computed automatically with SPM5 [S – SPM5]. 122

List of tables

Tab. 1: Initial fitting parameters of the T2-ASL data evaluation. 83

Tab. 2: Values for $M_{0,a}$, derived from twelve ASL time series measurements, with five subjects and different measurement protocols. T2-ASL are the measurements of the current, T2'-ASL the data from the following chapter.....85

Tab. 3: Typical fitting results for two selected voxel. 88

Tab. 4: Table containing ROI values and fitting errors. PS values have also been calculated assuming a venous relative compartment size of 0.02. 93

Tab. 5: T1 values reported in different publications 123

Tab. 6: T1 and T2 values from [Wansapura et al. - 1999] regarding different brain regions.....124

Tab. 7: T1 values from [Clare, Jezzard - 2001] regarding different brain regions.....124

Tab. 8: T2 values reported in different publications. 126

Tab. 9: T2* values reported in different publications 127

1 Preface

The scientific and technological revolution of Magnetic Resonance Imaging (MRI) in the last decades guaranteed a vast spread and success in many medical imaging applications. The improvements in image quality make it a competitive technique compared to CT. The most compelling advantage is the fact that MRI, unlike CT or PET, works without any ionizing radiation. In MRI experiments, there are no limitations in repeatability because of dose considerations.

Beginning in the 1980s, MRI has also been used to measure dynamic processes. There exists a large variety in imaging techniques like diffusion weighted imaging, diffusion tensor imaging, Time of Flight angiography, functional imaging for measuring brain activation, and perfusion imaging using MR contrast agents. In 1992, Arterial Spin Labeling (ASL) has been invented, a perfusion imaging technique which uses the natural blood water spins as contrast agent and thus working totally non-invasively. This, again, eliminates the potential risks of injected contrast agent and is therefore the technique of choice looking at risk and repeatability. Lately, ASL applications has been included in commercially available MR systems by the first manufacturers in 2008.

Several physical effects are the source of different relaxation mechanisms in MRI. The spin-lattice interaction gives rise to T1 relaxation, the spin-spin interaction is the underlying mechanism of T2 relaxation. Local magnetic field inhomogeneities lead to a further relaxation, T2'. The technique ASL has been well investigated in the field of perfusion imaging and quantification. In basic ASL experiments, T1 is the relaxation which mostly contributes to the perfusion signal dynamics, and is commonly the only one which is included in ASL models. There still exist many effects which are not yet considered or included in the common models, but which hold high potential to investigate and measure different physiological parameters. Two major effects are expected with measuring T2 and T2' of the ASL signal. There is a significant difference between blood T2 and tissue T2. So, measuring T2 of the ASL signal could give insight in the origin of the perfusion signal, and thus enable the estimation of blood brain barrier permeability. T2' measurements are closely related to oxygenation in blood vessels. Measurements combined with ASL could give deeper insight in perfusion and oxygenation dynamics and indicate local blood oxygenation and brain activation changes.

The permeability of the blood brain barrier plays a large role in contrast-based MR perfusion imaging. In several cerebral diseases, the blood brain barrier is affected and permeability is increased. This can be measured with tracer based perfusion techniques, where the intra-vascular contrast agent, consisting of macro-molecules which usually do not cross the blood brain barrier, will accumulate in the surrounding tissue.

Water molecules are expected to pass the blood brain barrier easily due to their small size. Blood and tissue are known to have significantly different T2 values. For investigating the blood water exchange rate to the perfused tissue, T2 is in principal an excellent marker. The effect of a restricted water permeability of the blood brain barrier on the classical ASL signal which measures the T1 governed signal evolution has already been described in recent publications. It turned out that the effect is so small that it can hardly be measured. Measuring T2 of the ASL signal can thus be an excellent way to measure the blood brain barrier water permeability.

The oxygenation of venous blood depends on the brain activation in the drained regions. The effect of oxygenation on the T2* or T2' weighted signal of surrounding tissue is well investigated and commonly used in functional MRI experiments. Since brain activation also correlates with perfusion, the feasibility of ASL based functional imaging experiments could be shown several years ago.

Measuring T2' of the inflowing blood water could give further insight in the transport of the blood water molecules through the capillary bed, and the capillary oxygen extraction from the arterial to the venous side. Moreover, in functional imaging, a T2' based ASL measurement would allow a simultaneous acquisition of perfusion and oxygenation changes. In recent years, a lot of effort has been put on quantification of functional imaging. This could potentially be achieved by an ASL technique which simultaneously measures T2'.

So far, these different mechanisms and contrasts of the ASL signal haven't been investigated yet. It is the intention of this work to shed light on this new field of ASL beyond the aspect of perfusion, to give an introduction of multi-parametric ASL measuring T2 and T2', and show the possibilities and implications which result.

The thesis contains the presentation of two imaging sequences to measure T2 and T2': a 3D-GRASE with variable echo time, and a novel spin/gradient dual echo double spiral

3D-GRASE readout for T2’ quantification. In vivo images of the human brain are shown for both cases, acquired at a 3 Tesla scanner system. Data has been evaluated investigating capillary wall permeability and dynamic oxygenation changes.

1.1 Content

The basic introduction in MR physics, MR sequence design and physiological mechanisms in Chapter 2 will mound in currently ongoing considerations and evaluation techniques of the classical ASL signal. An important part will be the thorough description of the sequence used to acquire ASL time series. Other aspects will be the discussion of existing two compartment models, including permeability and oxygenation considerations.

Chapter 3, which addresses the T2 measurements, starts with the theoretical derivation of a two-dimensional model describing the ASL signal evolution depending on the inflow time and the echo time, which includes T1 and T2 decay as well as capillary wall permeability. The readout sequence, a modified 3D-GRASE sequence with variable echo time, will be presented. Acquired data will be shown. Permeability value maps are derived from fitting the model to the data. A discussion about reliability and possible errors follows.

The dynamic ASL T2’ measurements are described in Chapter 4. After a short recapitulation about oxygenation effects in perfused tissue, the development of the readout module is described. A spin/gradient dual echo double spiral 3D-GRASE sequence has been developed for this task and is presented in this work. The basic contrast mechanism is described and dynamical image data shown. The change in T2’ over the inflow time, which can be put in relation to oxygen extraction along the capillary bed, is investigated and possible conclusions are discussed.

After a concluding summary in Chapter 5, the Appendix contains basic knowledge about physiological and anatomical aspects of brain perfusion as well as tables with common values for T1, T2 and T2’ at the field strength of 3 Tesla.

2 Theory

This chapter will give an overview about the physics of magnetic resonance (MR) of spins in an external field, the basics of magnetic resonance imaging (MRI), and important physiological aspects governing perfusion.

2.1 Magnetic Resonance

A short introduction to the Physics of nuclear magnetic resonance (NMR) and magnetic resonance imaging (MRI) will be given in this chapter. An extensive introduction to NMR Physics can be found in [Slichter - 1978]. For a more detailed view on MR imaging the thorough work of [Haacke et al. - 1999] can be recommended.

2.1.1 The spin in a magnetic field

MRI makes use of the characteristic properties of water proton spins. Protons are spin 1/2 particles and therefore have a magnetic moment, which can be described as

$$\vec{\boldsymbol{\mu}} = \gamma \cdot \vec{\mathbf{J}} = \gamma \cdot \hbar \cdot \vec{\mathbf{I}} \tag{1}$$

γ	Gyromagnetic ratio
$\vec{\mathbf{J}}$	Angular moment operator
$\vec{\mathbf{I}}$	Spin operator
$\hbar = 6.626 \times 10^{-34}\,\mathrm{Js}$	Planck constant

$\mathbf{I_z}$ has two eigenvalues: $m = +\frac{1}{2}, -\frac{1}{2}$.

The Hamiltonian for such a system in an external magnetic field $\vec{H}$, taken arbitrarily along the positive z-axis $H_z \equiv H_0$, is then

$$-\vec{\boldsymbol{\mu}} \cdot \vec{\mathbf{H}} = -\gamma \cdot \hbar H_0 I_z \tag{2}$$

This Hamiltonian has two eigenvalues $E = -\gamma \cdot \hbar H_0 m = \mp \frac{1}{2} \gamma \cdot \hbar H_0$, for $m = \pm \frac{1}{2}$, and hence two possible energy levels. The energy difference between the two energy states is

$$\Delta E = \gamma \cdot \hbar \cdot H_0 \tag{3}$$

The two energy levels are called parallel and anti-parallel spin states, corresponding to the macroscopic magnetization in respect to the external field H_0, as will be seen in the following. The parallel state has lower energy and will therefore be preferred. The population ratio of the parallel and anti-parallel state in a small volume gives rise to a macroscopic magnetization $\vec{M} = \left(M_x, M_y, M_z\right)$, which is the basis to the MR signal. With the exclusive presence of a constant external field, like in the Hamiltonian from Equ. (2), $\vec{M}$ will be parallel to the external field. In the general case, $\vec{M}$ will have transversal components M_x and M_y as well. $\vec{M}$ can be split up into the parallel magnetization $M_\parallel$ and the transversal magnetization $M_\perp$, following the relations

$$\begin{aligned} M_\parallel &= M_z \\ M_\perp &= M_x + i \cdot M_y \end{aligned} \tag{4}$$

$M_\perp$ is a complex number, with real part M_x and imaginary part M_y. Equivalently, $M_\perp$ can be given in magnitude and phase.

Because energy states in the equilibrium are Boltzmann distributed, at room temperature, also anti-parallel states will be occupied. The distribution of states, namely the ratio of the number of aligned states N_+ and anti-aligned states N_- in the equilibrium is given by

$$\frac{N_+}{N_-} = e^{\gamma \cdot \hbar H_0 / kT} \tag{5}$$

$k = 1.38065 \times 10^{-23}$ J/K	Boltzmann constant
T	Temperature

The surplus of aligned spins builds up a longitudinal equilibrium magnetization M_0, in a probe with N water protons per unit volume:

$$M_0 = \frac{N \cdot \gamma \cdot \hbar^2 \cdot H_0}{4kT} \tag{6}$$

Although the surplus of aligned spins is only on the order of 10^{-5} at room temperature, M_0 is observable and can be used for MRI because of the abundance of water protons in tissue.

The spin system can be manipulated by electro-magnetic interactions of the Larmor frequency ω_0, which corresponds to the energy difference between the two states.

$$\omega_0 = \frac{\Delta E}{\hbar} = \gamma H_0 \tag{7}$$

For ^{1}H of water molecules, $\gamma / 2\pi = 42.576$ MHz/T. At common field strengths between 1 and 4 Tesla, the Larmor frequency is in the range of radio- and microwave frequencies.

The actual energy levels are influenced by the molecular bindings as well. Proton spins of different molecules have different characteristic Larmor frequencies, which gives rise to the chemical shift. At 3 Tesla, the chemical shift between ^{1}H of water and fat is about 450 Hz. The dependency of the Larmor frequency on the molecular binding is exploited in NMR spectroscopy where the frequency is swept through a certain range to identify different compositions of molecules in a certain probe. In our case, only the water molecules are considered.

2.1.2 RF pulses

The macroscopic magnetization $\vec{M}$ has the properties of a magnetic moment. In the presence of an arbitrary time dependent magnetic field $\vec{B}(t)$, neglecting relaxation effects, it follows the equation

$$\frac{d\vec{M}(t)}{dt} = \gamma \cdot \vec{M}(t) \times \vec{B}(t) \tag{8}$$

Let's first consider a constant static external field $\vec{B}(t) = \vec{H}_0$, without loss of generality parallel to the z axis, and a magnetization $\vec{M}$ with non-negative transverse component $M_\perp$. The transverse and parallel vector components of Equ. (8) uncouple to

$$\begin{aligned} \frac{dM_x}{dt} &= \gamma \cdot H_0 \cdot M_y \\ \frac{dM_y}{dt} &= -\gamma \cdot H_0 \cdot M_x \\ \frac{dM_z}{dt} &= 0 \end{aligned} \tag{9}$$

This means that $M_\perp$ will precess around the z axis with angular frequency $\omega_0 = \gamma \cdot H_0$, while $M_\parallel$ will remain constant.

As mentioned beforehand, the net magnetization can be manipulated by radio frequent interactions. This is can also be described using Equ. (8). The magnetic field $\vec{B}_1$ induced by electro-magnetic waves with angular frequency ω_{HF} and amplitude B_1, polarized perpendicular to the z axis, follows the equation

$$\vec{B}_1(t) = B_1 \cdot \left(\cos(\omega_{HF} \cdot t), \sin(\omega_{HF} \cdot t), 0\right) \tag{10}$$

This radio-frequent or rf field is superimposed on the static external field $\vec{H}_0$ aligned along the z axis. Equ. (8) becomes

$$\frac{d\vec{M}(t)}{dt} = \gamma \cdot \vec{M}(t) \times \left(B_1 \cos(\omega_{HF} \cdot t), B_1 \sin(\omega_{HF} \cdot t), H_0\right) \tag{11}$$

This equation describes the manipulation of $\vec{M}$ by switching additional rf fields. By correct choice of frequency and magnitude of the rf pulse, the net magnetization can be prepared, e.g. to be anti-aligned or perpendicular to the external field. Choosing the Larmor frequency ($\omega_{HF} = \omega_0$) and a constant amplitude B_1, it can be shown that after a

pulse length t_p, $\vec{M}$ is deviated from the equilibrium by the angle α (e.g. [Haacke et al. - 1999]):

$$\alpha = \gamma \cdot \int_0^{t_p} B_1(\tau) d\tau = \gamma \cdot B_1 \cdot t_p \tag{12}$$

This is called the flipangle. For magnetization inversion, $\alpha = 180°$ is chosen, corresponding to a 180°-rf pulse or π-pulse. For preparation of a transverse magnetization, a 90°-pulse or $\pi/2$-pulse is applied. Pulse shape and frequency characteristics have influence on the spatial localization of the prepared magnetization, the efficiency of the pulse and on the transmitted energy. There exist various approaches and variants of rf pulses.

In MR imaging, the net magnetization of small volumes ("voxel") is considered. Therefore, a transverse magnetization has to be prepared in the considered voxels, e.g. by a 90° rf pulse. As the net magnetization precesses around the z axis, it emits radio frequent electro-magnetic waves. This signal can be acquired by coils located around the probe.

2.1.3 The Bloch equations, T1 and T2

In Equ. (8), relaxation effects have been neglected. In reality, if the net magnetization is disturbed or deviated from the equilibrium, it will take a characteristic time to recover and realign with the external field. The magnetization in z-direction follows the Bloch equation:

$$\frac{dM_{\parallel}}{dt} = \frac{M_0 - M_{\parallel}}{T1} + \gamma \cdot \left(\vec{M} \times \vec{H}\right)_z = \frac{M_0 - M_{\parallel}}{T1} + \gamma \cdot \left(M_x H_y - M_y H_x\right) \tag{13}$$

The characteristic relaxation time constant is T1 and depends on the magnetic field and the probe material. It has been introduced phenomenologically in this equation. T1 relaxation is due to spin-lattice interactions. In this process, energy is exchanged between the spin system and the chemical bindings of the surrounding lattice. This is a dissipative thermodynamical process and the energy cannot be recovered.

After preparing a transverse magnetization component as shown in the last section, $M_\perp$, will precess around the z direction with ω_0. $M_\perp$ is also prone to relaxation phenomena. The characteristic decay constant is called T2. It is associated to the spin-spin interaction which leads to relative dephasing of spins. The consequence is a resulting smaller transverse component in the vector addition. In Equ. (4), $M_\perp$ is given as a complex number, where the real and imaginary parts correspond to the physical x and y axes. In this notation, the external field transverse component is

$$H_\perp = H_x + iH_y \tag{14}$$

The Bloch equation for $M_\perp$ is then:

$$\frac{dM_\perp}{dt} = -i\gamma \cdot \left(M_\perp \cdot H_z - M_z \cdot H_\perp\right) - \frac{M_\perp}{T2} \tag{15}$$

The Bloch equations describe a classical system of magnetization. In fact, it turns out that the classical view is equivalent to the quantum mechanical view (cf. e.g. [Slichter - 1978], Ch. 2). Therefore, the net magnetization $\vec{M}$ can be considered as the classical observable used for MRI, with a longitudinal part $M_\parallel$ with characteristic time constant T1, and a transverse part $M_\perp$ which decays with T2.

In many cases, the use of the relaxation rates is more convenient and shall be introduced here:

$$R1 \equiv \frac{1}{T1} \tag{16}$$

$$R2 \equiv \frac{1}{T2} \tag{17}$$

2.1.4 Solutions to the Bloch equations

The Bloch equations can be solved for special settings. Two cases will be covered here, since they are the basis of measuring T1 and T2.

2.1.4.1 Inversion recovery and TI

If the magnetization is totally inverted at the beginning, i.e. the starting conditions at $t = 0$ are $M_{\parallel} = -M_0$ and $M_{\perp} = 0$, we speak of an Inversion Recovery (IR) experiment. IR experiments are used to measure T1. In the absence of transverse components in $\vec{H}$ and $\vec{M}$, only Equ. (13) needs to be considered. The solution for the parallel magnetization is:

$$M_{\parallel}(t) = M_0 \cdot \left(1 - 2 \cdot e^{-t/T1}\right) \tag{18}$$

In IR experiments, the parallel magnetization can be measured at different times after inversion to sample the T1 relaxation. For the signal acquisition, $M_{\parallel}$ is flipped to the transverse plane by a 90° pulse for readout. The chosen time is called inversion time TI. As can be seen in Fig. 1, the choice of TI will result in different signal contrast. Especially, signal of one certain TI can be "nulled" by choosing TI=TI_0.

Important to note here is that later in this work, considering, TI will be called "inflow time". This is a more informative description for TI in the case of ASL, but will basically describe the same mechanism as explained here.

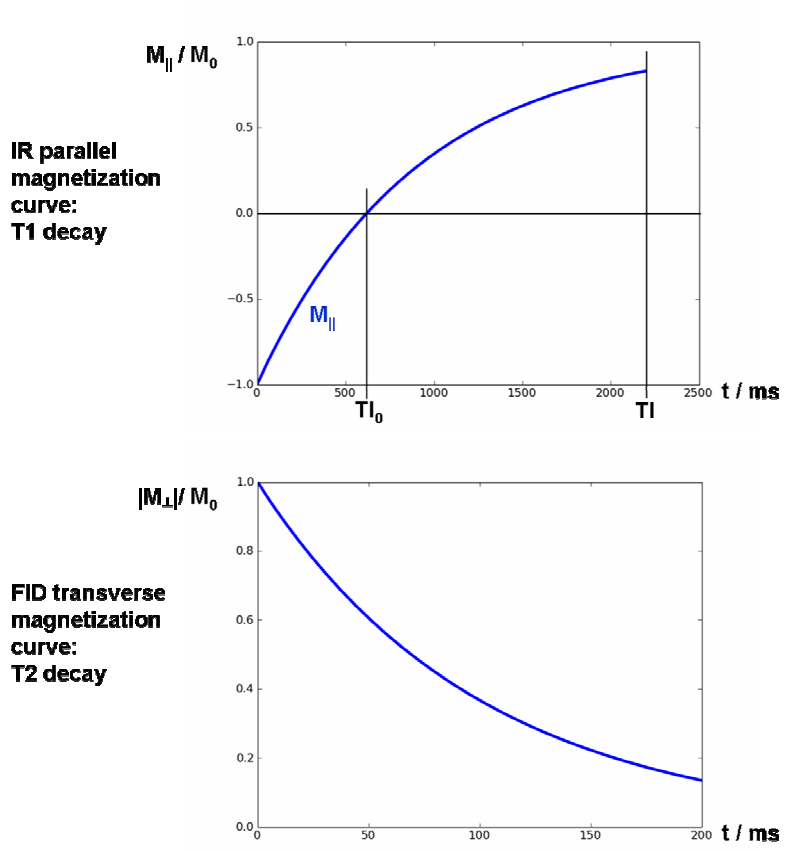

Fig. 1: Theoretical signal decay in IR (upper) and FID (lower) experiments. T1=800 ms and T2=100 ms have been chosen.

2.1.4.2 Free Induction Decay and TE

Another important case is the situation after application of an ideal 90°-pulse. The starting conditions are $M_{\perp} = M_0$ and $M_{\parallel} = 0$. This corresponds to Free Induction Decay (FID) experiments, where the transverse decay constant T2 can be measured. The solution for the transverse magnetization is

$$M_{\perp}(t) = M_0 \cdot e^{-t/T2 - i\gamma H_0 t} \tag{19}$$

The complex magnetization has a magnitude part which describes a simple exponential decay, and an oscillating phase part. For imaging, usually the magnitude part is considered. Again, the decay curve can be sampled at different times after the preparation of the transverse magnetization. The chosen time of readout is called echo time TE.

2.1.5 T2' and T2* Relaxation

The spin-spin interaction, which has been introduced with the Bloch equation of the transverse magnetization, Equ. (15), leads to a relative dephasing of neighboring spins. The resulting temporal dependence of the magnitude part of $M_\perp$ is:

$$\left|M_\perp(t)\right| = \left|M_\perp(0)\right| \cdot e^{-t/T2} \tag{20}$$

Another mechanism leading to additional signal decay is caused by macroscopic field inhomogeneities, summarized as ΔB_0. Neighboring spins in an inhomogeneous field which experience slightly different magnetic field strengths sum up a relative phase difference over time. The interference leads to a declining signal coming from a voxel with inhomogeneous field. The decline is also modeled as an exponential decay, named T2' ("T2 prime"). The relation with the mean local field inhomogeneities is

$$T2' = \frac{1}{\gamma \cdot \Delta B_0} \tag{21}$$

Predominantly local susceptibility changes of the probe contribute to the magnetic inhomogeneities, especially at tissue boundary surfaces. Other examples are contrast agent in vessels or the BOLD effect (cf. Ch. 2.4.2, p60), which originates from a different susceptibility of venous blood compared to tissue and arterial blood.

The overall observed decay is then faster, with relaxation rate

$$R2^* = R2 + R2' \tag{22}$$

Here, again, the relaxation rates $R2' \equiv 1/T2'$ and $R2^* \equiv 1/T2^*$ have been used.

2.1.6 The spin echo

In 1950 Hahn found out experimentally, that the observed MR signal rises again after the application of a 180° pulse in the transverse plane, until it reaches a maximum and then again follows a T2* decay [Hahn - 1950]. This phenomenon has later been called "Hahn spin echo". The inhomogeneous external field in those early magnetic resonance experiments was the cause for very short T2*. Field inhomogeneities within one voxel lead to different resulting Larmor frequencies. This means that there are faster and

slower precessing parts of the magnetization within the same voxel. A spin echo arises because the dephased spins are “flipped” by 180° along a transverse axis, but keep precessing in the same direction along the z-axis. Spins which have been “slower” and lagging behind are now ahead, but still slower because the local magnetic field inhomogeneities haven’t changed. As the faster precessing spins “catch up” with the slower ones, the transverse magnetization is refocused and all the previously dephased magnetization is recovered. The spin-spin interactions instead are irreversible, and so the envelope of the spin echo signal shows a pure T2 decay (Fig. 7).

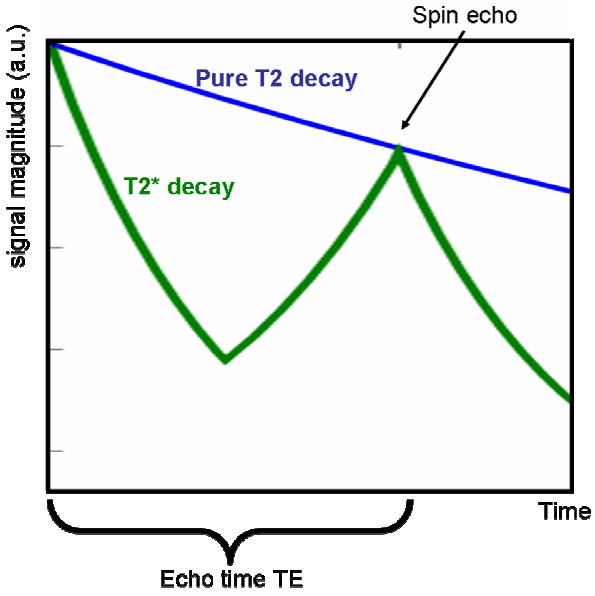

Fig. 2: Schematic plot of the $M_{\perp}$ magnitude part (green). The blue line indicates pure T2 decay. A refocusing pulse is applied at TE/2, a spin echo formed at TE.

Spin echoes are widely used in imaging sequences as a method to prepare the signal and conserve it long enough for the readout, and to minimize dephasing effects due to susceptibility inhomogeneities.

2.2 MR imaging and readout techniques

The books [Haacke et al. - 1999] and [Bernstein et al. - 2004] give an excellent view on aspects of MRI imaging and sequence design. After an introduction to the basic concept of k-space and standard sequences, the advanced imaging sequences which are important for this work shall be introduced now.

2.2.1 Spatial encoding

After a transverse magnetization has been prepared, the precession of $\vec{M}$ leads to emission of electromagnetic waves of frequency ω_0. This signal can be acquired and used for MRI. Obviously, magnetization from the entire probe adds to the acquired signal. This signal does not contain any spatial information yet. To extract the spatial information and reconstruct an image, different spatial encoding configurations have to be acquired one after another. The encoding is done by applying time dependent magnetic field gradients G_x, G_y, G_z in all three spatial dimensions. It is usually done in three steps: slice encoding, phase encoding and frequency encoding, corresponding to the z, y and x axes in image space. The resulting external field is then

$$\vec{H}(t) = \vec{H}_0 + \begin{pmatrix} x \cdot G_x(t) \\ y \cdot G_y(t) \\ z \cdot G_z(t) \end{pmatrix} = \begin{pmatrix} x \cdot G_x(t) \\ y \cdot G_y(t) \\ H_0 + z \cdot G_z(t) \end{pmatrix} \tag{23}$$

2.2.1.1 Slice encoding

A maximum $M_\perp$ can be prepared globally by applying an rf pulse which is trimmed such that the equilibrium magnetization is flipped by 90°. This 90° rf-pulse has frequency ω_0. If a slice encoding gradient G_z is switched on along the z axis, the resulting magnetic field along z, $H_0 + z \cdot G_z$, is altered for $z \neq 0$. The rf-pulse becomes off-resonant and will prepare less transverse magnetization for $z \neq 0$. In reality, finite pulses will excite a frequency range, which can be characterized by the bandwidth of the rf-pulse, $\Delta\omega_{HF} = \gamma \cdot G_z \cdot \Delta z$. Approximately, a frequency range $\omega_0 \pm \Delta\omega_{HF}/2$ will be excited. In this way, a slice of width Δz can selectively be excited in the probe.

2.2.1.2 Phase encoding

After slice encoding, the emitted MR signal comes from the two dimensional slice. Before the signal acquisition starts, another encoding gradient $G_y(t)$ is switched on for a short time t_{ph} in y-direction. The transverse magnetization is then

$$M_\perp(\vec{x},t_{ph}) = \left|M_\perp(\vec{x},t_0)\right| \cdot e^{i\cdot\gamma\cdot\int_0^{t_{ph}} y\cdot G_y(\tau)d\tau} \tag{24}$$

The gradient induced field $y \cdot G_y$ depends linearly on y. Therefore, a phase shift in $M_\perp$ will accumulate for coordinates with $y \neq 0$. The magnitude remains unaltered. The phase shift, depending on the spatial location in y direction, is:

$$\varphi_{ph}(y) = \gamma \cdot \int_0^{t_{ph}} y\cdot G_y(\tau)d\tau \tag{25}$$

2.2.1.3 Frequency encoding

The last step is the switching of the frequency encoding gradient G_x, also called readout gradient. This is done simultaneously to the signal acquisition. This results in an additional phase accumulation along x-direction, directly proportional to the readout time t_{ro}. It is equivalent to Equ. (25):

$$\varphi_{ro}(x) = \gamma \cdot \int_0^{t_{ro}} x\cdot G_x(\tau)d\tau \tag{26}$$

The total signal acquired from the slice at t_{ro}, depending on the previous preparation of G_y and t_{ph}, is

$$S(t_{ro,}G_y) = \int_{x,y} \left|M_\perp(\vec{x},t_0)\right| \cdot e^{i\cdot\gamma\cdot\int_0^{t_{ro}} x\cdot G_x(\tau)d\tau} \cdot e^{i\cdot\gamma\cdot\int_0^{t_{ph}} y\cdot G_y(\tau)d\tau} dxdy \tag{27}$$

The signal data acquired during one frequency encoding step with fixed phase encoding is usually called a Fourier line. After the acquisition of several Fourier lines with different phase encoding, Fourier transformation of this integral will yield the transverse

magnetization depending on the spatial signal origin, as will be seen in the following subsection.

The three gradients introduced above are shown schematically in Fig. 3, where the acquisition of one Fourier line is demonstrated.

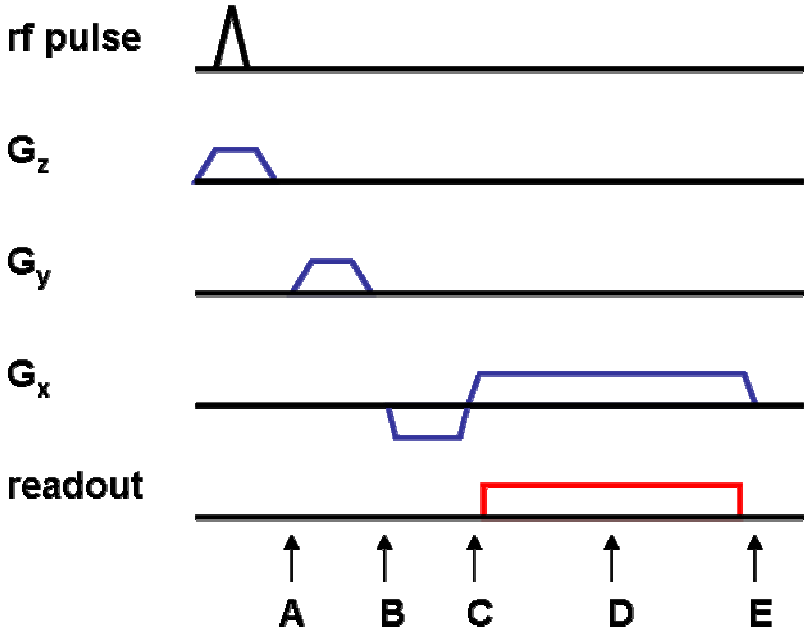

Fig. 3: Encoding scheme with: Slice encoding G_z simultaneously to the rf preparation pulse, phase encoding G_y, frequency encoding G_x simultaneously to the readout. Letters refer to Fig. 5.

2.2.1.4 3D-Encoding

Important to mention here is the mode of operation of 3D sequences. Instead of preparing the magnetization in one slice (in the range of millimeters), a larger imaging slab is prepared. To retrieve spatial information in z-direction, phase-encoding is applied before readout in z-direction as well. The signal equation will then have three exponential terms and the Fourier transform will range over three dimensions:

$$S(t,G_x,G_y,G_z)=\int_{x,y,z}\left|M_\perp(\vec{x},t_0)\right|\cdot e^{i\cdot\gamma\cdot\int_0^t x\cdot G_x(\tau)d\tau}\cdot e^{i\cdot\gamma\cdot\int_0^t y\cdot G_y(\tau)d\tau}\cdot e^{i\cdot\gamma\cdot\int_0^t z\cdot G_z(\tau)d\tau}dxdydz \qquad (28)$$

Here, in contrast to Equ. (27), the temporal variable t has been used in all three exponents. This is a more general formalism. It uses the fact that for times where $G(t) = 0$, i.e. after t_{ro} or t_{ph} in the former notifications, there is no contribution to the integral in the exponent.

For clarity, the reconstructed image slices are usually called partitions, and the encoding in z-direction is called “partition encoding”. 3D-encoding generally has the advantage of higher signal to noise ratio (SNR) because of the longer readout time where signal is acquired. Neglecting relaxation and saturation effects, with N_z encoded partitions, the theoretical gain in SNR is $\sqrt{N_z}$.

2.2.2 Image reconstruction and k-space formalism

Image acquisition comprises signal preparation, a temporal sequence of switching encoding gradients and the signal readout over time. The signal follows Equ. (28) and is stored before reconstruction. After all Fourier lines are acquired with different phase and partition encoding, the reconstruction of the slice can be done.

It can be shown that the temporal integral of the gradient field used for encoding corresponds to the wave number k yielding

$$\begin{aligned} k_x &= \gamma \cdot \int_0^t G_x(\tau) d\tau \\ k_y &= \gamma \cdot \int_0^t G_y(\tau) d\tau \\ k_z &= \gamma \cdot \int_0^t G_z(\tau) d\tau \end{aligned} \tag{29}$$

Equ. (27) becomes

$$S(k_x, k_y, k_z) = \int_{x,y,z} \left| M_\perp(\vec{x}, t_0) \right| \cdot e^{i \cdot k_x x} \cdot e^{i \cdot k_y y} \cdot e^{i \cdot k_z z} dx dy dz \tag{30}$$

This measured signal can be easily interpreted as a Fourier transform of the transverse magnetization, being its representation in k-space. This is where the concept of k-space comes into play. The signal can therefore be retransformed to obtain the representation in image space:

$$\tilde{S}(x,y,z) = 2\pi \int_{k_x,k_y,k_z} S(k_x,k_y,k_z)\cdot e^{-i\cdot k_x x}\cdot e^{-i\cdot k_y y}\cdot e^{-i\cdot k_z z} dk_x dk_y dk_z \tag{31}$$

This is the decoded image, i.e. the complex signal depending on its spatial origin in the probe. In the special case of $k_z \equiv 0$, this equation is reduced to two dimensions and represents an image slice. An example in two dimensions is shown in Fig. 4.

It is straightforward to use a vector formalism, yielding

$$\tilde{S}(\vec{x}) = 2\pi \int_{\vec{k}} S(\vec{k})\cdot e^{-i\cdot\vec{k}\cdot\vec{x}} d\vec{k} \tag{32}$$

In reality, a discrete Fourier transform (DFT) is employed:

$$\tilde{S}(\vec{x}) = 2\pi \sum_{\vec{k}} S(\vec{k})\cdot e^{-i(\vec{k}\cdot\vec{x})} \left|\Delta\vec{k}\right| \tag{33}$$

This discrete sampling leads to a finite possible image volume. The maximum image volume which can be encoded depends on the spacing of sampled points in k-space. The “field of view” in one direction is

$$FOV = \frac{1}{\Delta k} \tag{34}$$

The k-space formalism is a successful concept for MR imaging. It easily demonstrates that, to acquire one volume in image space, one has to encode a corresponding “volume” in k-space. In principle, the way in which the k-space is sampled in temporal and “k-spatial” order is arbitrary. There exist many different approaches. The most important ones for this thesis are discussed in chapter (2.2).

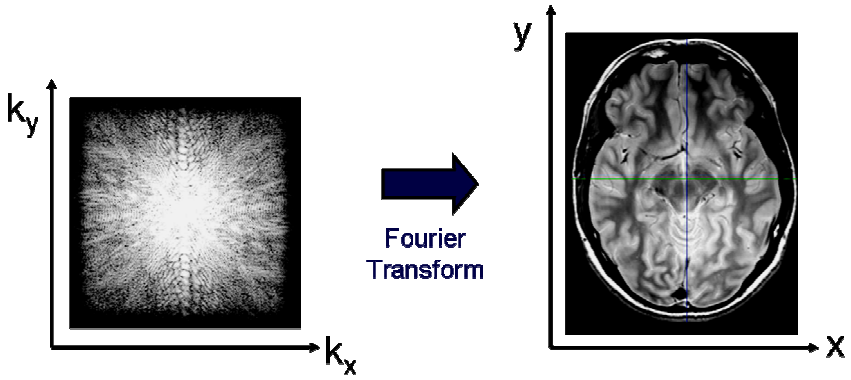

Fig. 4: Two-dimensional k-space acquisition; the corresponding fourier transform is a T2-weighted brain image

The center of k-space with frequency $\vec{k} = 0$ corresponds to the lowest frequency and represents the total sum of magnetization. At small frequencies, the major part of the image signal is situated. Higher k-space coordinates, i.e. higher frequency components, correspond to the finer image details. The image resolution d in one direction is therefore governed by the highest k-space frequency which is acquired, $k_{\max}$:

$$d = \frac{1}{2\pi \cdot k_{\max}} \tag{35}$$

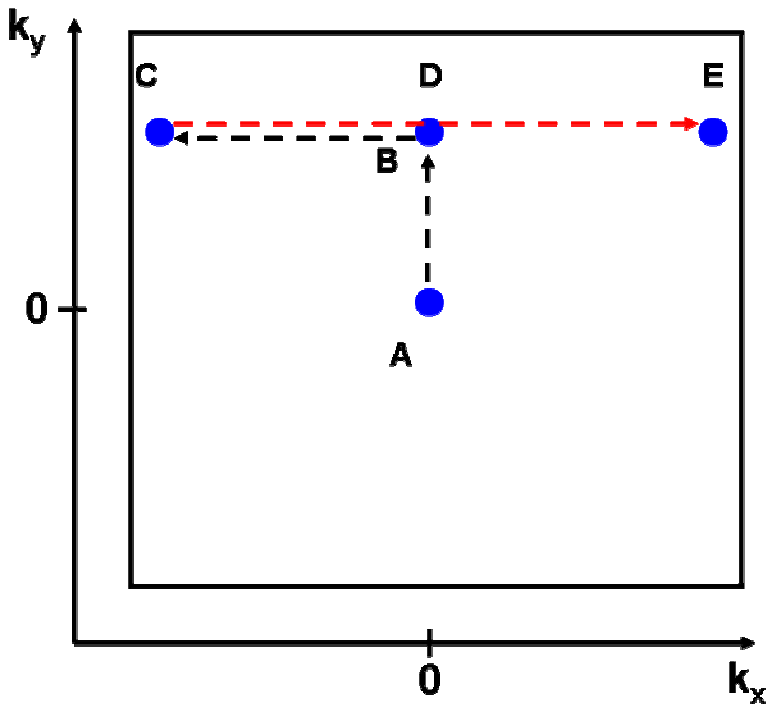

Fig. 5: Concept of spatial encoding in two dimensions in k-space, and acquisition of one Fourier line (red): Beginning in the k-space center A, the phase encoding gradient prepares the coordinate k_y (B). Before the readout, a gradient in the negative k_x direction prepares C in k-space. The readout gradient sweeps the system to E. Simultaneously, signal is acquired at discrete time points (red arrow). The k-space center is reached again during readout at D, where a gradient echo can be observed. For the encoding gradients, cf. Fig. 4.

2.2.3 Gradient echo and spin echo sequences

Magnetic field gradients used for image acquisition also lead to dephasing and thus, smaller signal. This is the reason that the highest signal intensity is acquired at $\vec{k} = 0$, in the k-space center. To get the maximum signal, it is therefore desirable to acquire the k-space center on the maximum of the spin echo.

Independently of the signal evolution due to susceptibility effects, the magnetization can be dephased by applying gradients. After applying the inverse gradient, the magnetization is rephased again, i.e. the k-space center is reached again, and a gradient echo is formed. This is usually done in a gradient echo sequence when a Fourier line is acquired (cf. Fig. 5). The magnetization is dephased in x direction before the readout, which therefore starts at the edge of k-space. The readout gradient rephases the mag-

netization during the acquisition. At the middle of the line, the rephased magnetization forms a gradient echo (Fig. 6, (b)) , before it is dephased again towards the opposing edge of k-space.

In a spin echo sequence, a 180° refocusing pulse is applied before readout. The Fourier line is encoded when the spin echo occurs. A schematic drawing is shown in Fig. 6. (a) corresponds to the spin echo sequence, where a spin echo is formed after TE. (b) shows a gradient echo sequence and the formation of a gradient echo at TE.

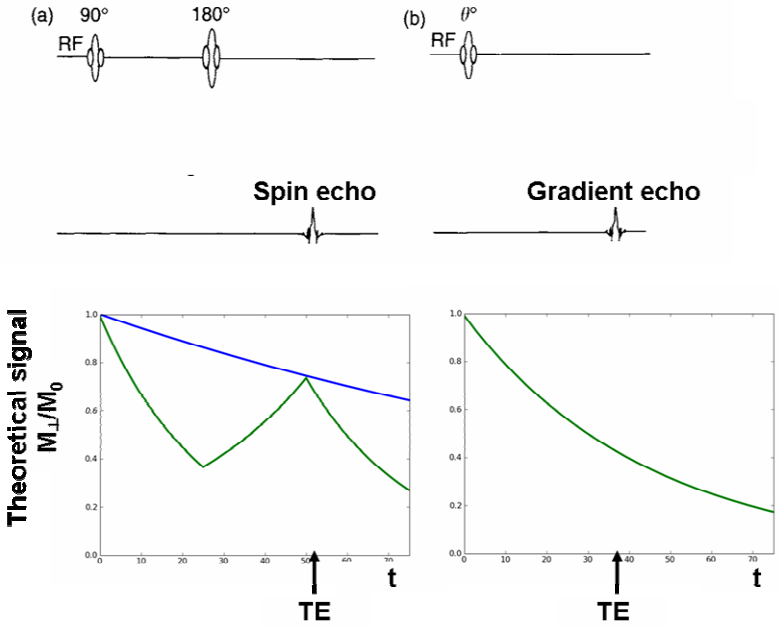

Fig. 6: Schematic drawing of a spin echo (a) and a gradient echo sequence (b), taken from [Bernstein et al. - 2004]. Below, theoretical signal evolution (without gradients applied) is shown (green curve).

An advancement of the spin echo sequence is the Turbo Spin Echo (TSE) readout. Instead of one spin echo, a whole spin echo train is prepared by applying several refocusing pulses. On each spin echo, another Fourier line can be encoded. The theoretical transverse signal development is depicted in Fig. 7.

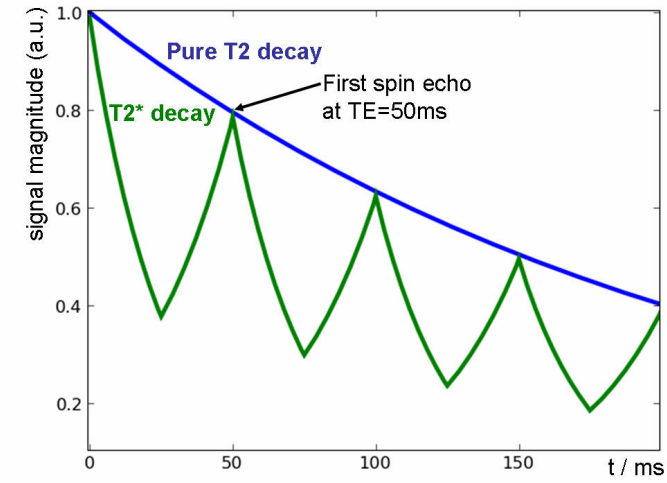

Fig. 7: Schematic signal magnitude during a spin echo train. T2=220ms, T2'=30ms; with refocusing pulses at 25, 75, 125 and 175ms; the first spin echo occurs at TE=50ms.

2.2.4 EPI – Echo Planar Imaging

Echo Planar Imaging (EPI) is a 2d fast imaging technique which has already been developed in 1977 by Sir Peter Mansfield [Mansfield, Maudsley - 1977]. The idea is to acquire one whole slice of k-space after magnetization preparation. The sequence starts off in a corner of the k-space slice. After the acquisition of the first line along k_x, the next Fourier line is prepared by a "blip", a small gradient in phase encoding direction. From there, the next line is acquired in reverse direction. This is repeated n times until the whole slice is acquired. This technique allows the acquisition of a slice in less than 100 ms. A pulse diagram is shown in Fig. 8, the corresponding k-space encoding scheme in Fig. 9.

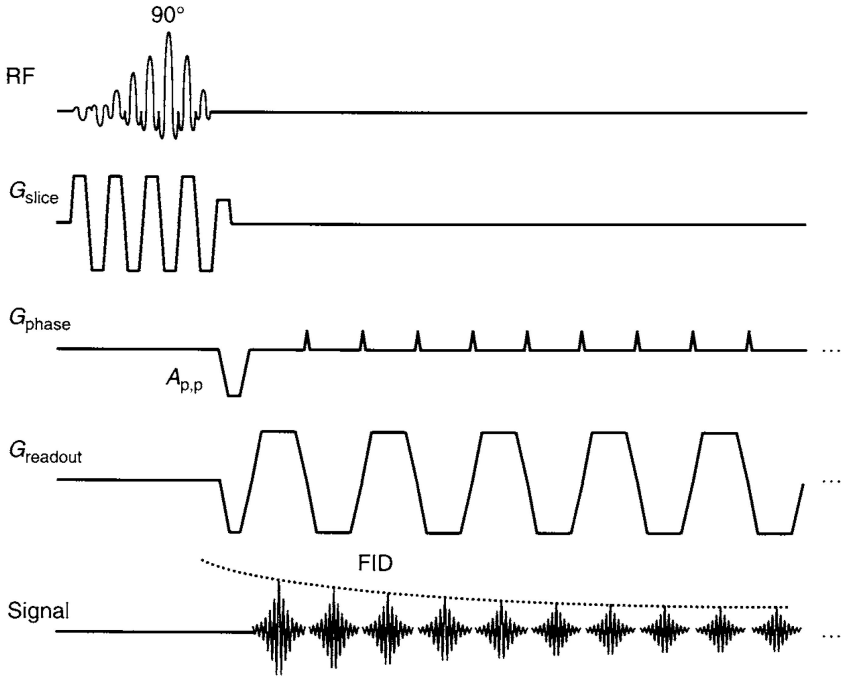

Fig. 8: EPI pulse diagram. The phase encoding consists of small “blips” which move to the next k-space line. During each line acquisition, a gradient is observed. Image taken from [Bernstein et al. - 2004].

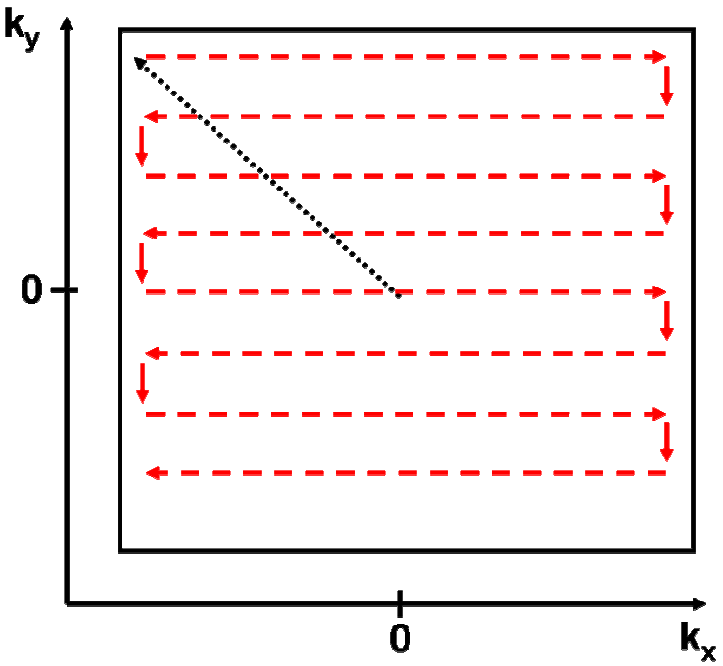

Fig. 9: EPI k-space encoding scheme. After an initial preparation (black arrow), line acquisitions are done (red dashed arrows). In each line at $k_x = 0$, the spins are rephased in respect to k_x, and a gradient echo is formed.

2.2.5 3D-GRASE: Gradient and Spin echo

The acronym GRASE stands for Gradient and Spin Echo and was first proposed by Oshio and Feinberg in 1991 [Oshio, Feinberg - 1991]. 3D-GRASE is a variant which was presented later and is a very fast 3D imaging technique in single shot [Günther et al. - 2005]. After the magnetization preparation, a spin echo train is prepared by applying a train of refocusing pulses. The basic idea of 3D-GRASE is to acquire one EPI readout on each spin echo, while always preparing another k-space partition in z direction. The center of k-space in x-y-direction of each partition is sampled on the occurrence of a spin echo, thus acquiring maximal signal at k-space-frequencies containing the maximum contrast (Fig. 10).

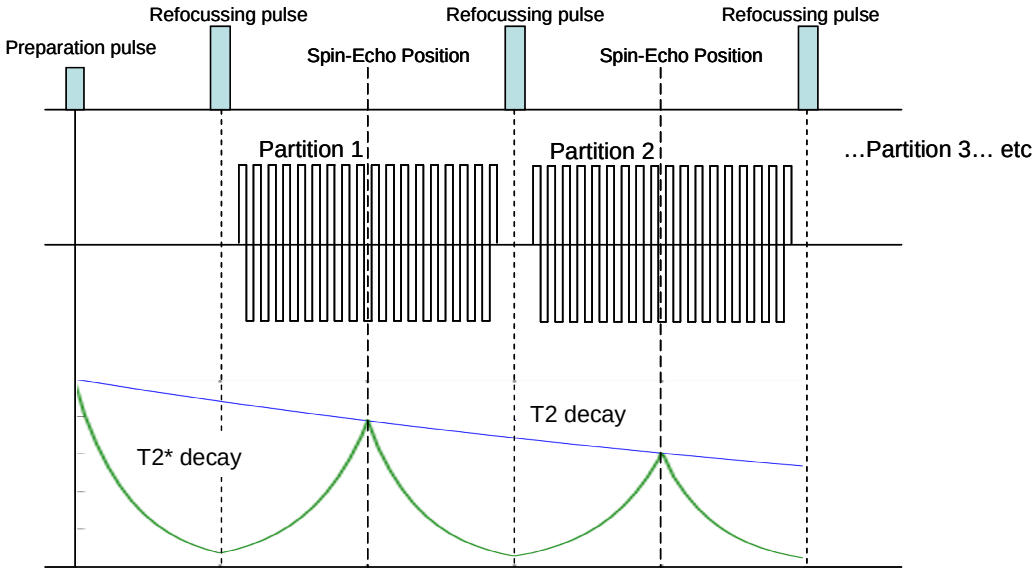

Fig. 10: Signal evolution and 3D-GRASE readout.

Between each two refocusing pulses, another partition is encoded. With a centric reordering scheme, the first acquired partition is the central k-space partition. Afterwards, the next upper and lower partitions are encoded, in alternating order. A k-space slab is shown schematically in Fig. 11. The center of k-space is therefore acquired on the first spin echo, at TE .

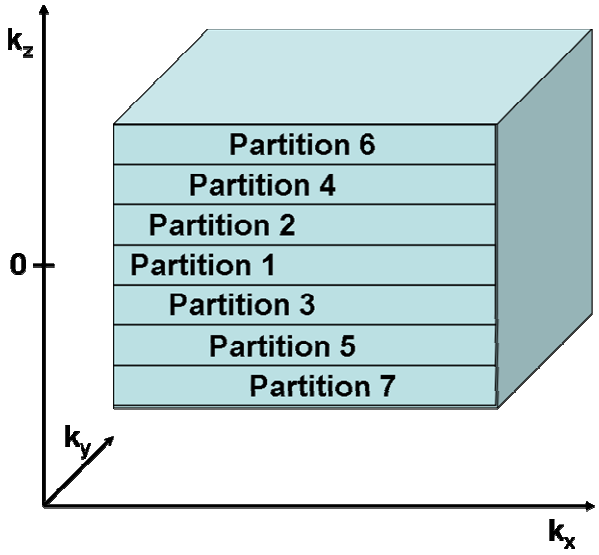

Fig. 11: Schematic k-space slab with 3D-GRASE centric encoding. The partitions in z-direction are acquired alternating, beginning in the k-space center. For the temporal order, cf. Fig. 34.

2.2.6 SEPI: Spiral Echo Planar Imaging

The EPI and 3D-GRASE readout schemes have the advantage that acquired data points in k-space lie on a Cartesian grid. This allows a simple image reconstruction by Fourier transformation. A disadvantage of the EPI concept are distortions along the phase encoding direction due to phase accumulation. Also, for tissue with very short T2*, a technique would be preferred which can realize shorter echo times.

A technique which tackles these topics is the spiral readout. The idea is to sample the k-space in the k_x-k_y-plane along a spiral trajectory. Starting in the k-space center, sinusoidal k_x and k_y gradients are switched, simultaneously to the signal acquisition. This way, signal is sampled along a spiral trajectory in k-space. This technique was first published by Ahn et al. [Ahn et al. - 1986] and named SEPI (“spiral scan echo planar imaging”).

For uniform spiral k-space coverage it is desired that the spiral trajectory has equidistant step size in radial direction. This is true for an Archimedean spiral where the radial and the angular components are proportional:

$$\vec{k}(t) = A \cdot \theta(t) \cdot e^{i\theta(t)} \tag{36}$$

The k-space coordinates from Equ. (29) can be converted to yield the gradient shapes:

$$\vec{G}(t) = \frac{1}{\gamma}\frac{d}{dt}\vec{k}(t) \tag{37}$$

Following the notation of magnetic field and magnetization, the transverse gradients used to encode the transverse k_x-k_y-plane can be expressed as complex number:

$$G_\perp(t) = G_x(t) + i \cdot G_y(t) \tag{38}$$

Combination of the above equations yields

$$G_\perp(t) = \frac{A}{\gamma}\left(\dot{\theta}(t)e^{i\theta(t)} + \theta(t)\cdot i\dot{\theta}(t)e^{i\theta(t)}\right) = \frac{A}{\gamma}\left(1 + i\theta(t)\right)\cdot\dot{\theta}(t)e^{i\theta(t)} \tag{39}$$

The geometric coverage of k-space doesn't depend on the time parameterization. For the simple case with $\theta(t) = t$, gradient shapes and k-space coverage are shown schematically in Fig. 12.

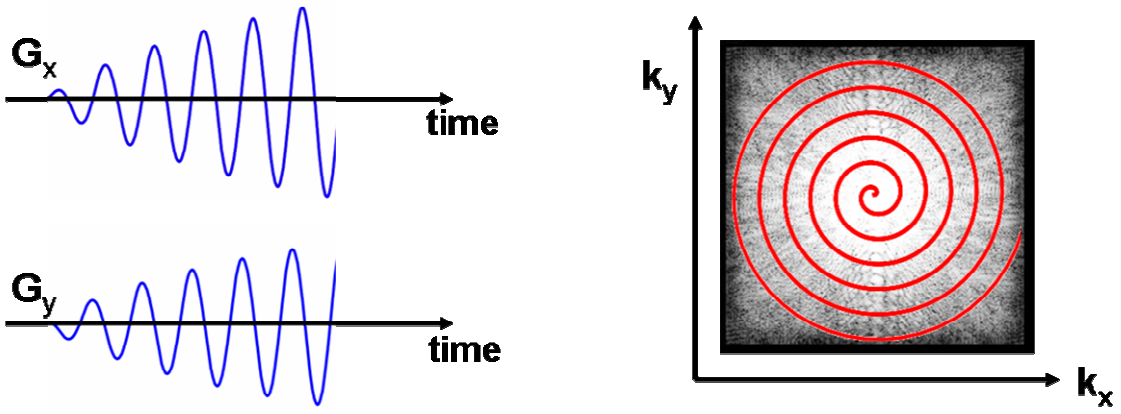

Fig. 12: Gradient shapes and k-space coverage with an Archimedean spiral;

Starting the trajectory in the k-space center (with $G_x, G_y = 0$) like in the example above allows a substantial reduction of TE (i.e. the k-space center is sampled at t=0). Still, signal decays with larger k-space values. In probe tissue with large susceptibility inhomogeneities and fast T2* decay, this leads to blurring artifacts. A possibility to reduce imaging time during one acquisition is the use of segmented spirals or "interleaved multishot spirals". In this approach, the sampling of k-space is done in several repeti-

tions or “segments”. With n segments, acquisition of one segment is reduced by n compared to a single shot spiral readout. The segments are rotated in respect to each other to sample the k-space homogeneously. A visualization of the k-space coverage with four segments is shown in Fig. 13. The data of the segments have to be recombined before reconstruction.

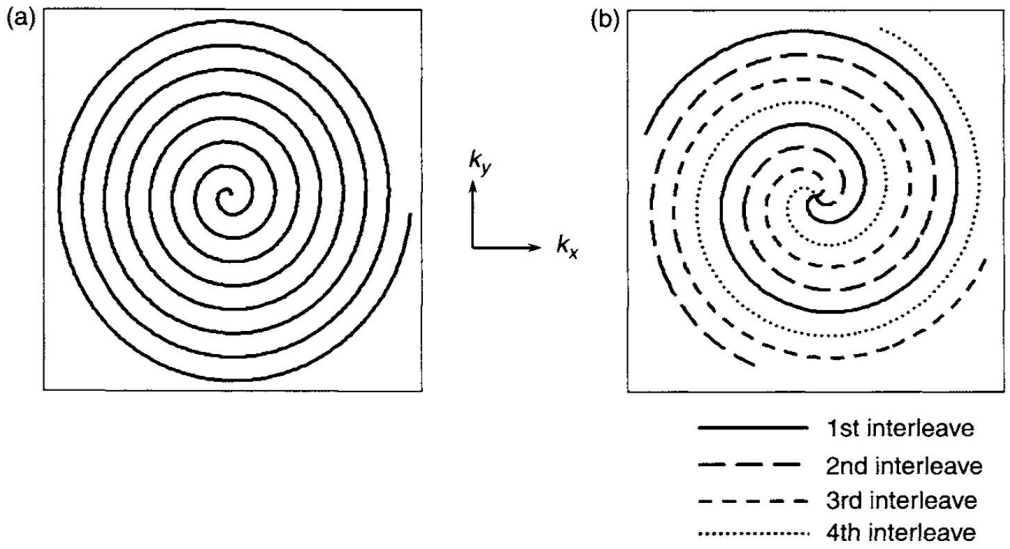

Fig. 13: Principle of segmented spiral readout; The k-space is acquired in several measurements. The data is combined before the fourier transform. From [Bernstein et al. - 2004]

The acquired raw data from spiral scans has to be resampled to a Cartesian coordinate system before the Fourier transform. A common method is regridding, where a weighting function is used to calculate the signal for a fixed Cartesian grid. This is computationally expensive but it is feasible on modern scanner systems.

The system response on a point-like signal source (a delta function) is called the “point spread function”. After k-space encoding and Fourier transform, the delta function smears out, which means that part of the signal is visible in other voxels surrounding the signal source. This is due to a finite T2*, which leads to an additional phase shift and so, to a spatial shift in image space. The effect depends on the encoding mechanism and acquisition time. For typical parameters, a simulation has been done in [Amann - 2000]. The resulting surface plots show the signal resulting magnitudes depending on the image coordinates, in Fig. 14. The main imaging parameters are the same (matrix size,

acquisition time). While on the left, the spiral readout only leads to blurring around the point-like source, the Cartesian EPI readout on the right shows distortions in the of the read and phase directions.

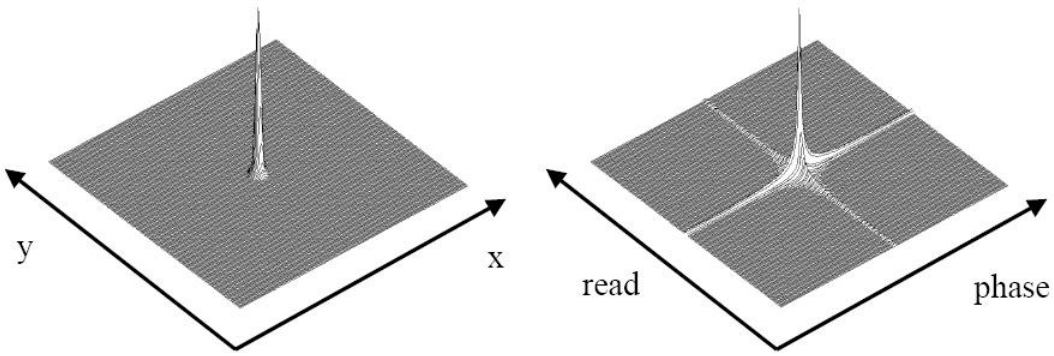

Fig. 14: Surface plots of calculated pointspread fuctions of a single shot spiral sequence (left) and a single shot EPI (right). Matrix size is 256 x 256, acquisition time 3 x T2*; from [Amann - 2000].

Applying spiral gradients allows the encoding in two dimensions. To extend the spiral readout to three dimensions, the easiest way is to realize a “stack of spirals”. Like in the extension of EPI to 3D-GRASE, where EPI readouts are stacked in k_z-direction, a stack of spirals contains several spirals encoding in k_x and k_y direction, while each spiral is prepared with different k_z gradients.

2.3 Arterial Spin Labeling

Arterial Spin Labeling (ASL) is a non-invasive imaging technique capable of measuring perfusion. This is a great advantage over contrast agent based methods. The basic principle of ASL is to employ the blood water itself as contrast agent to measure perfusion. The longitudinal magnetization of the blood water is prepared proximally of the perfused regions, i.e. usually it is inverted by a 180° pulse. Subsequently, the prepared blood flows to the readout region and the delivered magnetization can be acquired after an inflow time TI by common readout modules. (TI is equivalent to the inversion time in the last chapters, but has the additional meaning of inflow in ASL.) ASL usually involves the acquisition of a label image (with preparation of inflowing blood water spins) and a control image (without preparation), the difference of which is the perfusion weighted output image.

2.3.1 Two basic techniques: Continuous and Pulsed Arterial Spin Labeling

The concept of Arterial Spin Labeling was first proposed by [Williams et al. - 1992]. In this original approach, blood water is labeled by using a flow-driven adiabatic inversion. This labeling technique will flip the magnetization of water molecules with a certain velocity, while stationary tissue is saturated. (For a detailed description, cf. [Bernstein et al. - 2004].) The rf pulse length is typically greater than one second. The labeling efficiency is reduced by geometrical imperfections of the rf pulse and pulsatile velocity differences of the blood flow and ranges from 80-95%. Since there is always “fresh” labeled blood delivered, the readout region will tend to reach a steady state. This technique is known as Continuous ASL (CASL).

An alternative is Pulsed ASL (PASL), where the magnetization is prepared in a large region by applying a short inversion pulse [Edelman et al. - 1994]. The labeling efficiency is generally higher then in CASL. However, while the blood is flowing into the readout region, the prepared magnetization decays with T1. This leads to smaller signal when longer inflow times are chosen.

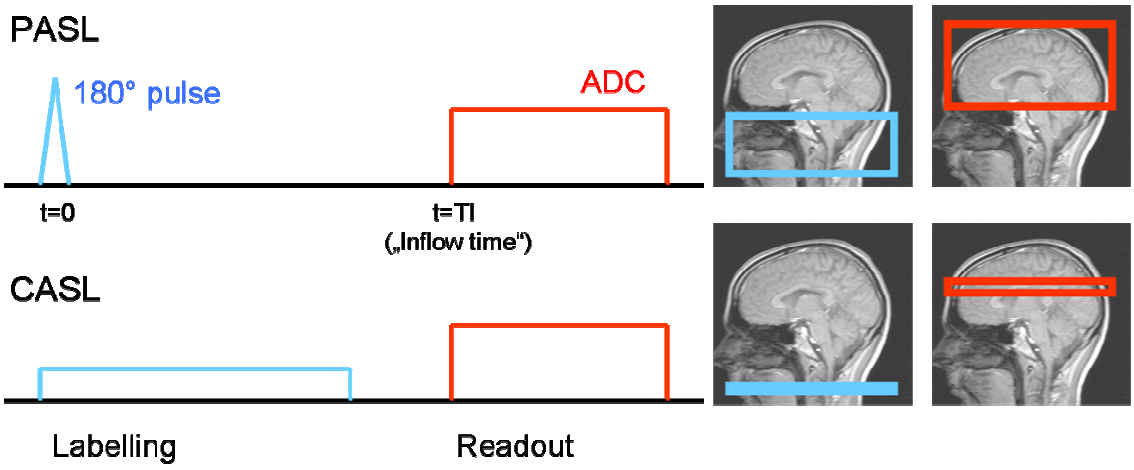

Fig. 15: Sketch of the two basic ASL techniques; in PASL, a larger region is labeled for a short time; the readout module can in both cases be chosen arbitrarily 2- or 3-dimensional

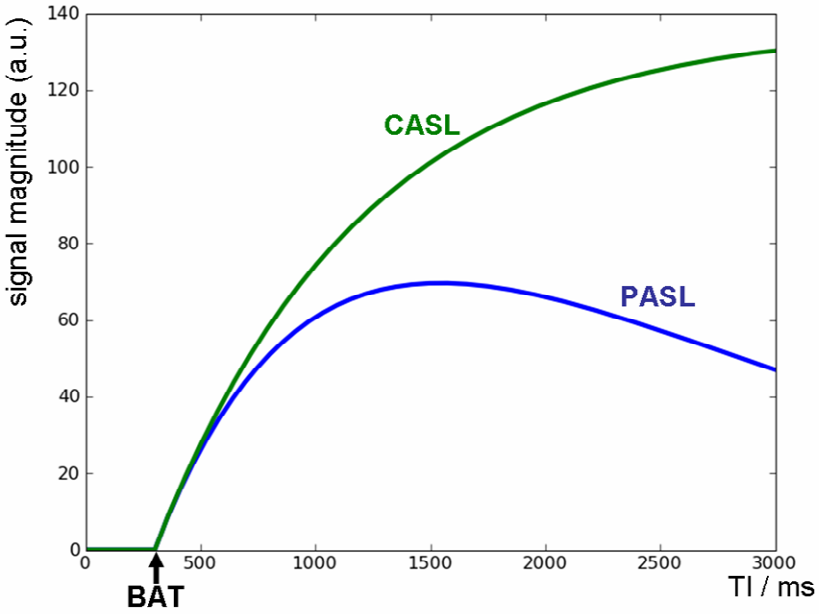

Fig. 16: Theoretical ASL signal from one voxel depending on the inflow time TI; labeled blood arrives in the voxel at TI=BAT (bolus arrival time); at later TI, the PASL curve shows T1 decay while CASL reaches a steady state.

2.3.2 Blood flow and perfusion: the General Kinetic Model

Blood flow is measured in units of ml/min and denotes the amount of blood per time flowing through a vessel. Perfusion is the amount of blood delivered to a certain amount of tissue, commonly measured in ml/100g/min.

The delivery of blood in Arterial Spin Labeling experiments can be described by the General Kinetic Model [Buxton et al. - 1998]. A good review is given by [Petersen et al. - 2006]. It includes the delivery function $c(t)$, the residue function $r(t)$, which describes the washout of labeled blood from the voxel, and a term $m(t)$, which describes the decay of magnetization. The observed signal in a voxel is the convolution of the delivery function with the tissue response $r(t) \cdot m(t)$:

$$S(t) = 2 \cdot M_{a,0} \cdot CBF \cdot \int_0^t c(\tau) \cdot r(t-\tau) \cdot m(t-\tau) d\tau \tag{40}$$

CBF: Cerebral blood perfusion
$M_{a,0}$: Equilibrium longitudinal blood magnetization

The integral can be solved analytically if simple assumptions are made. In the most common approach for pulsed Arterial Spin Labeling, the delivery function starts when the blood bolus arrives in the voxel, at BAT ("bolus arrival time"), and ends after the bolus length BL, at $BAT + BL = \tau_d$. BAT highly depends on the brain region. Outflow is modeled as an exponential decay assuming a certain probability of the water molecule of leaving the voxel at time t. $m(t)$ simply represents the longitudinal relaxation in the voxel. The describing functions are modeled as:

$$\begin{aligned} c(t) &= \delta(t - BAT) \cdot \delta(\tau_d - t) \cdot \alpha \cdot e^{-t \cdot R1_{bl}} \\ r(t) &= e^{-CBF \cdot t / \lambda} \\ m(t) &= e^{-t \cdot R1_{ex}} \end{aligned} \tag{41}$$

where α is the inversion ratio (the proportion of spins actually flipped by the 180° pulse), CBF the perfusion (usually measured in ml/100g/min), λ the tissue partition constant (the amount of tissue per volume, for grey matter approx. 0.9, cf. e.g. [Tofts -

2003]), and $R1_{bl}$, $R1_{ex}$ relaxation constants in arterial blood and extra-vascular space (i.e. tissue), respectively.

Solving Equ. (40) yields

$$S(t) = \begin{cases} 0 \\ \dfrac{-2 \cdot a \cdot M_{a0} \cdot CBF}{\delta R} e^{-R1_{bl} \cdot t} \left(1 - e^{-\delta R \cdot (t - \tau_a)}\right) \\ \dfrac{-2 \cdot a \cdot M_{a0} \cdot CBF}{\delta R} e^{-R1_{bl} \cdot \tau_d} \left(1 - e^{-\delta R \cdot (t - \tau_a)}\right) \cdot e^{-R1_{app} \cdot (t - \tau_d)} \end{cases} \quad \text{for} \quad \begin{cases} t < BAT \\ BAT \le t < \tau_d \\ t \ge \tau_d \end{cases} \quad (42)$$

$$R1_{app} = R1_t + \frac{CBF}{\lambda} \qquad \text{Apparent longitudinal relaxation}$$

$$\delta R = R1_a - R1_{app} \qquad \text{Relaxation difference}$$

The theoretical inflow curve for $t < \tau_d$ is shown in Fig. 16.

This is, however, only a basic model describing blood delivery to a voxel by uniform flow from one source. It describes the inflow of the blood through the vasculature, but assumes an immediate transfer of the water molecules from blood to tissue space, as soon as a water molecule arrives in the voxel (“fast exchange”). The choice of function $m(t)$ in Equ. (41) does not include multi-compartment or transfer effects. The solution can therefore be considered a single compartment model. However, such effects can be included in $m(t)$ before solving the convolution.

2.3.3 Magnetization Transfer: STAR and FAIR

Magnetization transfer (MT) is an effect which, in ASL, can lead to magnetization of stationary brain tissue in the readout slab. Water protons bound to macromolecules have a much broader frequency range (cf. Fig. 17) than free water protons. A labeling pulse, which is off-resonant in respect to the readout slab, can therefore still affect magnetization of the bound water molecules there. The two pools can exchange magnetization, via water diffusion or spin-spin interaction. Thereby, the magnetization of the free water protons is modified, and the free water proton magnetization will contribute to the readout signal.

The MT effect is used in MT-imaging, where it is used to estimate the bound water pool size, which hints to the presence of macromolecules. This can point to pathological changes in tissue composition.

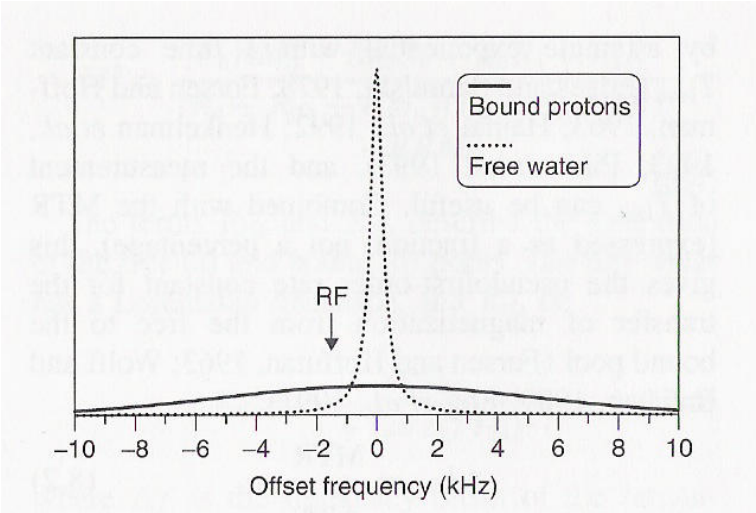

Fig. 17: Symbolic representation of the free (dotted line) and bound (solid line) water proton pools in brain tissue. An off-resonant rf pulse can excite bound water molecules, which can exchange their magnetization with the free water pool. Image taken from [Tofts - 2003].

In ASL, the MT effect is an important detail to be considered. The RF inversion pulse, which is off-resonant to the readout region, is only needed for the label acquisition. MT effects, which occur during labeling, but not during the control image, contribute dramatically to the perfusion weighted difference image. Therefore, methods to compensate MT effects had to be developed.

In the first PASL publication presented above, the idea was to apply the inversion pulse also in the control acquisition, but distal to the readout region. It is assumed that the MT effects are symmetric and therefore cancel out in the difference image. This is of course only practical for thin imaging slices, not for larger readout slabs. The technique is known as STAR (signal targeting with alternating radio frequency, after [Edelman et al. - 1994]).

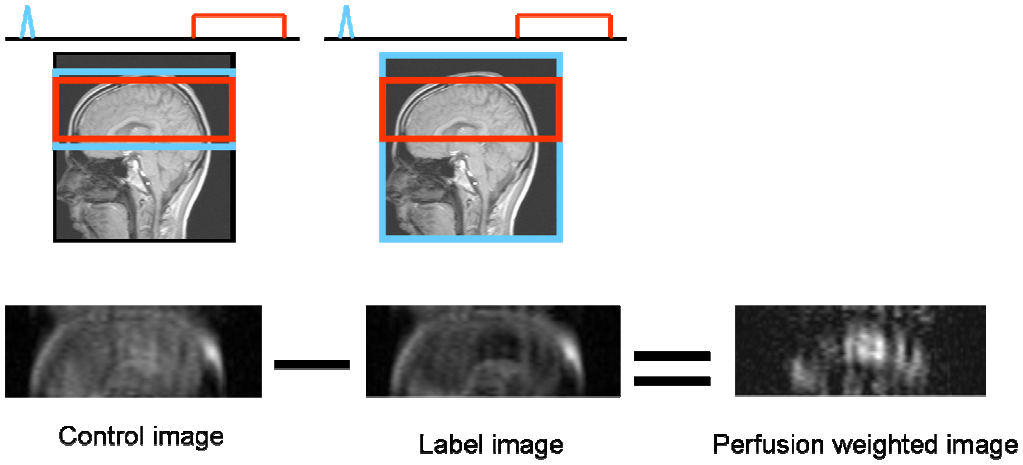

Fig. 18: The FAIR labeling scheme

One of the subsequently proposed MT compensation techniques is FAIR (flow alternating inversion recovery, [Kwong et al. - 1995] and [Kim - 1995]) Here, in the labeling case, a global inversion pulse is employed, thus labeling inside and outside the readout region. For the control image, a slice selective inversion pulse is used, inverting only the magnetization in the readout slab. In the difference image, this cancels out and the prepared magnetization of inflowing spins remains. FAIR is a technique which can also be used for larger readout slabs and 3D imaging. Label and control are also known as non-selective and slice selective acquisitions in FAIR.

2.3.4 Background suppression

At two time points between inversion and readout, additional global inversion pulses are applied as background suppression pulses. The timing of the pulses is optimized to null the tissue signal with a certain T1 at the time of readout TI. A schematic curve of $M_{\parallel}$ is shown in Fig. 19.

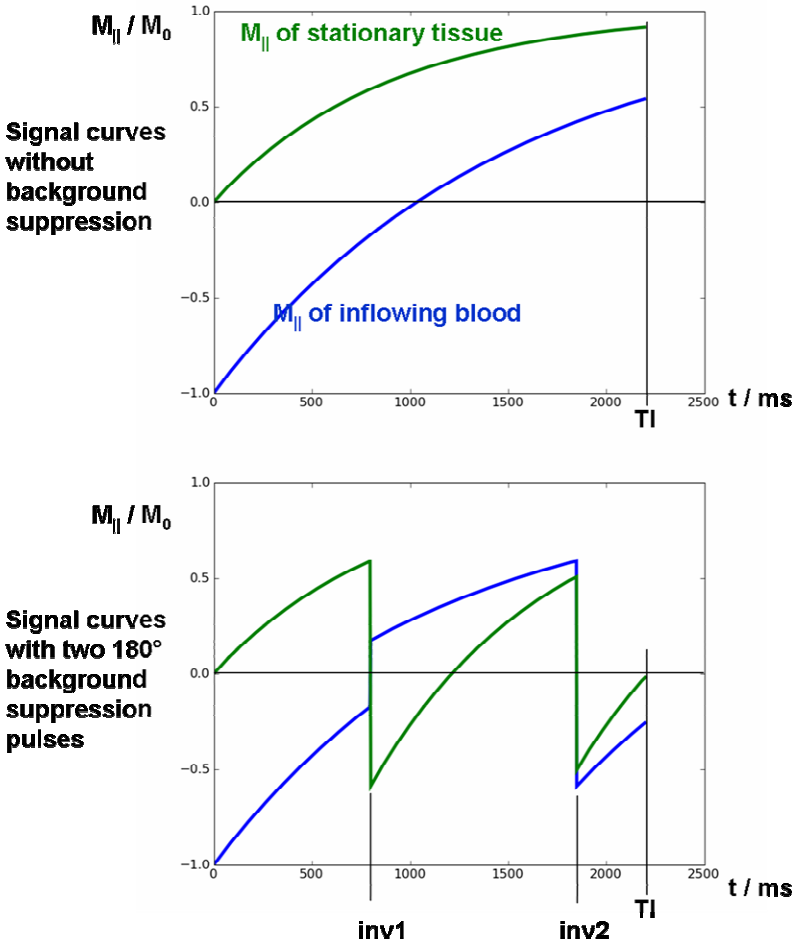

Fig. 19: Schematic magnetization curves with and without background suppression; blood signal starts at $M_{||}$=-1 after inversion and decays with $T1_{blood}$=1500 ms. Tissue signal starts at $M_{||}$=0 after post-labeling saturation and relaxes with $T1_{tissue}$=800 ms.

If one inversion pulse is employed it can be optimized to null exactly one characteristic T1. With two pulses, two different T1 tissue types can be nulled simultaneously, with correct choice of the timing, etc. However, there is no analytical solution for the inversion times of arbitrary T1 and TI. The flip angles of the inversion pulses need not be exactly 180°, but can also be optimized for maximal signal suppression [Ogg et al. - 1994].

2.3.5 Effect of varying BAT and Q2TIPS

One crucial point in planning an ASL experiment is the choice of TI. In the above considerations, acquisitions are done at exactly one fixed TI. The resulting difference from the labeled and unlabeled images is perfusion weighted. However, the signal

curves depend on TI (cf. Fig. 16), and also on characteristic properties varying from voxel to voxel. Especially, BAT varies in a large range between brain regions, commonly with differences of up to one second. This leads to underestimation of perfusion in areas with larger BAT. On the other hand, choosing a long TI where all voxels are assumed to be filled with blood, will lead to substantially lower SNR. Thus, the perfusion weighted image is not directly proportional to the real perfusion map. For quantification, errors have to be taken into account and corrected. The effect is depicted in Fig. 20, where the schematic signal curves of three different voxels is shown. The blue and red curves show voxels with same perfusion value, but different BAT. The green curve shows a voxel with half the perfusion. At a chosen inflow time of $TI = 2000\,\text{ms}$, the green signal curve is higher than the red one, despite of the significantly lower perfusion.

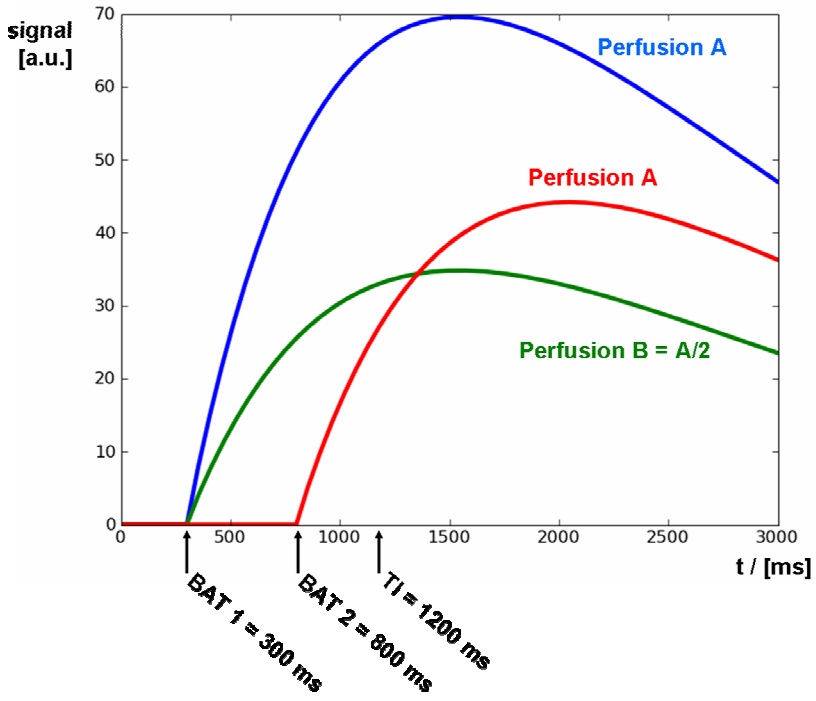

Fig. 20: Characteristic inflow curves of three voxels, with different arrival times and perfusion values.

Wong et al proposed to apply saturation pulses (called Q2TIPS or QUIPSS II – "**Qu**antitative **i**maging of **p**erfusion using a **s**ingle **s**ubtraction, second version") after a certain time BL ("bolus length") to truncate the blood bolus. This circumvents fresh labeled

blood from flowing into the imaging slab for times $t > BL$. Is BL chosen such that $TI - BL > BAT$ for all voxels, all voxels are subject to the same temporal length of the inflow bolus and the effects of varying BAT cancel out.

The idea of the application of Q2TIPS in the above ASL scheme is slightly different. In PASL, the bolus of inverted blood is in principle arbitrarily long, spatially and temporally. In practice, however, because of imperfect slice profiles and coil geometry, blood far away from the readout center will not be perfectly inverted. The truncation of the bolus at a certain time BL is therefore a mean to prepare a known bolus shape.

Besides quantification, there is another positive effect of applying the Q2TIPS pulses directly before readout. Any signal from outside the readout slab which could disturb in the image acquisition is saturated. This is especially important because the labeling pulses are applied outside the readout region and would lead to image artifacts.

2.3.6 An optimized pulsed ASL labeling and readout scheme

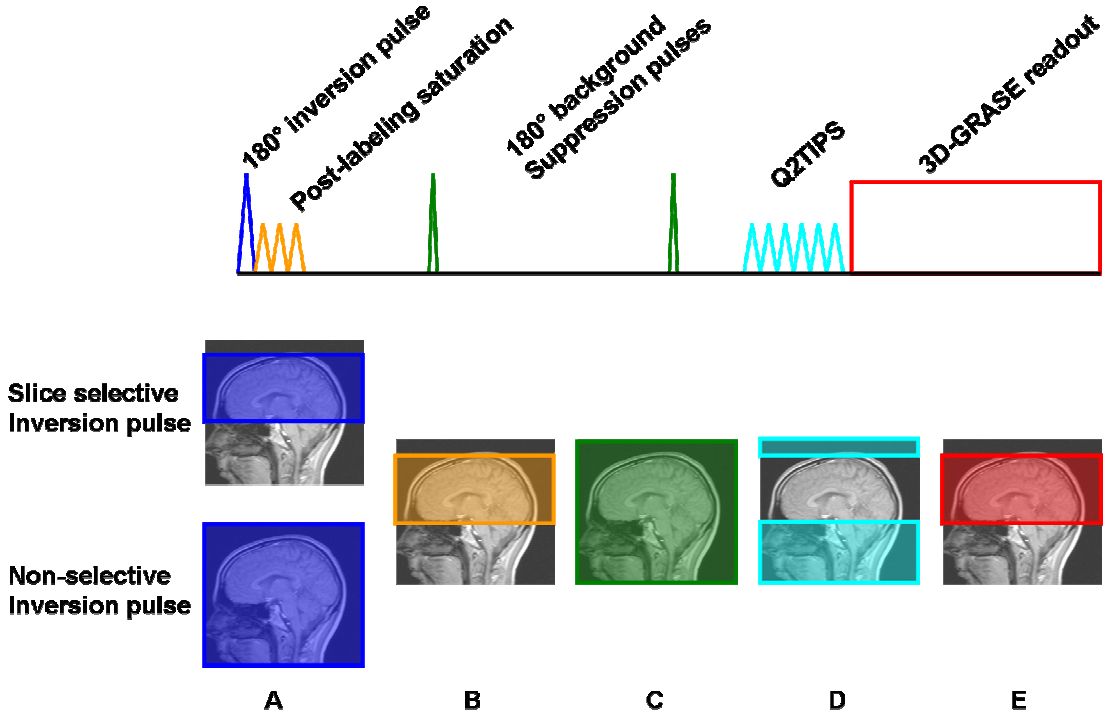

Fig. 21: Schematic pulse diagram of the optimized PASL-FAIR scheme
A: The inversion pulse is slice selective in case of the control image and non-selective for the labeling image.
B: After inversion, the readout region is saturated. This prepares a homogenous uniform

magnetization in the readout region and also saturates any possible MT-effects there.
C: Stationary tissue is suppressed by two background suppression 180° pulses which are optimized to null tissue signal at t = TI.
D: At t=BL (bolus length), the blood bolus is truncated by application of Q2TIPS saturation pulses. Also, signal from outside the readout slab is suppressed.
E: At t = TI, a 3D-GRASE single shot readout module acquires an image with whole-brain coverage.

In 2005, Günther et al. presented an optimized ASL preparation scheme in conjunction with a 3D-GRASE readout module [Günther et al. - 2005]. As mentioned above, care has to be taken to reduceor MT effects. Another basic issue in ASL is signal strength. The blood signal compared to tissue signal makes only a few percent. Both drawbacks are addressed in the presented approach.

Fig. 21 shows a schematic pulse diagram of the ASL sequence. This scheme is run twice, for the label- and control image. In both cases a 180° inversion pulse is applied to prepare the ASL signal. Like in the FAIR scheme, in one case the pulse is slice selective so none of the inflowing blood spins is labeled. Afterwards, post-labeling saturation pulses are applied. In the slice selective case, all previously prepared magnetization is saturated, while in the non-selective case only magnetization outside the imaging slab remains. The saturation also suppresses any MT effects in the readout region.

2.3.7 ASL time series

As mentioned above, varying *BAT* is a source of error in perfusion quantification. While there are ways to correct for these errors in a certain *BAT* range (like Q2TIPS), it is not sufficient in many cases. Especially cerebro-vascular diseases can lead to an uncommonly large *BAT* in affected areas. In these cases, it is desirable to get a detailed view on the dynamics of blood inflow. A solution to that is to acquire the perfusion weighted ASL images repeatedly with varying inflow times, thus sampling a time series of the signal evolution.

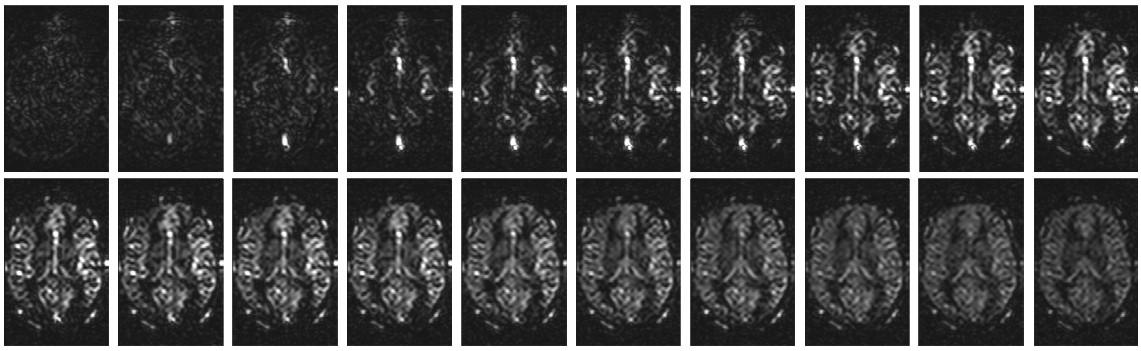

Fig. 22 ASL time series dataset; Inflow time steps range from *TI* =100 ms to *TI* =2000 ms, with a step size of 100 ms. In the first images, voxels with larger vessels appear bright. As blood is delivered to the tissue via the capillaries, on the later time steps the signal is more uniformly distributed in the tissue.

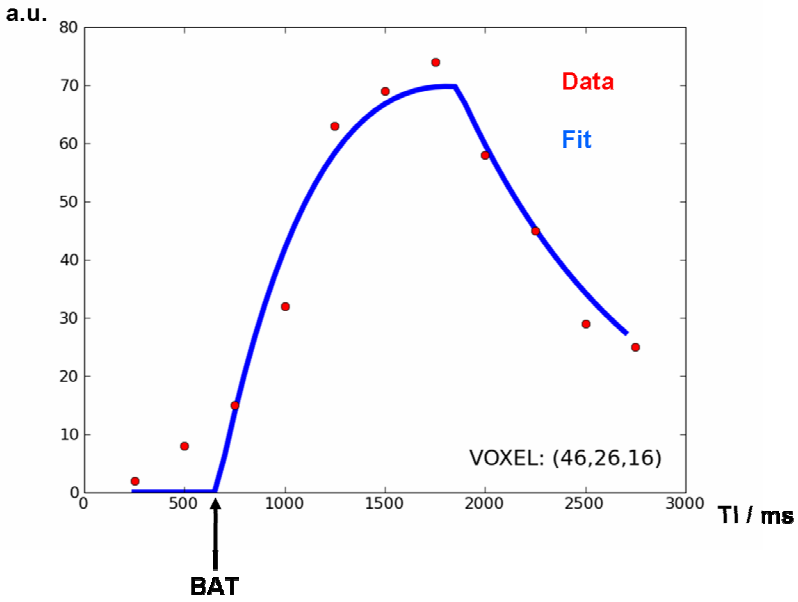

Fig. 23: Typical data points from one voxel. The Buxton model from Equ. (40) can be fitted to the voxel data along the inflow time axis.

Typical images and data are shown in Fig. 22 and Fig. 23. The model fit yields perfusion values which also depend on the fitted bolus arrival times.

2.4 Advanced physiological perfusion aspects

The current thesis will address new aspects of ASL signal contrasts and readouts, which might reveal insight in physiological processes. Previous work in this direction has been done in other groups, which will be summarized here. Especially, there has been work on more-compartment models which include permeability aspects, but only looking at T1.

2.4.1 ASL two-compartment models

In the fast exchange model from Equ. (42), the assumption has been made that blood water, due to its small size, can pass the blood brain barrier unhindered and is distributed by pure diffusion. The characteristic diffusion time of water molecules on a capillary diameter length scale can be estimated to about 2-7 ms [Yablonskiy, Haacke - 1994]. The typical time scale of ASL experiments is two orders higher and thus, fast exchange would be a good approximation. However, the assumption of infinite permeability of the blood brain barrier to water is not realistic, and indeed there exists evidence of restricted water exchange. Permeability is commonly measured in PET as permeability surface area product PS, which is simply the permeability times the entire surface of the membrane in the volume of interest. In PET experiments, finite extraction fractions suggests a PS of about 150 ml/100g/min for grey and white matter [Raichle et al. - 1983].

The assumption of a restricted water exchange and the fact that there are significant differences in T1 between blood and tissue gives need to incorporate the two different compartments in the model. A two compartment theory for ASL experiments has been developed in [St Lawrence et al. - 2000]. Other approaches can be found e.g. in [Parkes - 2005] and [Li et al. - 2005].

Lawrence et al. assumed a restricted water exchange which depends on the permeability area surface product PS and the concentration of labeled blood water spins. The concentrations are assumed uniform throughout each compartment.

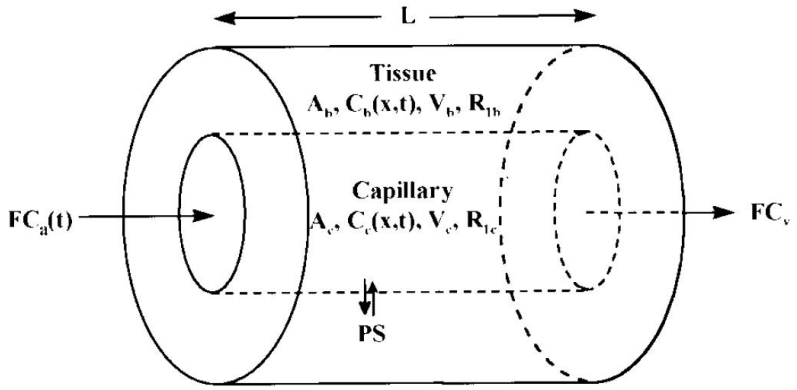

Fig. 24: Sketch from[St Lawrence et al. - 2000].

The continuity equations governing the labeled water concentrations in capillary and extra-vascular space are coupled differential equations of grade one. They uncouple if backflow from extra-vascular to capillary space is neglected. This is a reasonable approximation because the capillary space V_c makes only about 2% of the voxel and the extra-vascular concentration of labeled water will always be close to zero. In the well mixed voxel, the overall uniform concentration will be maximally 2%.

The differential equations are

$$\frac{\partial C_{bl}(x,t)}{\partial t} = -\frac{F}{A_c}\frac{\partial C_{bl}(x,t)}{\partial x} - \frac{PS}{A_c \cdot L}C_{bl}(x,t) - R1_{bl}C_{bl}(x,t)$$

$$\frac{\partial C_{ex}(x,t)}{\partial t} = \frac{PS}{A_{ex} \cdot L}C_{bl}(x,t) - R1_{ex}C_{ex}(x,t) \qquad (43)$$

C_{bl} : Labeled water concentration in blood
C_{ex} : Labeled water concentration in extravascular space
F : Blood flow of labeled spins
A_c : Capillary cross sectional area
A_{ex} : Cross sectional area of the surrounding tissue (assumed tubular)
$R1_{bl}$: R1 of blood
$R1_{ex}$: R1 of tissue
L : Length of the capillary segment

A solution to these equations for real problems isn't straightforward to give because of temporal dependence of the fresh inflow F which corresponds to the delivery function $c(t)$ in the Buxton model (41). However, the impulse residue functions can be given for

the blood and extra-vascular compartments, named $q(t) = r(t) + m(t)$ in comparison to Equ. (41), for times smaller than the capillary transit time:

$$q_{bl}(t) = e^{-\frac{PS}{V_c}t} + e^{-R1_{bl} \cdot t} \tag{44}$$

$$q_{ex}(t) = \frac{1}{\left(1 + \frac{\left(R1_{bl} - R1_{ex}\right) \cdot V_c}{PS}\right)} \cdot \left\{ e^{-R1_{ex} \cdot t} - e^{-\frac{PS}{V_c}t} - e^{-R1_{bl} \cdot t} \right\} \tag{45}$$

Here, $V_c = L \cdot A_c$ is the partial capillary volume in the volume of interest.

However, the effect on the perfusion signal is small. In [Li et al. - 2005], a model has been derived including capillary transit and the consequences for ASL have been discussed. It turns out that in classical ASL perfusion weighted experiments, the permeability is extremely difficult to measure because deviations from a single compartment model occur only at long inflow times, where the SNR is very poor (cf. Fig. 25; Fig. 26 shows typical data).

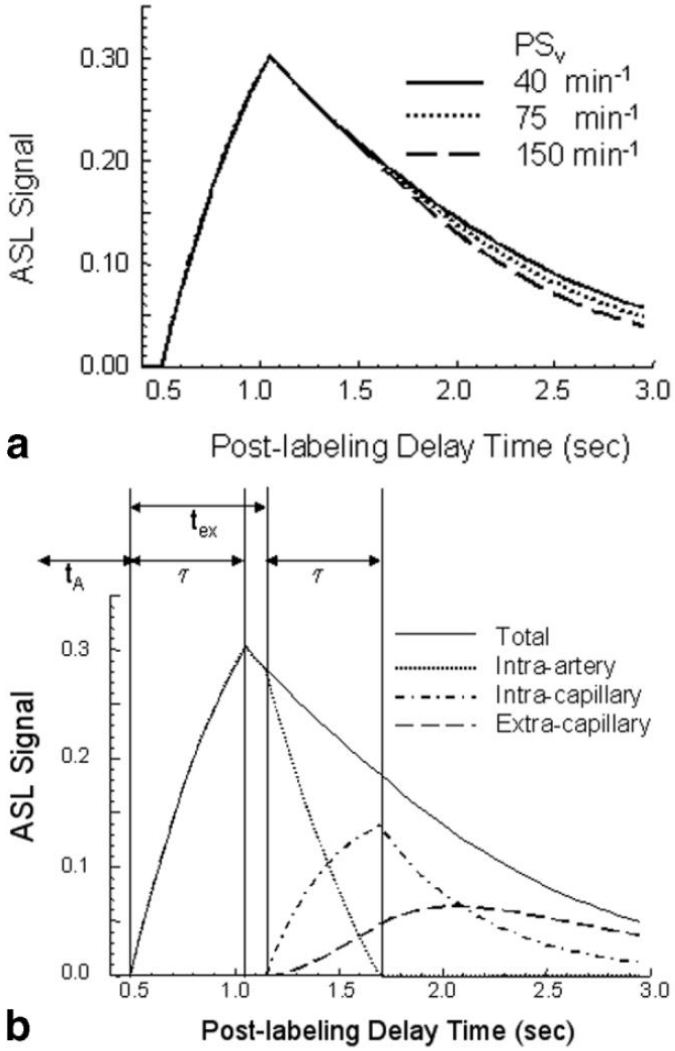

Fig. 25 Figure from [Li et al. - 2005]; In the single-capillary four-phase model derived in this publication, arterial, capillary and tissue phases are considered. The exchange between capillary and tissue is governed by PS (b). The effect of PS on the classic ASL signal is shown in (a).

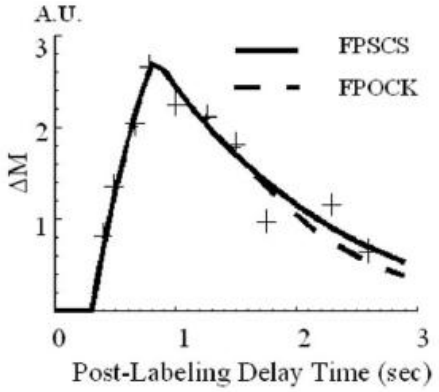

Fig. 26: Direct comparison between two models with fast exchange ("FPOCK", four-phase one-compartment Kety) and restricted permeability ("FPSCS", four-phase single-capillary stepwise model) with typical data points, depicting the difficulty to measure PS based on the T1 weighted signal. From [Li et al. - 2005].

Another interesting approach to estimate the permeability has been done by [Wang et al. - 2007]. He combined ASL with diffusion weighted imaging. In ASL experiments, diffusion gradients have been switched to assess the apparent diffusion coefficients (ADC). The ADC is different in blood plasma, where water can diffuse almost freely, and in tissue where diffusion is hindered by e.g. cell membranes. With increasing inflow time, Wang could show that an increasing part of the signal would originate from tissue space.

2.4.2 BOLD: the effect of deoxygenated venous blood on R2'

Brain activation leads to higher oxygen consumption and to an increase in perfusion. The local change in metabolism is measured in functional MRI (fMRI) experiments, where the activation of certain brain areas by e.g. visual or sensorial stimulation can be observed. Usually, fMRI experiments make use of the BOLD (Blood Oxygenation Level Dependent) effect. The BOLD effect is based on the fact that deoxygenated hemoglobin in the erythrocytes is slightly paramagnetic, in contrast to oxygenated hemoglobin which is isomagetic like the surrounding tissue. Deoxygenated blood therefore leads to local field protuberances around the vessels which can be observed with T2* weighted sequences. With higher oxygenation in a voxel, the dephasing of the measured magnetization decreases, and a higher signal can be observed. The signal changes therefore originate from the characteristics of the venous vessels.

2.4.2.1 BOLD effect in functional activation

Fig. 27 shows a schematic BOLD response curve in a voxel to a stimulus. Generally, time series of T2* weighted images are acquired which sample several response curves (“activation blocks”) alternating with baseline acquisitions. Characteristic properties of the response curve are: an initial dip, the positive BOLD response with an overshoot at the beginning, and a post-stimulus undershoot. The initial dip can be explained by an initial rise in demand of oxygen, leading to a higher deoxygenation and thus, signal loss. Subsequently, the perfusion is increased to compensate for the increased oxygen demand. The increase in blood flow leads to a lower extraction fraction. This can be explained by faster flow and reduced time the blood stays in the in the capillary bed. So, although absolutely, more oxygen is consumed in the tissue, the venous blood contains less deoxygenated hemoglobin and the T2* weighted signal increases. The overshoot and the post-stimulus undershoot can be explained by system response characteristics [Buxton et al. - 2004].

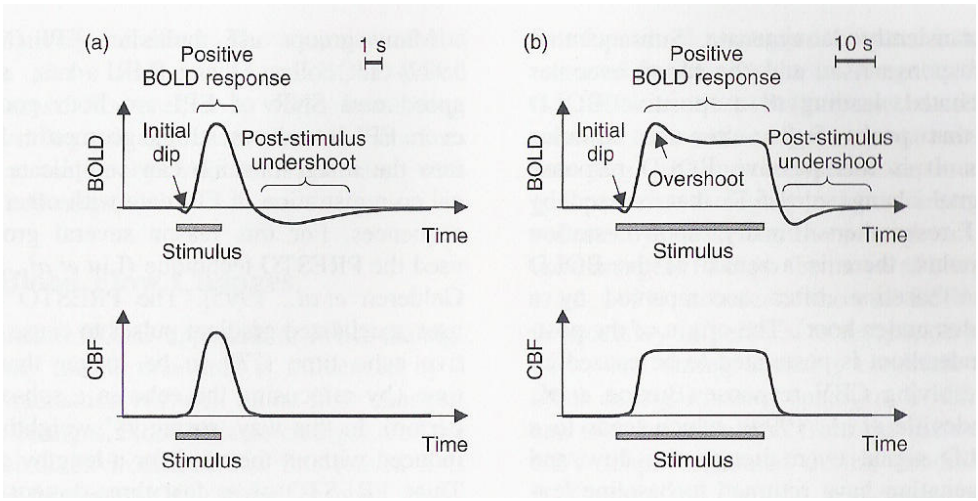

Fig. 27: Schematic BOLD and CBF response curves in one voxel showing brain activation in response to an external stimulus. Image taken from [Tofts - 2003]

2.4.2.2 Quantification of BOLD in the capillary network

The effect of spin dephasing on the signal coming from tissue perfused by a capillary bed containing deoxygenized Hemoglobin has been modeled by Yablonskiy [Yablonskiy, Haacke - 1994]. In this work, a two compartment model is used, to describe the MR signal coming from a medium (tissue) perfused by a vasculature contain-

ing a variable amount of deoxygenated Hemoglobin. The venous capillary bed and venules are modeled as cylindrical objects statistically distributed and directed in space. The oxygenation is described by the blood oxygenation level Y which ranges from 1 for oxygenated blood to about 0.6 for veins. Another important parameter is the hematocrit value Hct which stands for the volumetric fraction of red blood cells in the blood. The Hct depends on many factors like fitness and altitude. A common value is 0.4.

The influence of the oxygenation on the tissue signal in the following is expressed in $\delta\omega$, the frequency shift compared to the Larmor frequency. With the above configuration the obtained formula is

$$R2' = \xi \cdot \delta\omega = \xi \cdot \gamma \cdot \frac{4}{3} \cdot \pi \cdot \Delta\chi_0 \cdot (1 - Y) \cdot B_0 \tag{46}$$

ξ:	Venous compartment size; usually about 0.02
γ:	Gyromagnetic ratio
$\Delta\chi_0 = 0.8 \times 10^{-7}$	Susceptibility difference between totally oxygenated and totally deoxygenated blood with $Hct = 0.4$
Y:	Oxygenation
B_0:	External field strength

In some publications, Hct is included linearly in the above equation, taking $\Delta\chi_0$ independent of Hct.

An important underlying assumption is that water diffusion can be neglected. Dephasing which is due to particle diffusion cannot be recovered in spin echoes and leads to signal loss, called “motional narrowing”. It is generally considered as a contributing part of the T2’ decay, since T2 describes the spin-spin interaction effects. Diffusion has so far been neglected in the Theory section (Ch. 2.1.5). To model T2’ decay, one has to include dephasing due to diffusion and dephasing due to static magnetic field inhomogeneities. Local magnetic inhomogeneities are induced by mesoscopic structures with magnetic field, e.g. venules containing deoxy-haemoglobin. If the effect on T2’ of such static structures is large compared to the effect of diffusion one speaks of the “static dephasing regime”. This is not the case if the typical diffusion time is much smaller than the inverse local Larmor frequency offset $\delta\omega$: the “motional narrowing regime” is characterized by

$$\tau_D << 1/\delta\omega \tag{47}$$

In case of a perfusing vascular system in the imaging voxel, for the above values and $Y = 0.6$, $1/\delta\omega = 9.4\,\text{ms}$ (at 3 T). The characteristic diffusion time for the capillary system, in comparison, is

$$\tau_D \approx \frac{R_0^{\,2}}{4 \cdot D} \approx 2 - 7\,\text{ms} \tag{48}$$

From [Yablonskiy, Haacke - 1994];

$R_0 = 3 - 5\,\mu\text{m}$ Capillary radius

$D \approx 1 \frac{\mu\text{m}^2}{\text{ms}}$ self-diffusion coefficient of water

Therefore, relation (47) cannot be considered satisfied. Diffusion phenomena will additionally contribute to the dephasing. R2' will be under-estimated by Equ. (46). Also, this formula doesn't contain larger venous vessels which will have the main contribution to dephasing.

Functional changes predominantly enter in Equ. (46) by changes of the venous compartment size ξ and the oxygenation level Y. With the other parameters fixed and field strength 3T, Equ. (46) becomes

$$R2' = \xi \cdot (1 - Y) \cdot 270\,[1/s] \tag{49}$$

For $\xi = 0.02$ and $Y = 0.6$, this is $R2' = 2.16 \frac{1}{\text{s}}$, corresponding to $T2' = 460\,\text{ms}$.

Often, the oxygen extraction fraction $OEF = 1 - Y$ is used instead of the oxygenation.

The mean distance between capillaries in Grey matter of the adult human brain is 40 µm. The intermediate tissue space can therefore be filled homogeneously by inflowing water molecules which have reached the tissue by the capillary, and are diffusing through tissue space afterwards, after a certain time. An estimate of this characteristic time can be given with Equ. (48). With $R_0 = 20\,\mu\text{m}$ as half the distance between capillaries, the characteristic time is $\tau_{ch} = 100\,\text{ms}$. This is in on the order of the smallest practically used inflow time resolution of ASL time series experiments. This means that

in any case when we look at the water magnetization of labeled water which has reached tissue space, where the only “transport” mechanism is diffusion, we can consider the water molecules uniformly distributed between the capillaries. Another important conclusion is that, on time scales larger than 100 ms in uniform tissue, the relative vascular volume fraction in the vicinity of the labeled water can be taken as uniform over different inflow times.

The same considerations are basically true for oxygen. In Fig. 28, the oxygen distribution between two capillaries is depicted. In [Purves - 1972], the self diffusion coefficient for oxygen is given as $D_{oxy} \approx 1.6 \frac{\mu m^2}{ms}$. The BOLD effect, however, is induced by the deoxygenated hemoglobin. We are therefore not looking at the oxygen but at the deoxygenated red blood cells which stay in the vasculature.

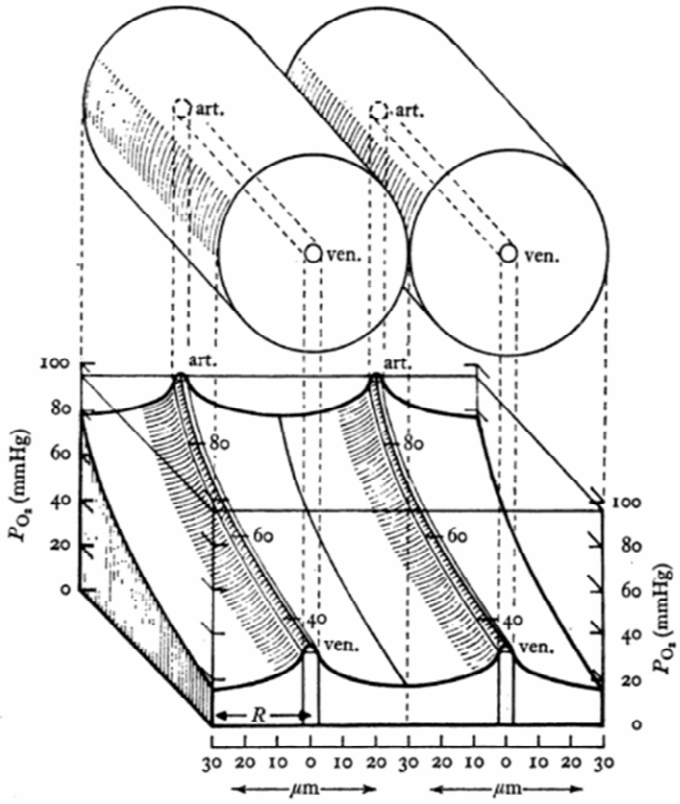

Fig. 28: Model of two adjoining cylinders in a grey matter voxel perfused by two capillaries. At the bottom, the relief of theoretical oxygen concentration is shown in the capillaries and surrounding tissue. From [Purves - 1972]

Since in the tissue voxel the only active transport mechanism for water molecules is blood flow, transport of labeled blood water towards the venous end of the capillary bed will mainly take place in the capillaries themselves. Therefore, as the inflow time increases, more labeled water molecules will be in the environment of the venous side of the capillary bed. In the ASL signal, those molecules will contribute to the BOLD effect.

2.4.2.3 Quantified BOLD measurements

Yablonskiy and Haacke proposed a sequence which is able to sample the rising and declining flanks of a spin echo and called it GESSE ("Gradient Echo Sampling of the Spin Echo", [Yablonskiy, Haacke - 1997]). The sequence acquires one Fourier line multiple times during the formation and decay of the spin echo (Fig. 29).

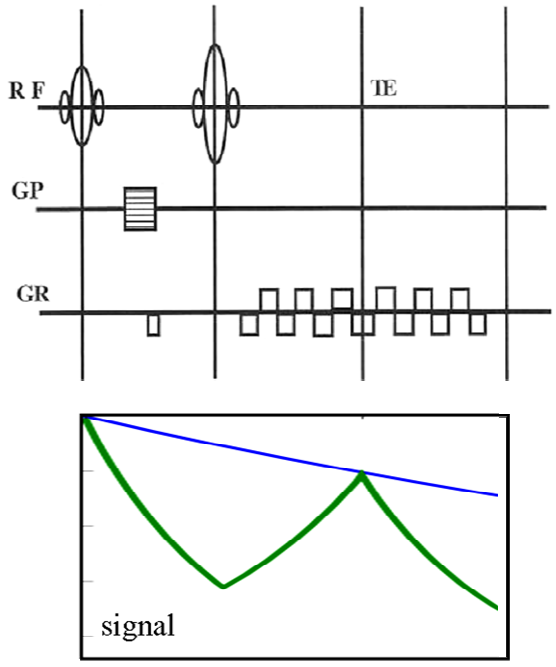

Fig. 29: Schematic pulse diagram of the GESSE sequence ("Gradient Echo Sampling of the Spin Echo"). In the signal intensity is shown in the green curve. A spin echo is formed at TE. The readout gradient encodes the same Fourier line multiple times for different times relative to TE. Image taken from [Yablonskiy, Haacke - 1997]

The signal intensity data points can be used to extract different parameters by least squares optimization. Among the fitting parameters are ξ and Y, which can be fitted separately (a detailed explanation can be found in [An, Lin - 2000]). T2 can be extracted by the asymmetry of the spin echo flanks and used for T2 correction of the data. With this method, ξ, Y, T2 and T2' can be extracted reliably [He, Yablonskiy - 2007]. Resulting maps at 3 Tesla are shown in Fig. 30.

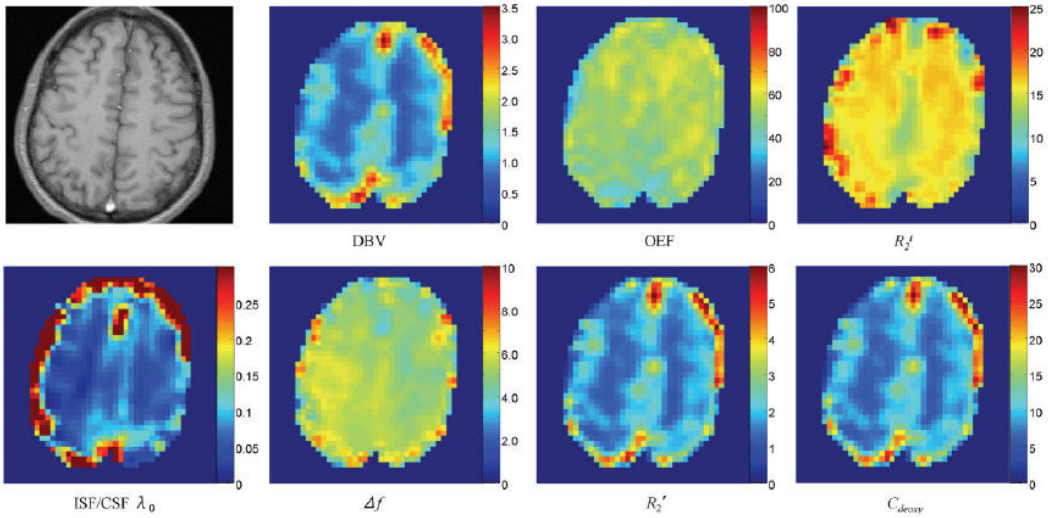

Fig. 30: Representative maps of brain parameters obtained with a low-resolution (64x64) GESSE sequence at 3T. Top left: high-resolution anatomic image. Rest of the maps: DBV fraction (deoxygenated blood volume , corresponds to ξ, in %), OEF (%), *R*2 for brain tissue (1/s), CSF volume fraction, CSF frequency shift (Hz), R2 of brain tissue (1/s), brain deoxyhemoglobin concentration (μM). Image taken from [He, Yablonskiy - 2007]

3 ASL and T2: blood water transfer time and blood brain barrier permeability

Permeability of the blood brain barrier plays a large role in contrast based MR imaging. In several cerebral diseases, the blood brain barrier is affected and permeability is increased. This can be measured with tracer based perfusion techniques, where the macromolecular contrast agent, which usually does not cross the blood brain barrier, will accumulate in the surrounding tissue. Blood and tissue are known to have significantly different T2 values. Therefore, T2 is an excellent marker to answer the question, how fast blood water is exchanged between vasculature and the perfused tissue. The effect of restricted water permeability of the blood brain barrier on the classical ASL signal, which measures the T1 governed signal evolution, has already been described. But it turns out that the effect is so small that it is difficult to measure. Measuring T2 of the ASL signal can thus be an excellent way to measure the blood brain barrier water permeability.

In previous work of other groups, Thomas et al. considered two fixed echo times for modeling the ASL signal dependency of apparent T2 [Thomas et al. - 2001]. A model was presented which describes the temporal evolution of the non-selective and slice-selective images. It did not include permeability effects. Measurements have been done on gerbils.

Wells et al. measured the T2 dependence of the ASL difference signal for various inflow times in rats, with several experimental setups to investigate the signal origin at different inflow times [Wells et al. - 2009]. They found different signal characteristics and explained the findings with several compartments, like vascular, extracellular and intracellular space. A concise formula including permeability has not been given.

In the following, a two-compartment model will be derived based on the General Kinetic Model, including T1 and T2 effects. Afterwards, the details of the MR sequence for the multi-echo acquisition are discussed. Resulting images are shown, yielding maps of blood brain barrier water permeability values.

3.1 Theory: Derivation of a two compartment perfusion model including T1 and T2 decay

A way to model a two compartment model analogous to the General Kinetic Model is to include a transfer term $r_{bl\to ex}(t)$ from blood to extra-vascular space. In the following, two major simplifications will be made: backflow from extra-vascular space to capillaries will not be considered and outflow is neglected, because the typical duration of stay of a water molecule in a voxel is of several seconds and thus longer than the usual measurement times (mean transit time approx. 5 seconds, cf. [Tofts - 2003], [Parkes, Tofts - 2002]). The transfer $r_{bl\to ex}(t)$ will be modeled as an exponential decay, corresponding to a uniform probability for a water molecule in the vasculature to enter the extra-vascular space.

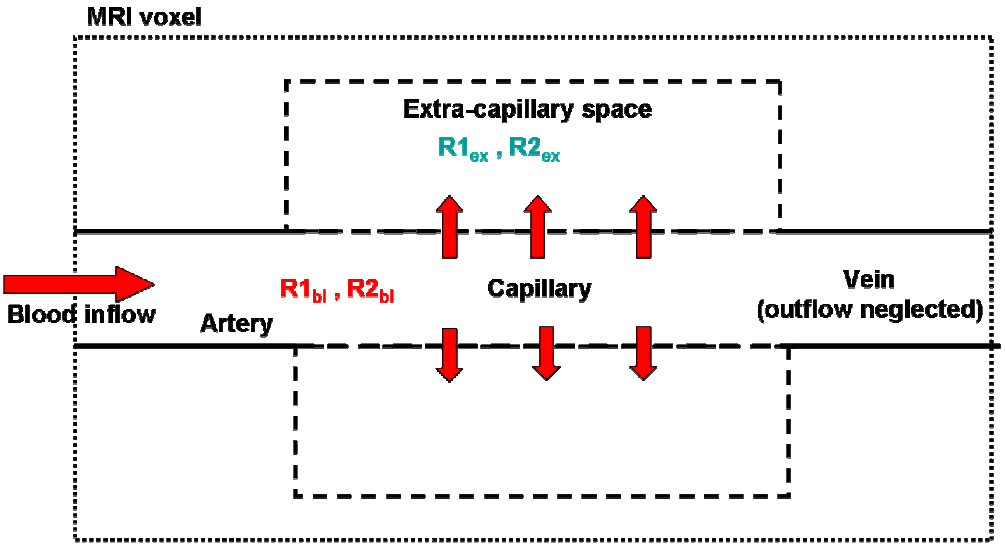

Fig. 31: Schematic diagram of an MR voxel; There are two compartments, a blood (considered purely capillary), and an extra vascular compartment, both with their appropriate relaxation constants. The measured R1 and R2 values will be a mixture from signal of both compartments.

3.1.1 T1 dependent signal evolution

The inflow in the intravascular compartment is then as in Equ. (41), with $r_{bl\to ex}(t)$ as "outflow term", meaning flow from vascular to extra-vascular space:

$$S_{bl}(t) = 2 \cdot M_{a,0} \cdot f \cdot \int_0^t c(\tau) \cdot r_{bl \to ex}(t-\tau) \cdot m_{bl}(t-\tau) d\tau \tag{50}$$

The outflow of the blood compartment determines the inflow of the extra-vascular compartment signal, $1 - r_{bl \to ex}$, convolved again with the delivery function c:

$$S_{ex}(t) = 2 \cdot M_{a,0} \cdot f \cdot \int_0^t c(\tau) \cdot (1 - r_{bl \to ex}(t-\tau)) \cdot m_{ex}(t-\tau) d\tau \tag{51}$$

The overall signal from both compartments is given by

$$S(t) = S_{bl}(t) + S_{ex}(t) \tag{52}$$

Assuming the delivery function as in Equ. (41), single exponential T1 decay and an exponential time constant for blood water transfer $R_{bl \to ex}$, defined for $t \geq 0$:

$$c(t) = \begin{cases} 0 \\ \alpha \cdot e^{-t \cdot R1_{bl}} \\ 0 \end{cases} \quad \text{for} \quad \begin{cases} t < BAT \\ BAT < t < BAT + BL \\ t > BAT + BL \end{cases}$$

$$r_{bl \to ex}(t) = e^{-R_{bl \to ex} \cdot t} \tag{53}$$

$$m(t) = e^{-t \cdot R1_{bl}}$$

Following equations are obtained:

$$S_{bl}(t) = \begin{cases} 0 \\ \dfrac{f \cdot \alpha \cdot M_0}{R_{bl \to ex}} \cdot e^{-(R1_{bl} + R_{bl \to ex}) \cdot t} \cdot \left(e^{R_{bl \to ex} t} - e^{R_{bl \to ex} BAT} \right) \\ \dfrac{f \cdot \alpha \cdot M_0}{R_{bl \to ex}} \cdot e^{-(R1_{bl} + R_{bl \to ex}) \cdot t} \cdot \left(e^{R_{bl \to ex}(\tau_2)} - e^{R_{bl \to ex} BAT} \right) \end{cases} \quad \text{for} \quad \begin{cases} t < BAT \\ BAT \leq t < \tau_2 \\ t \geq \tau_2 \end{cases} \tag{54}$$

$$S_{ex}(t)=\begin{cases} 0 \\ \dfrac{f\cdot\alpha\cdot M_0}{R1_{ex}-R1_{bl}}\cdot e^{-R1_{ex}\cdot t}\cdot\left(e^{(R1_{ex}-R1_{bl})t}-e^{(R1_{ex}-R1_{bl})BAT}\right) \\ \qquad -\dfrac{f\cdot\alpha\cdot M_0}{R_{app}}\cdot e^{-(R1_{ex}+R_{bl\to ex})\cdot t}\cdot\left(e^{R_{app}t}-e^{R_{app}BAT}\right) \\ \dfrac{f\cdot\alpha\cdot M_0}{R1_{ex}-R1_{bl}}\cdot e^{-R1_{ex}\cdot t}\cdot\left(e^{(R1_{ex}-R1_{bl})\tau_2}-e^{(R1_{ex}-R1_{bl})BAT}\right) \\ \qquad -\dfrac{f\cdot\alpha\cdot M_0}{R_{app}}\cdot e^{-(R1_{ex}+R_{bl\to ex})\cdot t}\cdot\left(e^{R_{app}\tau_2}-e^{R_{app}BAT}\right) \end{cases} \quad \text{for} \quad \begin{cases} t<BAT \\ BAT\le t<\tau_2 \\ t\ge\tau_2 \end{cases} \qquad (55)$$

BAT	Bolus arrival time in the voxel
BL	Bolus length
$R_{app}\equiv R1_{ex}-R1_{bl}+R_{bl\to ex}$	
$\tau_2=BAT+BL$	
f	Perfusion
α	Inversion efficiency
M_0	Equilibrium longitudinal blood magnetization

The apparent relaxation term R_{app} includes longitudinal relaxation and exchange, and has been introduced for convenience.

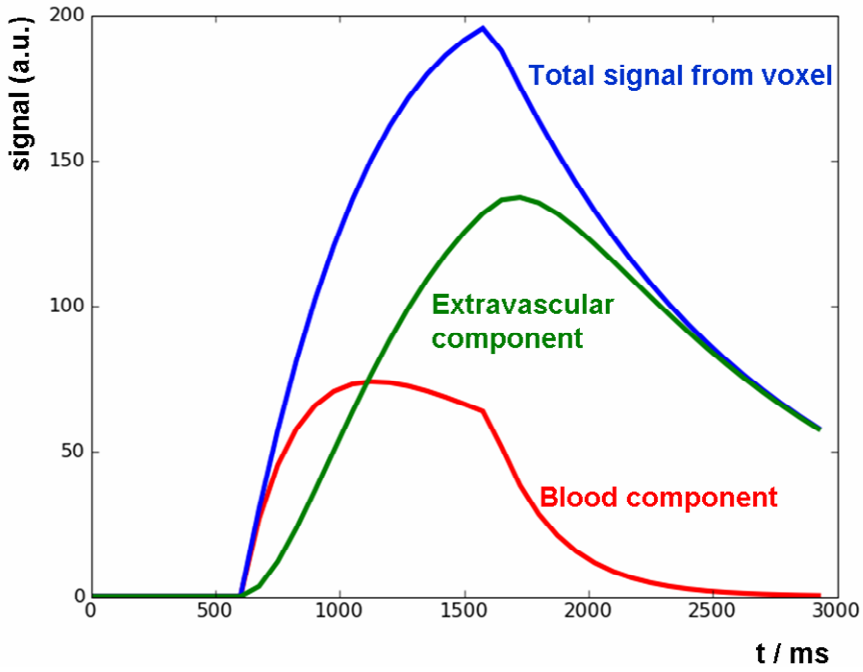

Fig. 32: Theoretical curves showing S_{bl} (red), S_{ex} (green) and S (blue) from Equ. (44) and (45). The plots are calculated with f =175 ml/100g/min, BAT =600 ms, BL =1000 ms, $T1_{bl}$ =1500 ms, $T1_{ex}$ =1100 ms and $T_{bl\to ex}$ =300 ms.

3.1.2 T2 dependent signal evolution

These formulae describe pure T1 decay. As soon as the 90° preparation pulse is applied at time $t = TI$, the longitudinal magnetization is flipped to the transverse plane. This transversal magnetization afterwards decays with T2. This is true for the water molecules in tissue and blood, as well as in the inflowing bolus. For the further calculation of the signal evolution along the TE axis we can write equations like Equ. (53) to calculate the integrals from 0 to TE. The delivery function in this case depends on the time TI. Because there can also be a certain amount of magnetization inside the blood compartment - namely $S_{bl}(TI)$ - which has to be considered in the convolution, this is included using the delta distribution at time $t = 0$. For clarity, we will use te as the temporal variable along the echo time axis and ti for the variable along the inflow time axis. All T2 related functions will be indexed as “2” as distinction from the above T1-related formulae.

$$c2_{TI}(te) = \begin{cases} 0 \\ \alpha \cdot f \cdot M_0 \cdot e^{-TI \cdot R1_{bl}} \cdot e^{-te \cdot R2_{bl}} + \delta(0 - te) \cdot S_{bl}(TI) \\ 0 \end{cases}$$

$$\text{for} \quad \begin{cases} te < \max(BAT - TI, 0) \\ \max(BAT - TI, 0) \le te < BAT + BL - TI \\ te \ge BAT + BL - TI \end{cases} \tag{56}$$

$$r_{bl \to ex}(te) = e^{-R_{bl \to ex} \cdot te}$$

$$m2(te) = e^{-te \cdot R2_{bl}}$$

3.1.2.1 Blood compartment

The result for the blood compartment is

$$\begin{aligned} S2_{bl,TI}(te) &= 2 \cdot \alpha \cdot M_0 \cdot f \cdot \int_0^{te} c2_{TI}(\tau) \cdot r_{bl \to ex}(te - \tau) \cdot m2_{bl}(te - \tau) d\tau \\ &= 2 \cdot \alpha \cdot M_0 \cdot f \cdot \int_0^{te} \{ (e^{-TI \cdot R1_{bl}} \cdot e^{-te \cdot R2_{bl}} + \delta(0 - te) \cdot S_{bl}(TI)) \\ &\qquad \cdot r_{bl \to ex}(te - \tau) \cdot m2_{bl}(te - \tau) d\tau \} \\ &= 2 \cdot \alpha \cdot M_0 \cdot f \cdot e^{-TI \cdot R1_{bl}} \cdot \int_0^{te} e^{-te \cdot R2_{bl}} \cdot r_{bl \to ex}(te - \tau) \cdot m2_{bl}(te - \tau) d\tau \\ &\qquad + 2 \cdot \alpha \cdot M_0 \cdot f \cdot S_{bl}(TI) \cdot r_{bl \to ex}(te) \cdot m2_{bl}(te) \\ &= S2A_{bl,TI}(te) + S2B_{bl,TI}(te) \end{aligned} \tag{57}$$

In the last line, this has been split up into a first part for ongoing inflow also after TI ($S2A$) and a second term with only outflow and decay ($S2B$). The first term is technically the same as in equation (54). Attention has to be put on the different cases of $TI < BAT$ and $TI > BAT$.

If $TI < BAT$, the solution looks similar to Equ. (54) and there are three cases:

$$S2A_{bl,TI}(te)=\begin{cases}0\\ \dfrac{f\cdot\alpha\cdot M_0}{R_{bl\to ex}}\cdot e^{-TI\cdot R1_{bl}}e^{-(R2_{bl}+R_{bl\to ex})\cdot te}\cdot\left(e^{R_{bl\to ex}te}-e^{R_{bl\to ex}(BAT-TI)}\right)\\ \dfrac{f\cdot\alpha\cdot M_0}{R_{bl\to ex}}\cdot e^{-TI\cdot R1_{bl}}e^{-(R1_{bl}+R_{bl\to ex})\cdot te}\cdot\left(e^{R_{bl\to ex}(\tau_2-TI)}-e^{R_{bl\to ex}(BAT-TI)}\right)\end{cases} \tag{58}$$

$$\text{for}\quad\begin{cases}te<BAT-TI\\ BAT-TI\le te<\tau_2-TI\\ te\ge\tau_2 TI\end{cases}$$

If $TI>BAT$ and $TI<BAT+BL$ there are two cases:

$$S2A_{bl,TI}(te)=\begin{cases}\dfrac{f\cdot\alpha\cdot M_0}{R_{bl\to ex}}\cdot e^{-TI\cdot R1_{bl}}e^{-(R2_{bl}+R_{bl\to ex})\cdot te}\cdot\left(e^{R_{bl\to ex}te}-1\right)\\ \dfrac{f\cdot\alpha\cdot M_0}{R_{bl\to ex}}\cdot e^{-TI\cdot R1_{bl}}e^{-(R1_{bl}+R_{bl\to ex})\cdot te}\cdot\left(e^{R_{bl\to ex}(\tau_2-TI)}-1\right)\end{cases} \tag{59}$$

$$\text{for}\quad\begin{cases}0<te<\tau_2-TI\\ t\ge\tau_2 TI\end{cases}$$

For $S2B_{bl,TI}$, we get one expression for all above cases:

$$S2B_{bl,TI}(te)=S_{bl}(TI)\cdot r_{bl\to ex}(te)\cdot m2_{bl}(te) \tag{60}$$

3.1.2.2 Extravascular compartment

The same calculations can be done for the exravascular compartment. It's possible that labeled water has already arrived in the extra vascular compartment which simply decays with $R2_{ex}$. This needs not be considered in the convolution, but just added as an extra term. So, again for $TI<BAT$ we get:

$$S2A_{ex}(te)=\begin{cases}0\\ e^{-TI\cdot R1_{bl}}\left\{\dfrac{f\cdot\alpha\cdot M_0}{R2_{ex}-R2_{bl}}\cdot e^{-R2_{ex}\cdot te}\cdot\left(e^{(R2_{ex}-R2_{bl})te}-e^{(R2_{ex}-R2_{bl})(BAT-TI)}\right)\right.\\ \qquad\left.-\dfrac{f\cdot\alpha\cdot M_0}{R2_{app}}\cdot e^{-(R2_{ex}+R_{bl\to ex})\cdot te}\cdot\left(e^{R2_{app}te}-e^{R2_{app}(BAT-TI)}\right)\right\}\\ e^{-TI\cdot R1_{bl}}\left\{\dfrac{f\cdot\alpha\cdot M_0}{R2_{ex}-R2_{bl}}\cdot e^{-R2_{ex}\cdot te}\cdot\left(e^{(R2_{ex}-R2_{bl})(\tau_2-TI)}-e^{(R2_{ex}-R2_{bl})(BAT-TI)}\right)\right.\\ \qquad\left.-\dfrac{f\cdot\alpha\cdot M_0}{R2_{app}}\cdot e^{-(R2_{ex}+R_{bl\to ex})\cdot te}\cdot\left(e^{R2_{app}(\tau_2-TI)}-e^{R2_{app}(BAT-TI)}\right)\right\}\end{cases} \tag{61}$$

$$\text{for}\quad\begin{cases}te<BAT-TI\\ BAT-TI\le te<\tau_2-TI\\ te\ge\tau_2-TI\end{cases}$$

For $TI>BAT$ and $TI<BAT+BL$:

$$S2A_{ex}(te)=\begin{cases}\alpha\cdot e^{-TI\cdot R1_{bl}}\left\{\dfrac{f\cdot M_0}{R2_{ex}-R2_{bl}}\cdot e^{-R2_{ex}\cdot te}\cdot\left(e^{(R2_{ex}-R2_{bl})te}-1\right)\right.\\ \qquad\left.-\dfrac{f\cdot M_0}{R2_{app}}\cdot e^{-(R2_{ex}+R_{bl\to ex})\cdot te}\cdot\left(e^{R2_{app}te}-1\right)\right\}\\ \alpha\cdot e^{-TI\cdot R1_{bl}}\left\{\dfrac{f\cdot M_0}{R2_{ex}-R2_{bl}}\cdot e^{-R2_{ex}\cdot te}\cdot\left(e^{(R2_{ex}-R2_{bl})(\tau_2-TI)}-1\right)\right.\\ \qquad\left.-\dfrac{f\cdot M_0}{R2_{app}}\cdot e^{-(R2_{ex}+R_{bl\to ex})\cdot te}\cdot\left(e^{R2_{app}(\tau_2-TI)}-1\right)\right\}\end{cases} \tag{62}$$

$$\text{for}\quad\begin{cases}0\le te<\tau_2-TI\\ te\ge\tau_2-TI\end{cases}$$

And for the second term, again in all cases:

$$S2B_{ex,TI}(te)=S_{bl}(TI)\cdot(1-r_{bl\to ex}(te))\cdot m2_{ex}(te)+S_{ex}(TI)\cdot m2_{ex}(te) \tag{63}$$

3.1.2.3 Result

Finally, we can write our result as a two-dimensional function with coordinates ti and te:

$$S_{bl}(ti,te) = S2A_{bl,ti}(te) + S2B_{bl,ti}(te)$$

$$S_{ex}(ti,te) = S2A_{ex,ti}(te) + S2B_{ex,ti}(te) \quad (64)$$

$$S(ti,te) = S_{bl}(ti,te) + S_{ex}(ti,te)$$

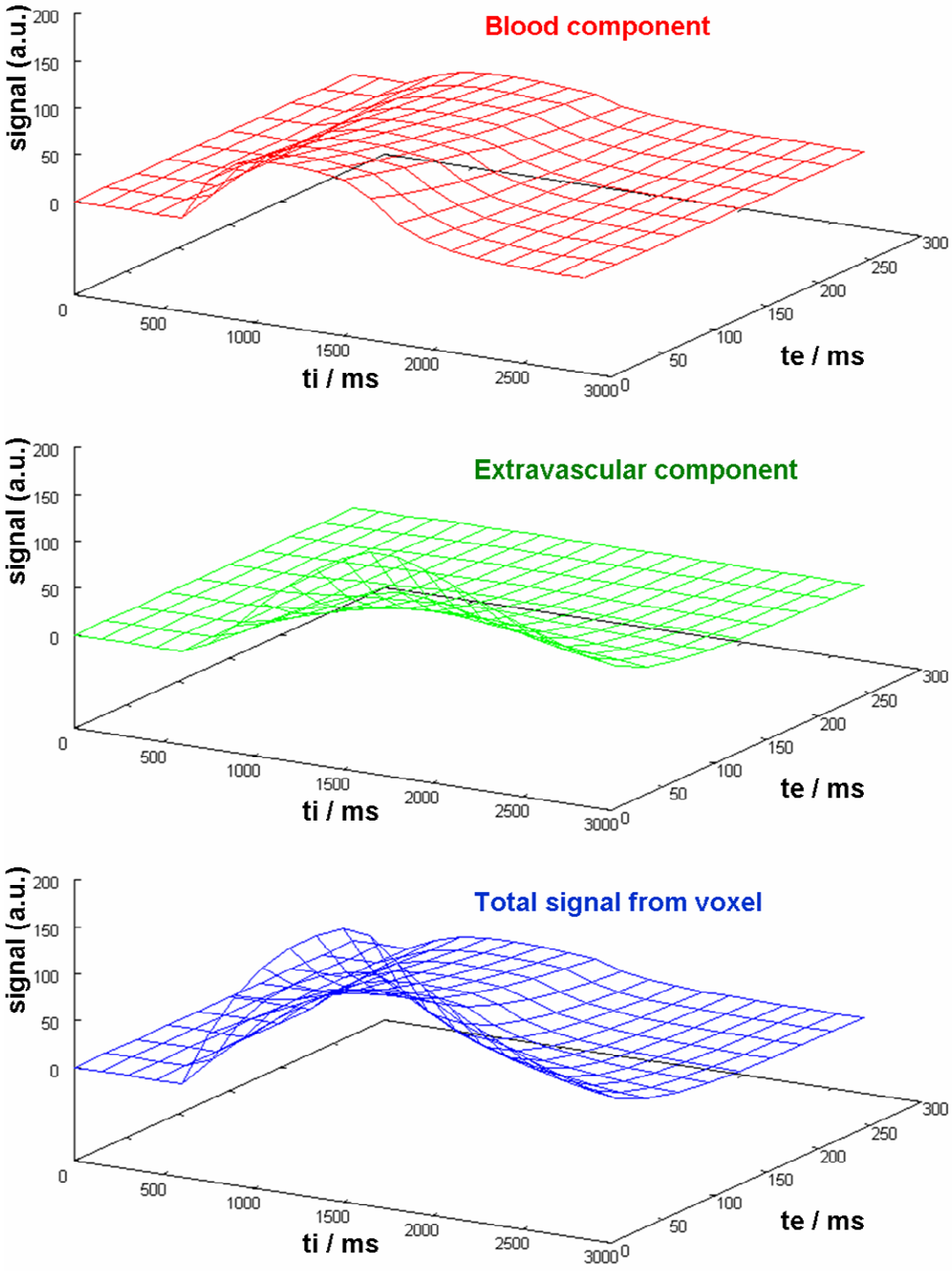

Fig. 33: Two-dimensional plots showing blood component (red), extra-vascular component (green) and total signal (blue) from (64). Signal decay due to T2 along the *te* axis is fast for the extravascular component and slower for the blood component. The plots are calculated with f =175 ml/100g/min, BAT =600 ms, BL =1000 ms, $T1_{bl}$ =1500 ms, $T1_{ex}$ =1100 ms and $T_{bl\rightarrow ex}$ =300 ms.

The formulae have been checked with MAPLE [S - MAPLE] and implemented in C++. They can be accessed by the data processing framework DeVIDE [S - DeVIDE], [Botha, Post - 2008] for 3D plotting with Gnuplot [S - Gnuplot] and fitting with Minuit [S - Minuit], [James, Roos - 1975] based routines. Plots for typical parameters are shown in Fig. 33. The inflow curve along ti at $te = 0$ is similar to Fig. 32. The decay along te is significantly different for the blood and the extravascular compartment. The last plot shows the curve of expected experimental data.

In the above formulae, the exchange term $r_{bl \to ex}$ has been introduced phenomenologically. It describes how long the freshly delivered blood takes on the average to cross the capillary wall and enter the extravascular space. This may depend also on the content of larger vessels in the voxel. If we assume the vasculature in the voxel to be only capillary, we can derive a direct connection to the water permeability of the blood brain barrier. Comparing Equ. (56) with Equ. (44), the residue term described here phenomenologically has been derived in [St Lawrence et al. - 2000] theoretically as

$$r_{bl \to ex}(t) = e^{-(PS/V_c) \cdot t} \tag{65}$$

PS : permeability area surface product
V_c : partial capillary volume in the voxel

This leads to the simple dependency

$$R_{bl \to ex} = PS / V_c \tag{66}$$

V_c is conveniently chosen without units as the percentage value of (capillary) blood in the voxel, which is between 1 and 3%. The permeability surface area product has then the unit of [1/s]. Usually, PS is given in [ml/100g/min] (like perfusion). If we assume equality of Milliliters and Grams, we also have an inverse time unit. Since the uncertainty about the correct V_c is very high, it has been common in recent ASL publications (e.g. [Parkes, Tofts - 2002], [Wang et al. - 2007]) to use the ratio PS / V_c as result.

For an approximate the evaluation and comparison with PET data, we can use

$$PS = 0.02 \cdot R_{bl \to ex} \tag{67}$$

3.2 Methods: Development of the modified 3D-GRASE-readout module for T2 quantification

In order to measure T2 of the inflowing blood, the 3D-GRASE readout scheme has been modified to realize different echo times TE. The sequence is presented here and the major aspects discussed.

3.2.1 Modified 3D-GRASE for T2 measurement

A standard 3D-GRASE sequence samples the center partition with $k_z = 0$ at after the first refocusing pulse (centric reordering, cf. Ch. 2.2.5). With an EPI readout for each partition, this means that the first spin echo, and the center of k-space, is read reached between the first two refocusing pulses. This corresponds to the echo time "$TE\,1$" in Fig. 34, where the center of partition "P 1" is acquired.

For an acquisition with longer TE, the first refocusing pulse of the GRASE readout is applied at a later time $TE/2$. The first spin echo appears at TE, and the first k-space partition can be acquired. The subsequent partitions are encoded and acquired without change (Fig. 34).

As in GRASE, the readout of a single TE is sampled in one shot. On each spin echo between two 180° refocusing pulses, one partition is sampled by an EPI readout. For each TE, the ASL measurement has to be repeated.

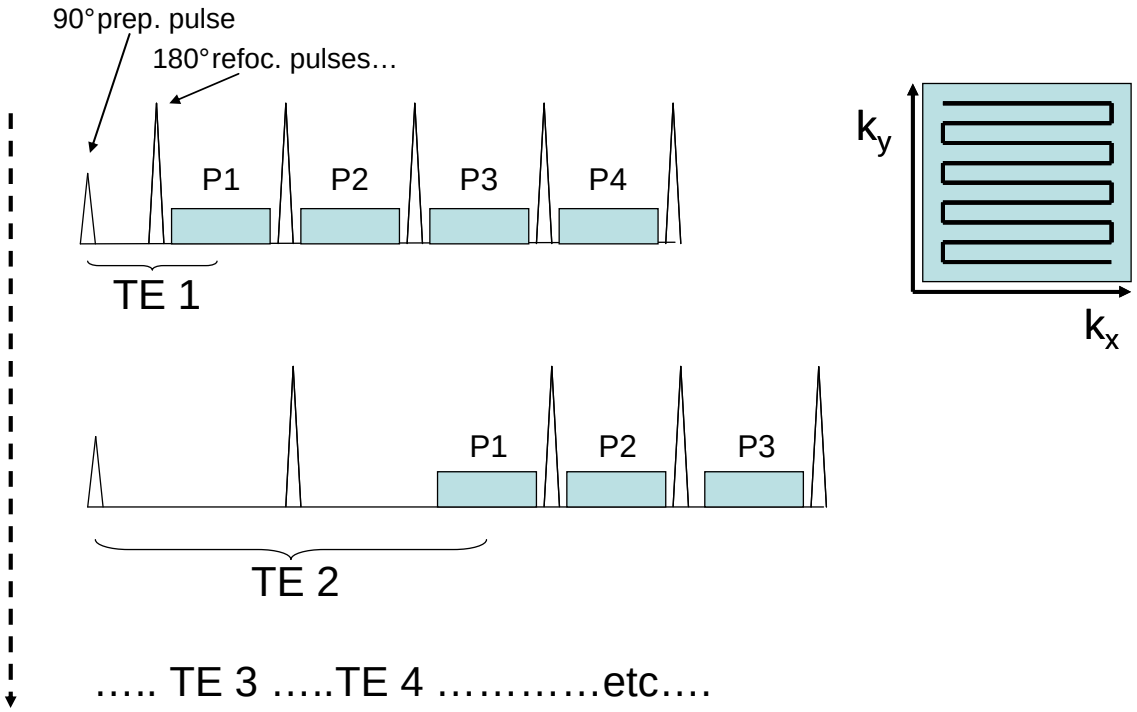

Fig. 34: Readout scheme of the modified 3D-GRASE for T2 measurements; the readout blocks are shifted to later echo times TE after the 90° preparation pulse.

The echo times acquired as seen in Fig. 34 are $TE1$, $3 \cdot TE1$, $5 \cdot TE1$ etc. This timing is important because of the occurrence of stimulated echoes, as will be explained in the following section. As depicted, acquiring later TE corresponds to leaving out certain refocusing pulses and shifting the partitions to later times. This is done in order to keep the same timing as in the original GRASE sequence.

3.2.2 Stimulated echoes

A nominal 180° refocusing pulse in reality is not perfect and does not invert all magnetization. In contrast, there will always be a component of the magnetization which is unaffected by the pulse, and a component which will be flipped back to the transverse plane. At first sight, this means signal loss for the following spin echoes. However, in multi-echo sequences, the part of the magnetization which has not been flipped by 180° can be flipped by the next following refocusing pulse and form a spin echo later. This can be visualized in extended-phase graphs (Fig. 35, cf. [Hennig - 1988]) which plot the magnetization dephasing over time. The dephasing evolves linearly with time. Refocusing pulses can flip the magnetization, inverting the dephasing. Reaching zero, the magnetization is rephased and a spin echo can be observed. Possible pathways are shown in Fig. 35, forming a primary spin echo (blue) and a stimulated echo (green).

Another possible pathway is shown in red until the second rf pulse, for the part of the magnetization which has not been affected by the first refocusing pulse. “rf 1” corresponds to the 90° preparation pulse, while “rf 2” and “rf 3” are refocusing pulses.

On the right, Fig. 35 shows that, with correct echo and rf pulse spacing, the primary spin echo and the stimulated echo will coincide. This mechanism is an important basis of 3D-GRASE (and all other CPMG sequences), which has an echo spacing of [$TE/2$ – TE – TE – TE ….]. In our case, this is the reason that the chosen echo time increase is always 2 times TE . In this configuration, also stimulated echoes from the first refocusing pulse will contribute later to the readout signal. Shifting the readout by multiples of $2 \cdot TE$ can be thought of as just skipping subsequent refocusing pulses and not altering the timing.

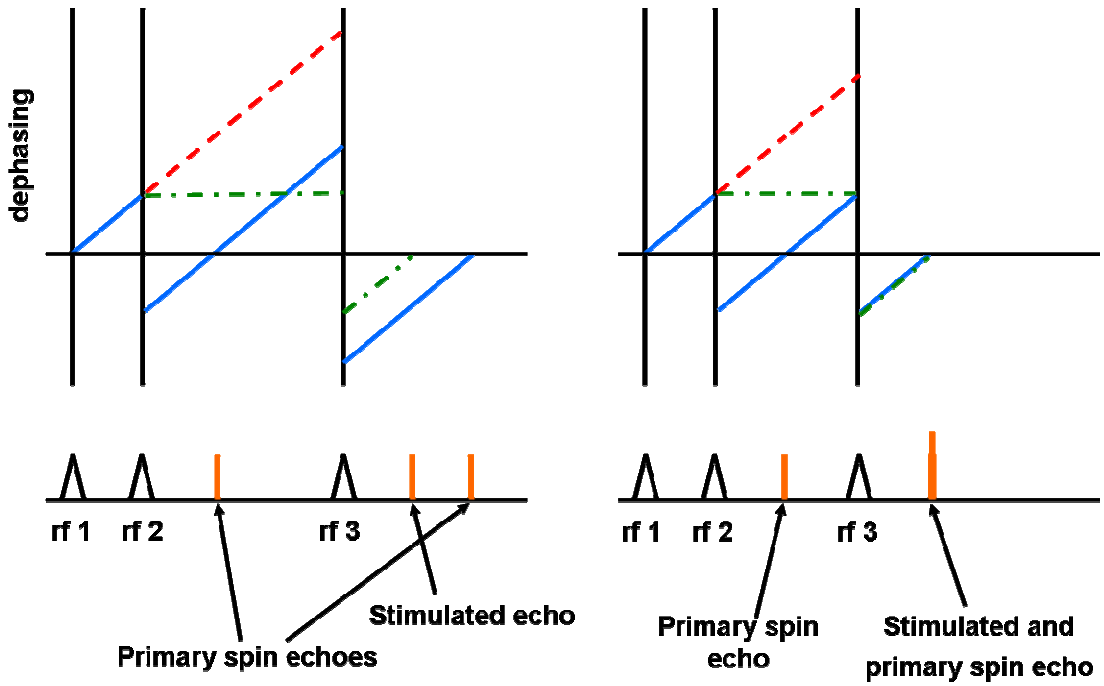

Fig. 35: Primary spin echoes and stimulated echoes: For two different rf pulse timings, extended-phase graphs are shown. In blue, the echo pathways of the primary spin echo are shown. The green and red dashed lines are possible pathways after the second rf pulse, the green later forming a stimulated echo. On the left, the stimulated echo occurs before the primary spin echo after the third rf pulse. On the right, with optimized pulse spacing, the echoes coincide.

When part of the magnetization is flipped to the longitudinal direction, it is subject to T1 decay, without losing its phase information. This is a mechanism how stimulated echoes can contribute to signal at later measurement times. Therefore, it is common to choose lower flip angles in the 3D-GRASE readout, e.g. 120°. In this way, magnetization is "stored" for later echoes. The signal contrast is then a mixture between T1 and T2 weighting. In our case, the first refocusing pulse is always a 180° pulse to ensure that a maximum part of the magnetization is reversed. This is important to measure T2 with minimal T1 contributions on the first echo.

3.3 T2 measurement protocols and trials

All measurements have been carried out on a Trio Siemens MR scanner (field strength 3 Tesla). The acquisition protocol was composed of an ASL sequence and common T1 and T2 weighted anatomical imaging sequences for segmentation and registration. A 32 channel head coil has been used. The ASL sequence had a FAIR preparation scheme, post-labeling saturation of the readout slab, background suppression pulses, Q2TIPS saturation, and a 3D-GRASE readout part as described above. The GRASE readout allowed the single-shot acquisition of 26 partitions of 4 mm and a matrix size of 128x56 with 4 mm resolution inplane (FoV: 51.2 x 22.4 cm^2). It was tuned to acquire 18 inflow time steps ranging from 150 to 3000 ms with a step size of 150 ms, with pulse triggering to suppress physiological noise. The protocol was optimized to allow variable averaging, i.e. averages ranged from two on early time steps to five on late time steps. Three different echo times of 16.5, 49.4 and 82.3 ms have been acquired on separate acquisition. The blood bolus length has been limited to 1000 ms by Q2TIPS. The repetition time was 3800 ms, nominal measurement time 22 min. Pulse triggering increased the actual measurement time to about 25 min.

Five healthy volunteers of age 28 to 40 have been recruited for the preliminary study. The volunteers were asked to lie still. Heads have been cushioned with foam plastics to reduce head motion.

The non-selective and slice-selective datasets have been subtracted offline, allowing non-biased difference images. Motion correction was not feasible because of the change in image contrast over changing TI inflow phases. The difference images have been smoothed with a Gaussian filter along the three spatial axes with a sigma of 1.1 voxels.

No smoothing along the temporal axes TI and TE has been done to preserve temporal detail accuracy. Gray and White matter masks have been extracted from the T1 weighted image with SPM5 [S – SPM5]. The T1 and T2 weighted anatomical data sets have been mapped on the ASL dataset and the gray and white matter masks have been realigned accordingly using SPM5. The two-dimensional model from Equ. (64) has been fitted to the data using a least-squares optimization taken from Minuit [James, Roos - 1975], [S – Minuit]. It was performed for all voxels which lay inside the Grey and White matter masks and exceeded a subject dependent threshold on at least one time point (ti, te) to exclude voxels containing only noise. Limits and starting values have been set on all fitting parameters (Tab. 1) to guide the fit to the global minimum. The main concern lay on the exchange parameter $R_{bl\to ex}$ which therefore had a wide range of allowed values. A fitting routine was chosen which outputs error estimates for each parameter ("Migrad" in [S – Minuit]). The output parameters, corresponding errors and chi-square values were saved as image data maps. All of the processes above have been automated using on basis of the network prototyping framework DeVIDE [Botha, Post - 2008], [S - DeVIDE], and making use of Python [S - Python], VTK [S – VTK] and ITK [S – ITK] toolkits.

Parameter	Starting value	Lower limit	Upper limit
f [ml/100g/min]	290	0.25	5000
BAT [ms]	400	50	1300
BL [ms]	1000	850	1000
$T1_{bl}$ [ms]	1500	fixed	
GM $T1_{ex}$ [ms]	1300	1050	1250
WM $T1_{ex}$ [ms]	900	750	1050
$T2_{bl}$ [ms]	165	fixed	
$T2_{ex}$ [ms]	70	fixed	
$T2_{bl\rightarrow ex}$ [ms]	10	1	3000

Tab. 1: Initial fitting parameters of the T2-ASL data evaluation.

3.4 Perfusion quantification

Compared to dynamic susceptibility contrast measurements, ASL has an important advantage: ASL perfusion data sets can be quantified to yield absolute perfusion values. The resulting value is generally given in ml blood per 100 g tissue per minute. This can be done in ASL time series measurements by fitting a model, e.g. Equ. (42), or, in this case, Equ. (64), to the data on a voxel-by-voxel basis. For the quantification, the correct value of $M_{0,a}$ has to be known, the longitudinal equilibrium blood magnetization. This can be measured with inversion recovery experiments on blood samples. In the present ASL time series experiments, all necessary data is acquired to derive an estimate of $M_{0,a}$. With the assumption that there exists at least one voxel in the image in a large artery which is fully filled with blood, one can take the signal values and the corre-

sponding temporal and spatial information to derive $M_{0,a}$. This will, however, only give a lower estimate because of potential partial volume effects. In the data evaluation, the normalization has been performed automatically. With a fixed value of $T1 = 1500$ ms, the algorithm looked for a voxel with maximum signal, corrected for T1 relaxation in blood ($signal \cdot e^{t/T1}$). The uppermost two and lowest two image slices were excluded to suppress infolding artifacts. Also, time steps of TI<250 and TI>1500 has been excluded: the former, because background suppression isn't applied at the lowest time steps, and the later to suppress noise artifacts (high noise values times $e^{t/T1}$ would lead to over-estimation). This resulted in the maximum blood signal value in one voxel, $m_{0,\max}$. This is the value of the image voxel, corrected for T1. It is proportional to the magnetization, but characteristic for the MR scanner and sequence. It is therefore a dimensionless number and not the physical magnetization.

The physical magnetization $M_{0,a}$ depends on voxel size since it is proportional to the number of water molecules in the voxel. $m_{0,\max}$, instead, is independent of voxel size because the images are automatically scaled by the image reconstruction algorithm on the scanner. For quantification, the value $m_{0,\max}$ has first to be multiplied by the voxel size V_{vox} in mm³.

The derived maximum magnetization value is afterwards transformed to units which will yield the perfusion in [ml/100g/min], thus $M_{0,a} = \frac{m_{0,\max} \cdot V_{vox} / [\mathrm{mm}^3]}{1000 \cdot 100 \cdot 60}$.

Measured $M_{0,a}$ values are listed in Tab. 2. Twelve time series measurements were taken for quantification, including the five datasets for T2 quantification in the current chapter. The average value is 0.0021, standard deviation is 0.00057. There are variations over subjects and measurements which can be explained by partial volume effects leading to underestimation, and pulsation artifacts which can potentially lead to over-estimation.

The inversion ratio α in PASL experiments is close to 100% [Petersen et al. - 2006] and is therefore assumed as $\alpha = 1$. The error of this simplification is very small compared to the 25% variation of $M_{0,a}$.

Protocol **Subject**	**T2-ASL**	**T2'-ASL**	**other**
A	0.00268	0.00305	0.00231
B	0.00210	0.00207	
C	0.00112		0.00129
D	0.00172	0.00217	0.00236
E	0.00122	0.00181	
AVERAGE	0.0021+-0.0006		

Tab. 2: Values for $M_{0,a}$, derived from twelve ASL time series measurements, with five subjects and different measurement protocols. T2-ASL are the measurements of the current, T2'-ASL the data from the following chapter.

3.5 Results: Blood water transfer and blood brain barrier permeability

Fig. 36 shows a dataset acquired with the T2 protocol. The anatomical T1 image has been registered and resampled to the non-selective images for data analysis.

A first model fit has been carried out with values shown in Tab. 1. Arterial blood T1 and T2 values were fixed to mean literature values (cf. Appendix B) because no substantial change is assumed as long as the blood is in the vascular compartment. Also, in case of fast exchange, the blood values cannot be fitted reliably. Starting values for tissue T1 are chosen on basis of the White and Gray matter masks. Because of partial volume effects and the large white matter – gray matter difference in T1 the tissue values have been fitted with appropriate limits. Tissue T2 has been fixed to 70 ms as it doesn't change much between gray and white matter. The lower limit of the exchange constant $T_{bl\rightarrow ex}$ is set to 1 ms which represents fast exchange.

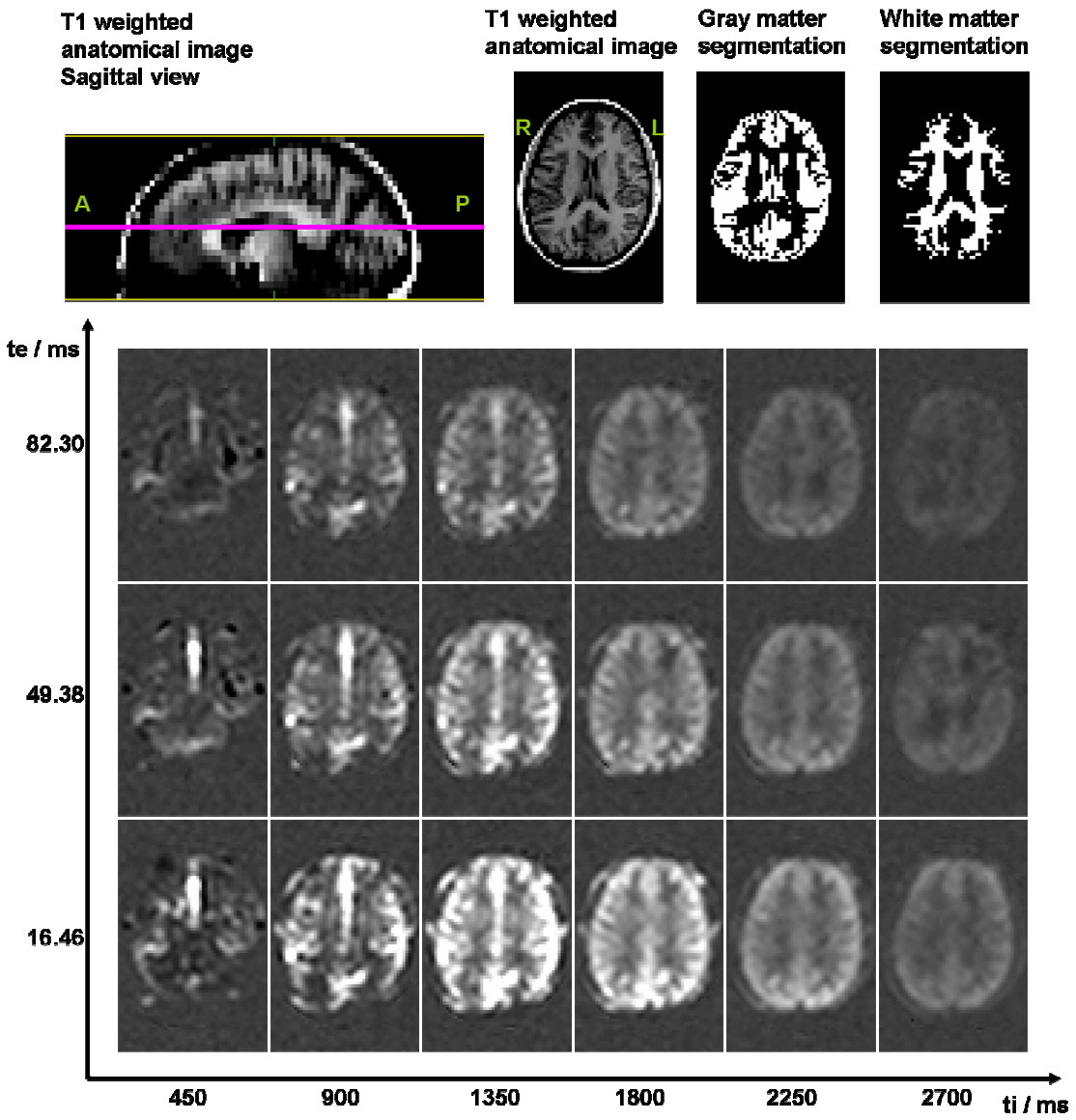

Fig. 36: ASL difference image dataset (some images skipped in ti direction); Along the *ti* axis, the inflow of blood can be seen first in areas around large vessels (e.g. MCA). At later *ti* the signal diffuses and is assumed to come predominantly from tissue. Also, signal decays with T1. Along the *te* axis, T2 decay can be observed. Flow artifacts occur at ti=450 ms (black dots).

Fitting results are visualized for two selected voxel of significantly different $T_{bl\to ex}$. In the first case (Fig. 37) the plot for a voxel with fast exchange is shown. In the second case (Fig. 38) the resulting fit shows a substantial blood component. It is obvious that there is a change in T2 decay over *ti* which is accounted for by fitting $T_{bl\to ex}$ very well. Fitting results and errors are listed in Tab. 3.

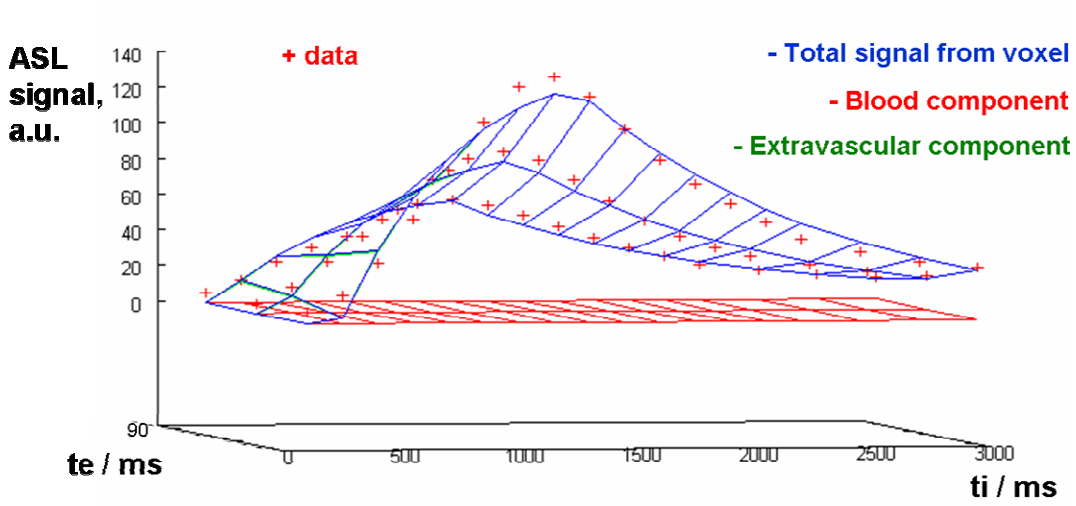

Fig. 37: Data and fit from and fit from a voxel with fast exchange. Blood signal is zero all the time. The total signal curve is built up only from the extra-vascular signal.

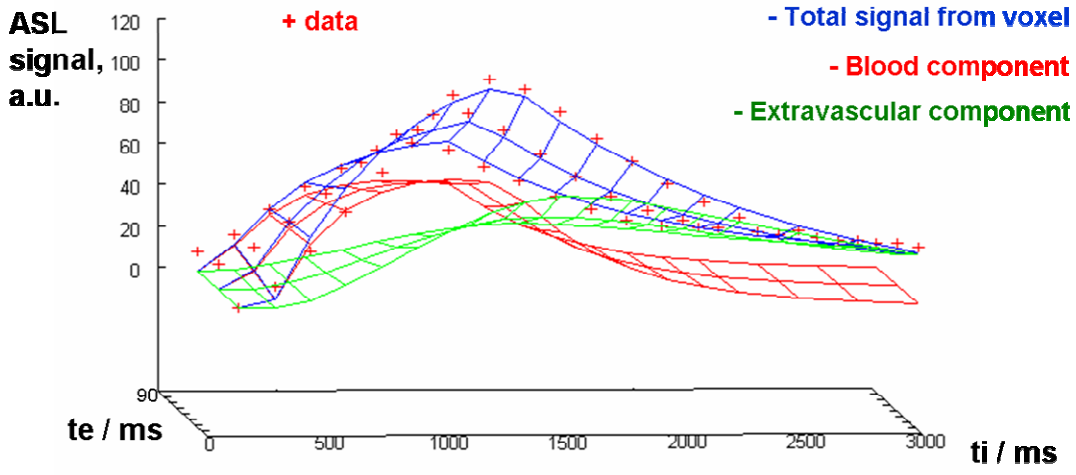

Fig. 38: Data and fit from a voxel with slow exchange. The blood signal rises fast with *ti* until the end of the bolus is reached. The extra-vascular signal rises much slower.

	Fast exchange	**Slow exchange**
Voxel coordinates (x,y,z)	(12,68,7)	(25,55,16)
f [ml/100g/min]	113±2	78±4
BAT [ms]	312±10	299±17
BL [ms]	1000	1000
$T1_{bl}$ [ms]	1500	1500
GM $T1_{ex}$ [ms]	1050±205	1267±84
WM $T1_{ex}$ [ms]		
$T2_{bl}$ [ms]	165	165
$T2_{ex}$ [ms]	70	70
$T2_{bl\rightarrow ex}$ [ms]	1.0 (±450)	623±184

Tab. 3: Typical fitting results for two selected voxel.

In Fig. 39 and Fig. 40, the fitted total signal curves are shown in 2d plots. The main difference between the voxels to note occurs in the first few hundred milliseconds after bolus arrival. In the case of slow exchange (Fig. 40), the experimental data as well as the fitted curves start closely together and spread slowly apart from each other (equivalent to long T2). In the other case (Fig. 39) they spread apart faster in the beginning, showing extra-vascular T2 right from the start. This can be demonstrated more clearly by plotting the relative signal origin (lower plots). Plotted are the percentage ratios of extra-vascular and blood signal over ti from the fitted curves. In the fast exchange case,

the blood compartment can be neglected while in the slow exchange case, blood signal contributes a lot on earlier inflow time steps.

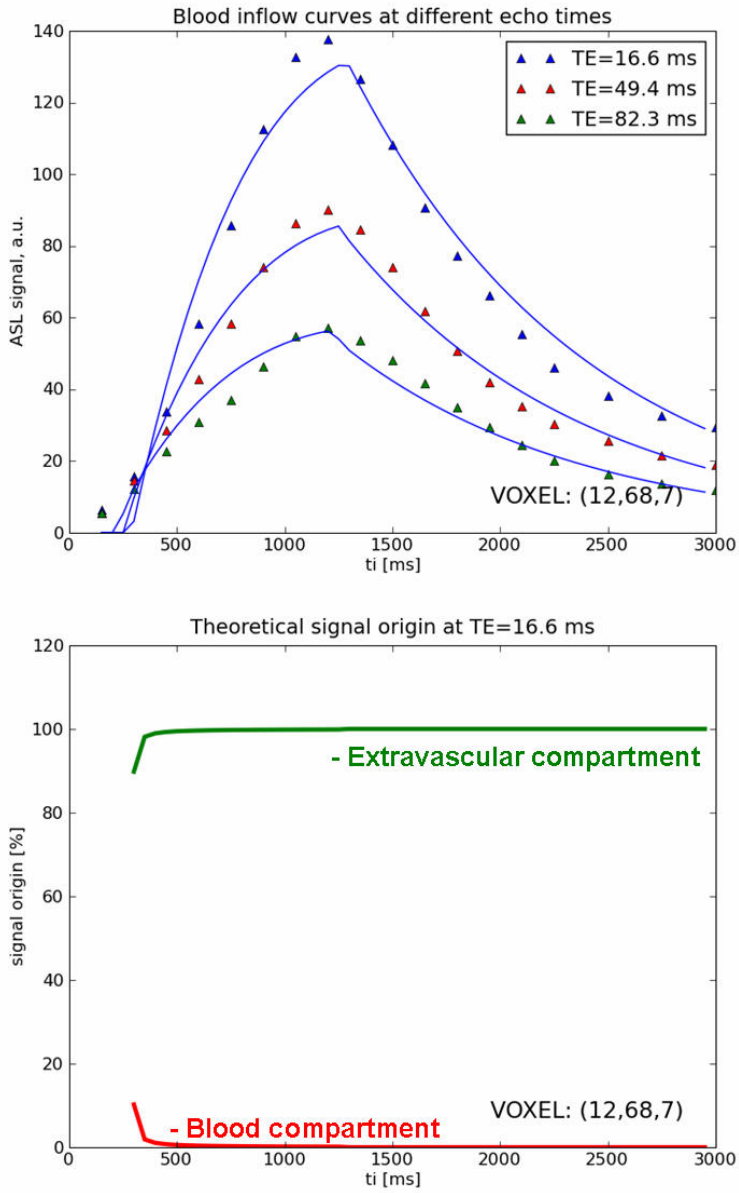

Fig. 39: 2d plots from a voxel with apparent fast exchange showing data and fitted total signal curves (top), for all three echo times. The percentage of signal origin is shown (bottom). All of the signal is coming from the extra-vascular compartment most of the time. A slow exchange voxel is shown in Fig. 40.

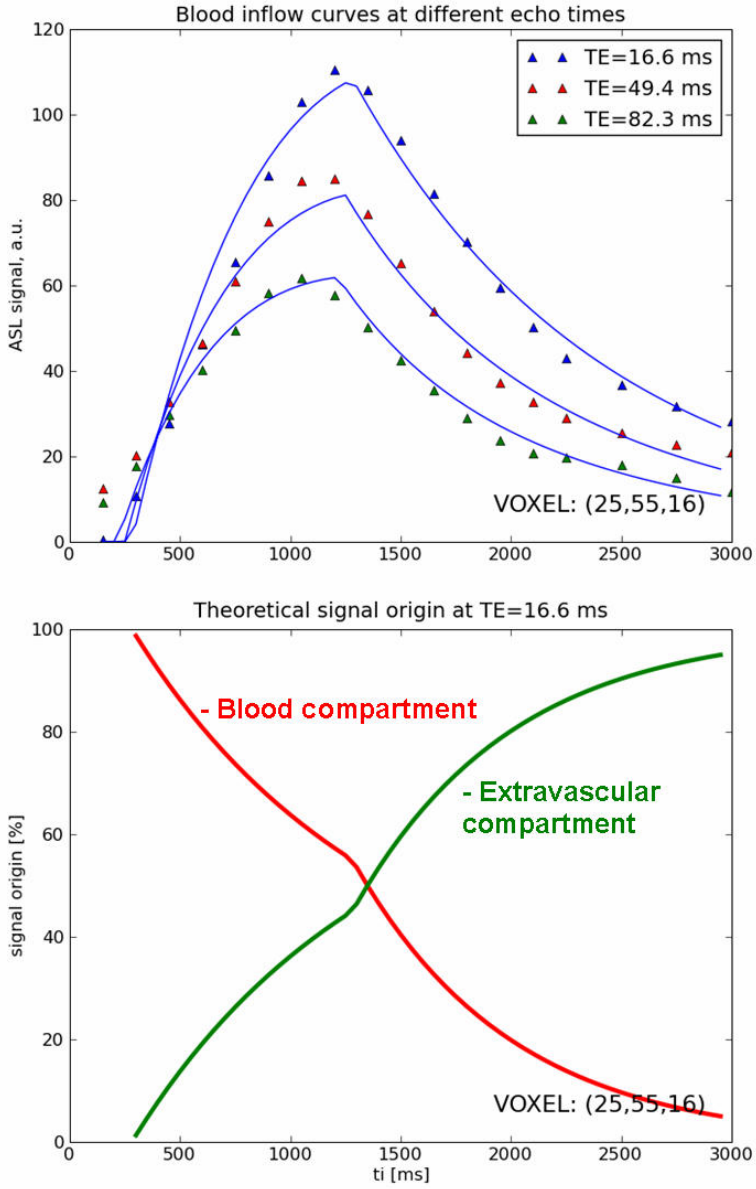

Fig. 40: ASL curves as in Fig. 38, from a voxel showing significant permeability. Signal originates from the blood compartment in the beginning. Blood signal drops with *ti* even faster when $BAT + BL$ is reached and no fresh labeled blood replenishes the blood compartment.

In Fig. 41, the resulting maps are shown for all parameters in two planes. Areas with significantly high $T_{bl\rightarrow ex}$ can be identified as the Supplementary motor area (SMA) and the Parietal and Occipital lobes. Fitting results with $T_{bl\rightarrow ex} = 0$, which would correspond to fast exchange, can be seen in the lower slices in areas with larger arteries, like MCA. This finding is likely to be due to flow artifacts. This pattern can be reproduced in other subjects (Fig. 43).

In Fig. 42, a ROI analysis is done on the resulting $T_{bl\rightarrow ex}$ map and the corresponding fitting error. For lower values we get a 50% error (orange). The error for the higher values (SMA, red) is 25%. This is a result which indicates a good applicability of the fit to the data in this area, leading to a significant difference to fast exchange.

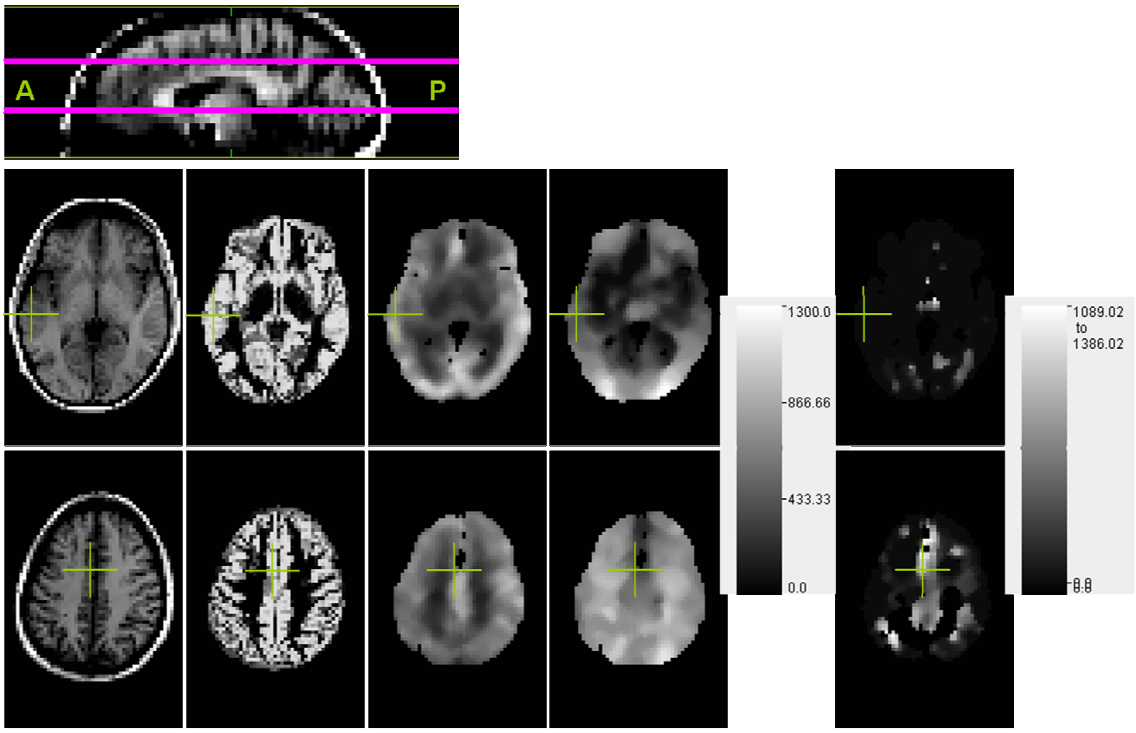

Fig. 41: Derived maps for one

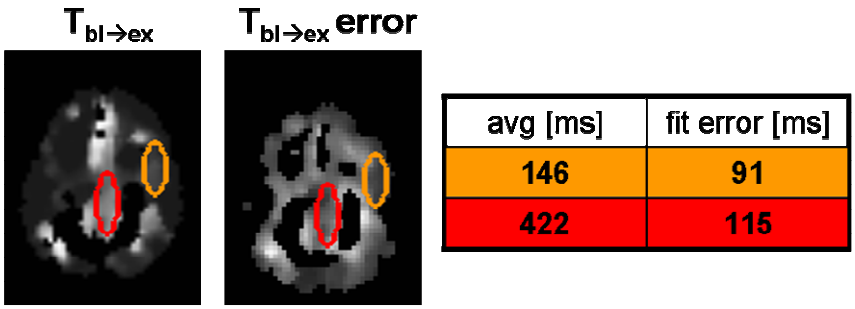

Fig. 42: $T_{bl\rightarrow ex}$ map and corresponding fitting error; typical values are shown in the ROI analysis. The SMA appears bright in the left image (red ROI) indicating high $T_{bl\rightarrow ex}$ values.

$T_{bl\to ex}$ maps of all five subjects are shown in Fig. 43, where the maps are displayed as overlay over the realigned T1 weighted image data sets. A ROI analysis has been done on all subjects like in Fig. 42, choosing a ROI A in the SMA and ROI B in a lateral or occipital cortical region with substantial $T_{bl\to ex}$. Only values $0 > T_{bl\to ex} > 2500$ ms have been included in the analysis to exclude fitting errors. The results are listed in Tab. 4. For comparison with PET data, the values have been transformed to yield PS in units [ml / 100g / min]. ROI A values yielded reasonable data comparable to PET (e.g. [Raichle et al. - 1983]: 144 ml/100g/min). In many cortical regions, however, the model fit yields extremely short $T_{bl\to ex}$. This points to substantial under-estimation of $T_{bl\to ex}$ and leads to unusual high PS values. Possible sources of error will be discussed in the next section.

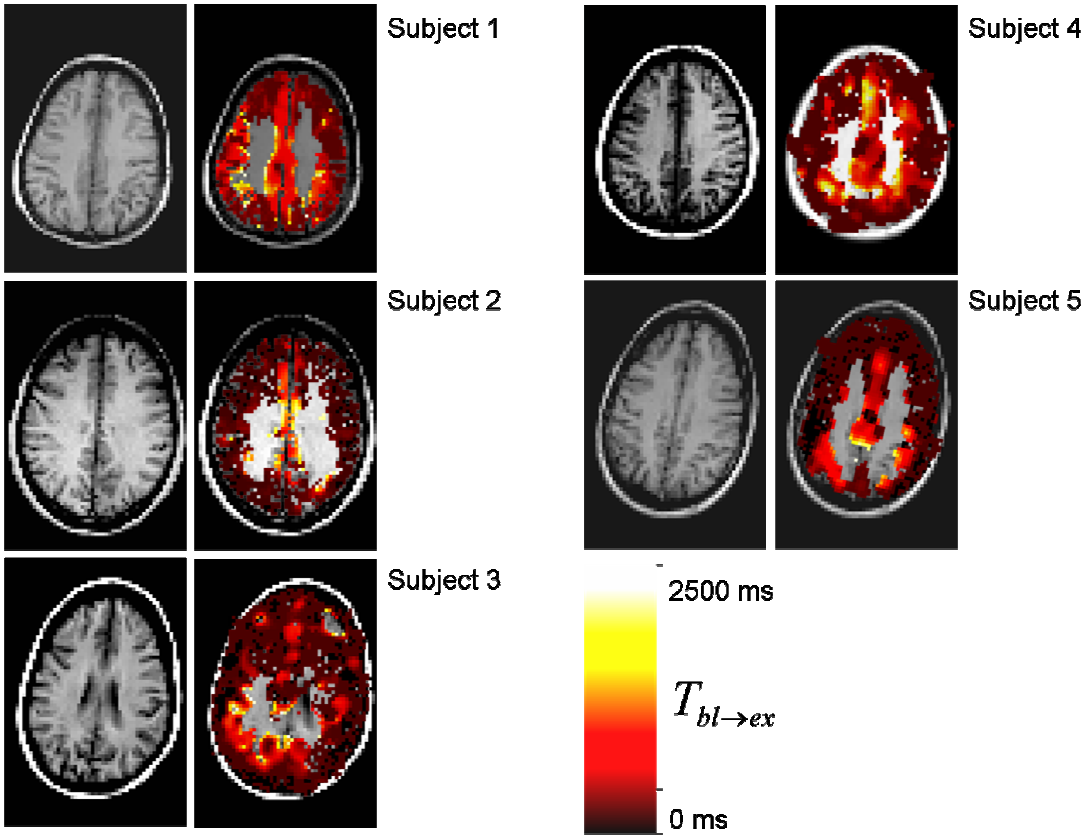

Fig. 43 T1 weighted images, $T_{bl\to ex}$ maps;

$T_{bl\rightarrow ex}$ / [ms]	**ROI A**	**Fitting error**	**PS**	**ROI B**	**Fitting error**	**PS**
S1	725	277	271	638	418	822
S2	615	174	183	72	151	327
S3	442	115	195	146	91	1667
S4	568	534	166	229	116	188
S5	656	214	211	367	352	524
Inter-subject mean	**601**	**263**	**205**	**290**	**226**	**706**
Inter-subject st.dev.	106	162	41	223	149	588

Tab. 4: Table containing ROI values and fitting errors. PS values have also been calculated assuming a venous relative compartment size of 0.02.

3.6 Possible sources of error

The images above show significant patterns of $T_{bl\rightarrow ex}$, which is directly proportional to the inverse permeability. There are especially large values in the Supplementary motor area (SMA), supplied by the ACA, and in the Occipital lobe in the PCA vascular territory. This is an interesting finding, but it has to be made sure that the localized high $T_{bl\rightarrow ex}$ values are not induced by other effects typical for these areas, like bolus dispersion and partial volume effects.

3.6.1 Bolus dispersion

In the theoretical derivation of the T2 dependent perfusion model the possible bolus dispersion has not been considered. As the bolus travels downstream through the vascular tree, the blood bolus will experience dispersion, due to friction at the vessel wall which leads to a non-uniform velocity profile, and non-laminar flow in bifurcations. It is therefore likely that dispersion correlates with the bolus arrival time. Bolus dispersion would lead to a slower inflow of labeled blood in the voxel and to a slower apparent exchange to the extra-vascular compartment. This concept has been presented as "short bolus ASL" by [Günther - 2009a], [Günther - 2009b], where the dispersion of short blood boli has been investigated.

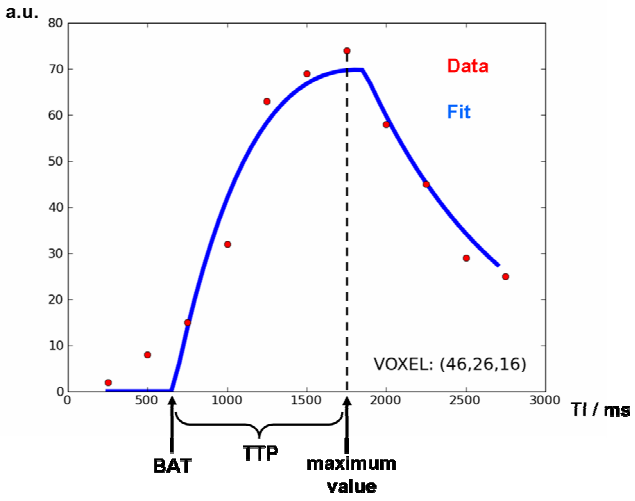

Fig. 44: Time-to-peak (TTP): concept of deriving parameter TTP

To measure dispersion, the "time to peak" has been mapped for each voxel, i.e. the time between the fitted BAT and the maximum signal value. A typical image is shown in Fig. 45. Values typically range from 700 to 1300 ms. Since the bolus length has been fixed to 1000 ms, the higher values point to dispersion. The lower values can be explained by dominant T1 decay, i.e. the voxel is filled with blood very fast and therefore the maximum reached with $TTP < BL$. There are large variations in the SMA. Especially there is a significant pattern of long TTP in the cingulate gyrus above the corpus callosum. These variations cannot explain the higher $T_{bl \rightarrow ex}$ values as the major part of

the SMA shows regular values of TTP around 900 ms. Also, the Occipital lobe shows common values.

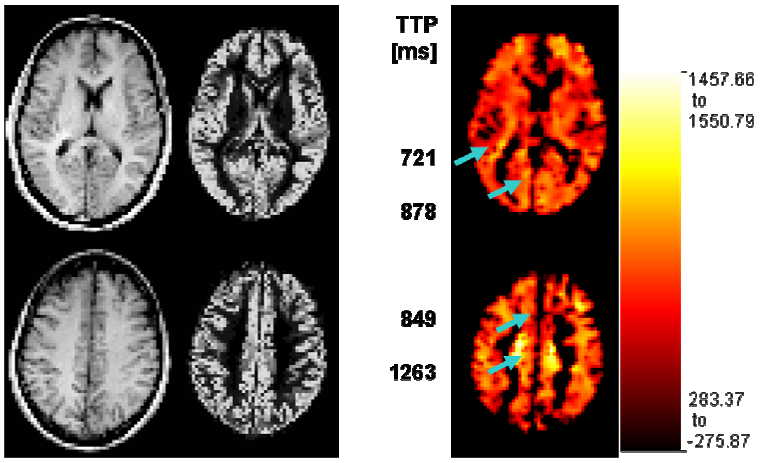

Fig. 45: Left to right: T1 weighted anatomical image, Grey matter segmentation, Time-to-peak maps derived from an ASL time series dataset. Typical values are shown (blue arrows).

3.6.2 Partial volume effects

Partial volume effects play a major role in MRI quantification errors. In this case, a substantially different $T_{bl\rightarrow ex}$ of grey and white matter, or significant differences in T1 or T2, might lead to errors in $T_{bl\rightarrow ex}$ estimation. With a look at the grey matter masks, it is clear that there are regions with different Grey matter density. The probability masks hold grey matter probabilities with values between 0 and 1, which already contain partial volume effects. The data has been smoothed before evaluation, which further increases partial volume effects. Also, in ROI analysis in larger areas, other voxel contribute.

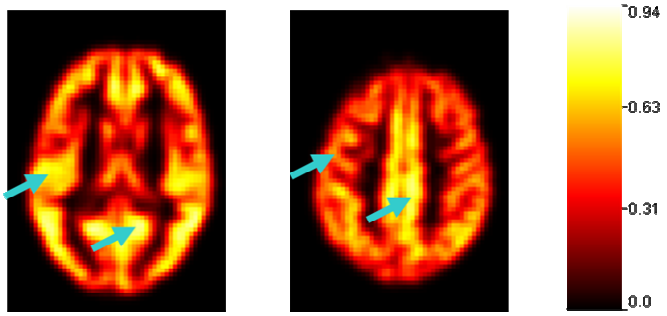

Fig. 46: Grey matter probability map; the GM map has been Gaussian smoothed (sigma 1.1); typical values (blue arrows, left to right): 0.7, 0.8, 0.5, 0.8

To evaluate the grey matter densities in several regions, grey matter masks have been smoothed like the ASL data (Gaussian, sigma=1.1). A mask is shown in Fig. 46. SMA and Occipital lobe show large grey matter density values compared to the lateral grey matter regions. This could explain the high $T_{bl\rightarrow ex}$ values in these areas. It can be assumed that the low SNR values in White matter make it difficult to extract a change in T2 over inflow time.

3.7 Summary

In this work, a method has been developed and presented to acquire and calculate whole brain blood water transfer time constant maps, showing water transfer form vascular to tissue compartment. With the assumption of constant fixed blood compartment size and disregarding larger vessels in the voxels, this is equivalent to whole brain permeability maps. This is the first technique which produces voxel-based whole brain permeability maps of intrinsic blood water based on ASL T2 measurements. The permeability values obtained, measured as permeability surface area product PS, can be compared with data from PET experiments. In PET, the calculation of permeability depends on the extraction fraction of blood water measured on the venous side. Therefore the obtained PS values are not voxel-wise but a summation over the vasculature and capillary bed with certain assumptions. With Equ. (67), the obtained inter-subject mean value of $T_{bl\rightarrow ex} = 601\,\text{ms}$ in the SMA (ROI A) corresponds to permeability area surface product of

$$PS = 0.034\frac{1}{\text{s}} = 205\frac{\text{ml}}{100\text{g}\cdot\text{min}}$$

Values range from 166 to 271 ml/100g/min. The results are in the range of the value reported in [Raichle et al. - 1983], 144 ml/100g/min.

Values could only be obtained for gray matter regions. This supposedly is mainly due to the low SNR in White matter.

With the applied model, there could be identified different regions in the brain with significantly different $T_{bl\rightarrow ex}$. This could be verified on different subjects. The highest values could be obtained in the Supplementary motor area (SMA). Lower values were found in the occipital lobe and lateral cortical grey matter, leading to an inter-subject mean of 705 ml/100g/min. In other regions, especially in the grey matter regions around the left and right MCA, $T_{bl\rightarrow ex}$ values were not significantly larger than zero.

However, as such high variations of the blood brain barrier permeability in grey matter seems unlikely, various sources of errors have to be considered. It is to note first that the value of capillary volume, considered 2%, isn't proven and might change throughout the brain and over different ASL inflow times. Also, larger vessels in the voxel have been neglected. This can have opposing effects on the resulting transfer times: If the vessel mounds into the capillary bed in the same voxel, the transfer time could appear larger due to a delayed delivery of the blood in the tissue. This is a very small effect as it will only delay the blood transfer for a few milliseconds and lead to a higher apparent transfer time. The other possibility is an artery which crosses the voxel ("throughflow"). In the fitting model, this case has not been included. Instead, all possible outflow goes into the extra capillary space, where it decays with a faster R2 decay rate. Especially in the areas of the MCA it seems likely that throughflow of smaller arteries optimized in the fit by assuming faster outflow into the extravascular space. (Throughflow and water transfer has been fitted with an extended model simultaneously. This did not yield stable results since the effects of throughflow and fast exchange are unidirectional and lead to overfitting.)

The conclusion is that in several brain regions or certain voxels the model fit will lead to an underestimation of $T_{bl\rightarrow ex}$ and therefore an overestimation of PS. Reliable values can still be obtained from dense grey matter regions distal to larger vessels, like in the Supplementary motor area and the Occipital lobe. This can be especially verified looking at the fitting errors, which are smallest there.

The transfer of blood water from vascular to extra-vascular space is difficult to measure. A reason for this is the time scale of a few hundred milliseconds which is on the order of the bolus length. Therefore, using the General Kinetic Model, the convolution of input and residue function cannot be neglected. The convolution can only be done analytically with the assumption of some major simplifications. In the approach presented here, a concise analytical description has been found including T2 and T1, regarding two temporal dimensions TI and TE. This made it possible to measure permeability values locally.

As has been mentioned in the beginning, permeability values are important in several cerebral diseases. With this work, a possibility has been presented to obtain permeability maps of the brain non-invasively with a measurement time of 20 minutes. Although the method is at the beginning of its development, it shows prospect to become an important tool in clinical diagnosis in the future.

4 ASL and T2': dynamic blood oxygenation measurements

Quantification of blood flow and oxygenation is an important aspect when investigating cerebral physiological processes. In functional MRI (fMRI) experiments, usually the BOLD susceptibility change is the effect which is investigated and used as contrast. This effect depends on changes in perfusion, venous compartment size and venous oxygenation. These mechanisms make it harder to quantify BOLD or even to look at the physiological underlying effects. In typical experimental setups, mainly signal data from tissue contributes. This signal is influenced by susceptibility changes induced by physiological changes in the vessels.

The combination of a quantified T2' measurement on the ASL signal could lead to further insight in the mechanisms involved. If only the inflowing blood water contributes to the BOLD signal, ASL measurements with variable inflow times have the potential to reveal the different susceptibility effects in the capillary bed and the larger venous vessels, as blood traverses the vascular system. For future applications in fMRI, this holds high potential for increasing contrast to noise by the acquisition of two separate correlating effects, BOLD and perfusion.

4.1 Theory: R2' oxygenation dependence at 3 Tesla

For functional imaging, the relative venous compartment size ξ and oxygen extraction fraction OEF are both subject to change and have to be considered. In the present study, no stimulus has been applied and therefore, no change in brain activation over time is expected. The question is then, given inflow of labeled water particles, how the environment of those particles changes over time as the blood flows into the voxel, and the consequences for ξ and OEF. For a simple model, we can assume a homogeneous tissue distribution over the voxel, perfused by a capillary bed, and no larger vessels involved (Fig. 47).

Assuming a homogeneous tissue distribution over the voxel, the theoretical considerations from Ch. 2.4.2 imply a uniform distribution of labeled water molecules between

capillaries, because of the high diffusion coefficient of water compared to the small inter-capillary distance. In Fig. 48, the distribution of labeled water in the capillaries and tissue is shown schematically, shaded in blue. Because the diffusion time between parallel capillaries is only about 100 ms, the labeled water can be considered uniformly distributed in the tissue space as soon as it has crossed the capillary wall. Only signal from the blue shaded areas contributes in the ASL experiment. Over different inflow times TI, the relative vascular compartment size, which is the ratio of the capillary volume to the total volume of the blue shaded area, can be considered constant in the idealized voxel. Therefore it is convenient for ASL based oxygenation estimations to modify Equ. (49) to depend on the total vascular (assumed capillary) relative compartment size V_c instead of the venous size ξ. V_c can then be assumed to be constant over different inflow times, while the apparent oxygenation Y or oxygen extraction fraction OEF inside the capillary will change over TI. At 3 Tesla, R2' is then

$$R2'(TI) = V_c \cdot OEF(TI) \cdot 270\,[1/\mathrm{s}] \tag{68}$$

Or, as OEF depending on TI:

$$OEF(TI) = \frac{R2'(TI) \cdot [\mathrm{s}]}{V_c \cdot 270} \tag{69}$$

OEF will range from zero at the arterial end and 0.6 at the venous end of the capillary bed (cf. Fig. 47). In ASL time series experiments, one will therefore expect a low value of R2' at short TI. Going to long TI, the assumption is that labeled water molecules are uniformly distributed in the voxel. Therefore, a mean value for OEF over the entire capillary bed can be expected at long TI.

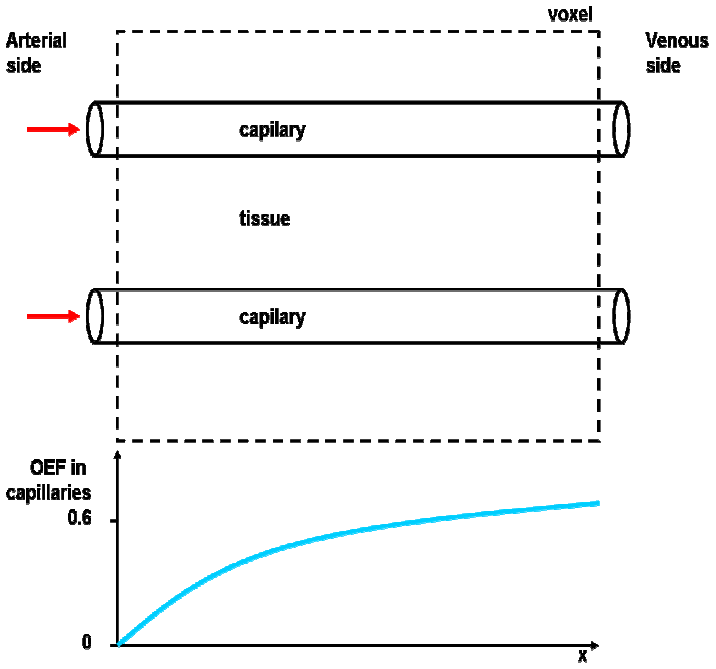

Fig. 47: Schematic voxel depicting the *OEF* model. The tissue voxel is perfused by several capillaries. Inside the capillary, *OEF* rises towards the venous end asymptotically (cf. [Purves - 1972]).

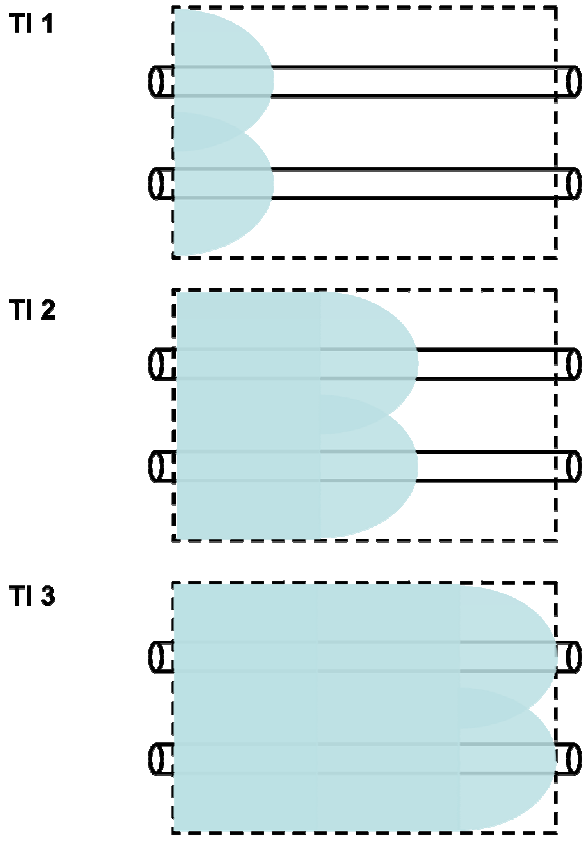

Fig. 48: The perfused voxel with schematic assumed labeled water distribution (blue) over different ASL inflow times *TI* . Because of the small inter-capillary distance, water is expected to be in equilibrium between capillaries after approximately 100 ms (cf. Ch. 2.4.2). Conversely, the capillary bed is traversed along the capillary direction in a time range of several seconds (cf. [Tofts - 2003]). Along the capillary direction, no change in relative vascular compartment size is assumed.

4.2 Methods: Development of a Spin/Gradient dual echo double spiral 3D-GRASE readout module for T2' quantification

T2* maps can be acquired in FID experiments. Images with at least two different echo times need to be acquired to calculate T2*. In 3D-GRASE, a train of spin echoes is prepared and one Fourier partition is acquired on each spin echo. By acquiring the same partition two or more times between two refocusing pulses, the formation of the spin echo can be sampled.

The spiral-out readout concept is predestined for this application because it starts in the k-space center. It is therefore possible to sample a spin echo with two subsequent spiral

readouts, with contrasts on the rising slope and on the spin echo center. Another valuable advantage is the fact that there are no distortions in spiral images. This is especially important when T2* is in the focus of interest. Instead, susceptibility changes lead to blurring artifacts which reduces the effective image resolution. A third advantage is the short readout time due to the efficient k-space sampling.

A schematic pulse diagram and corresponding theoretical signal evolution is shown in Fig. 49. The first two partitions are shown of a 3D-GRASE like partition encoding scheme. Between each refocusing pulse there are now two spiral readouts, instead of one EPI readout. Images are acquired at TE and at $TE - \delta TE$. Echo 1 is the gradient echo and echo 2 the spin echo.

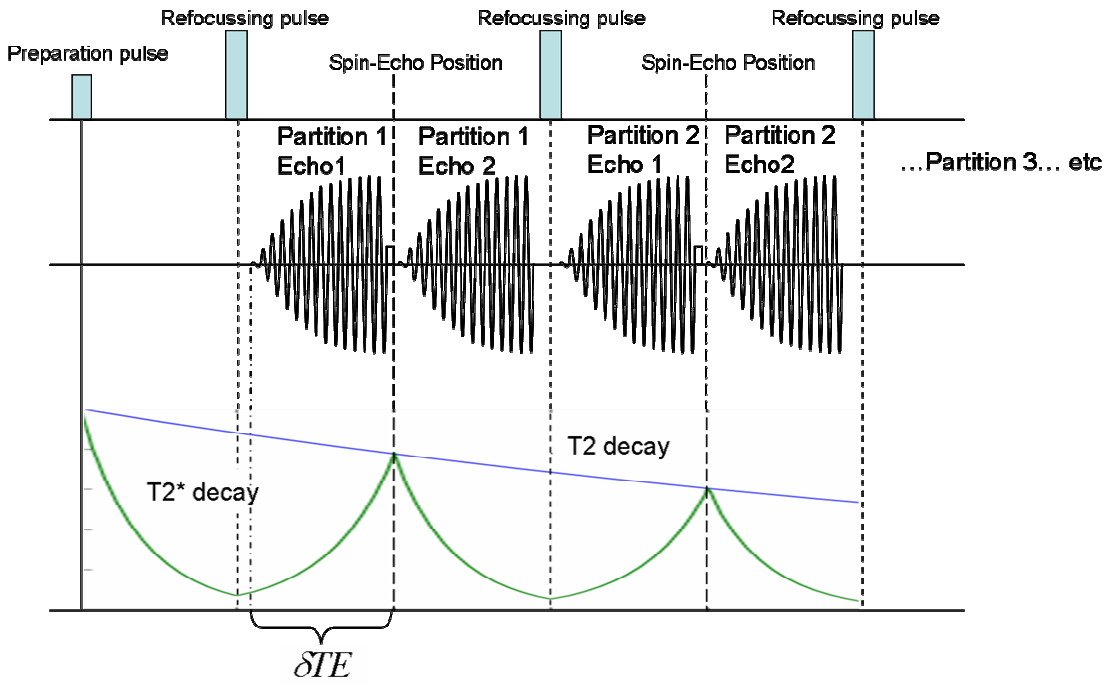

Fig. 49: Schematic pulse diagram and contrast mechanism of the spin/gradient dual echo double spiral 3D-GRASE readout. Spiral readouts start at $t = TE$ on the spin echo center and at $TE - \delta TE$ on the rising slope.

The signal equation for the spin echo with initial magnetization m is

$$s_{SE} = m \cdot e^{-R2 \cdot TE} \tag{70}$$

The signal at the gradient echo is

$$s_{GE} = m \cdot e^{-R2 \cdot (TE - \delta TE)} \cdot e^{-R2' \cdot \delta TE} = m \cdot e^{-R2 \cdot TE} \cdot e^{-(R2' - R2) \cdot \delta TE} \tag{71}$$

Taking the ratio of Equ. (70) and (71) eliminates TE. Afterwards, $R2'-R2$ can be extracted:

$$R2^{+} \equiv R2'-R2 = -\frac{1}{\delta TE} \cdot \ln \frac{s_{GE}}{s_{SE}} \tag{72}$$

This contrast which can be extracted from the developed sequence depends on $R2$ and $R2'$ and is the exponential growth rate of the rising slope. $R2$ and $R2'$ cannot be extracted separately if both are unknown. However, as both depend on compartment (tissue type, blood) and on oxygenation (BOLD) an overall change over separate inflow times of an ASL experiment can be expected. It is to note that $R2^{+}$ can take positive and negative values. It is positive when $R2' > R2$, i.e. when decay due to susceptibility inhomogeneities dominate, and the spin echo signal at TE is larger than the gradient echo signal: $s_{SE} > s_{GE}$. In the case where T2 decay dominates, the spin echo signal will be lower. Then, $s_{SE} < s_{GE}$, and R^{+} takes negative values. The proposed technique is therefore a sensitive tool to determine the dominant decay mechanism.

4.3 T2 star measurement protocol and trials

All measurements have been carried out on a Trio Siemens MR scanner (field strength 3 Tesla). The acquisition protocol was composed of an ASL sequence and common T1 and T2 weighted anatomical imaging sequences. A 32 channel head coil has been used. The ASL sequence in use had a FAIR preparation scheme, post-labeling saturation of the readout slab, background suppression pulses, Q2TIPS saturation, and a GRASE readout part. The blood bolus length has been limited to a maximum 1200 ms by applying Q2TIPS.

For the acquisition of ASL time series, the repetition time was 3300 ms, measurement time 22 min. The double spiral readout has been run with six segments and three averages. The use of a segmented spiral readout reduced the spin echo train length, allowing a short TE of 16.26 ms. The gradient echo was acquired δTE = 5.35 ms before the spin

echo. The 3D-GRASE-like partition encoding yielded 20 slices in single shot. Eleven time steps from 250 ms to 2750 ms have been measured with a step size of 250 ms. The resolution was 3.4 mm inplane with 4 mm slice thickness. The spiral gradient has been limited to a maximum of 0.019 T/m and a slewrate of 115 T/m/s to avoid Nyquist artifacts.

Four healthy volunteers of age 22 to 40 have been recruited. The volunteers were asked to lie still. Heads have been cushioned with foam plastics to reduce head motion.

4.4 Data processing and evaluation

For the investigation of OEF changes with varying inflow time, the ASL difference images have to be calibrated by the tissue OEF. This can be extracted from the non-selective and slice-selective ASL images. Further, a temporal preprocessing is necessary to exclude errors from variable BAT. The necessary steps for OEF calibration and temporal preprocessing are explained in this chapter.

The data evaluation has been automated basing on the rapid prototyping image processing framework DeVIDE [Botha, Post - 2008], [S – DeVIDE], making use of Python [S – Python], vtk [S – VTK] and itk [S - ITK] toolkits.

4.4.1 R2' contrast and OEF calibration

From the gradient and spin echo slice-selective and non-selective images, a contrast can be derived as suggested in Equ. (72), named here $R2^+$. A typical image can be seen in Fig. 50. This is an average of the non-selective and slice selective images, where the influence of perfusion should be minimal and the signal can be assumed to originate mostly from stationary tissue. The high $R2^+$ values in the frontal sinus region show the expected behavior with dominant $T2'$ decay.

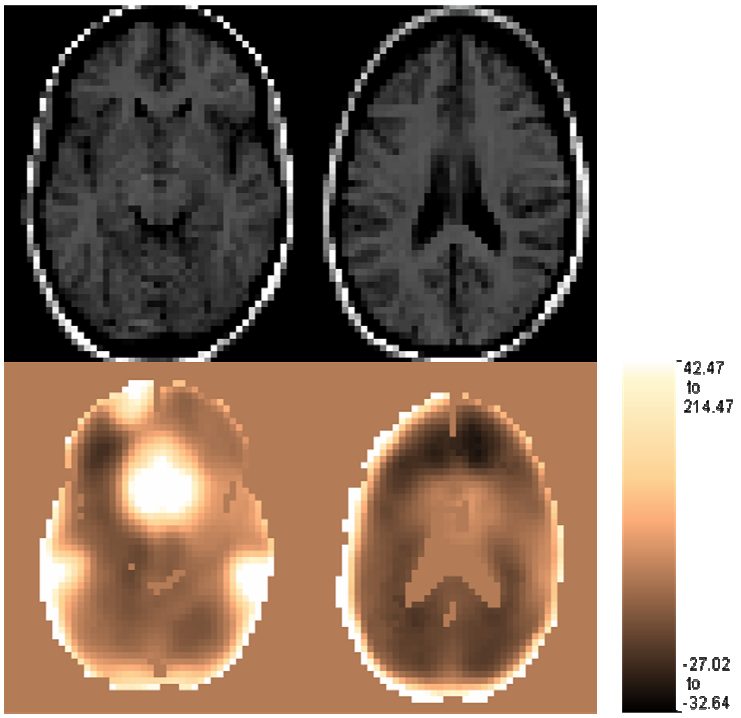

Fig. 50: Anatomic (upper) and $R2^+$ (lower) images. The scaling is in 1/s. Bright regions indicate high field inhomogeneities and dominant $R2'$.

The obtained $R2^+$ values of the non-selective and slice selective images contain information about field inhomogeneities, originating from susceptibility differences or external field inhomogeneities. As such, they can be used to correct the difference images, which are subject to the same macroscopic field inhomogeneities, but have much lower SNR.

If the variables R2 and ξ are known, OEF can be estimated using Equ. (69). This is not trivial, since R2 and ξ depend on brain tissue and region, and literature values vary over a wide range. Additionally, inhomogeneities of the external field are not considered in the above equations, but have a large influence on the resulting R2'.

For a first estimate of the OEF values, literature values can be used, assumed to be constant over the whole brain: $T2 = 20$ ms, and $\xi = 0.03$. The $R2^+$ map from Fig. 50 has been smoothed (Gaussian kernel, sigma = [1.0,1.0,1.0]). The derived apparent OEF map is shown in Fig. 51. The side differences between ROI A and C point to a large effect of external field inhomogeneities on the apparent OEF. This leads to nonsensical results of apparent OEF, with negative values or values greater than one. This error has

to be considered in the further evaluation. A typical literature value of OEF is 0.6, meaning that 60% of the erythrocytes are deoxygenated in the venous vessels. The apparent OEF values obtained in Fig. 51 are therefore in the expected range.

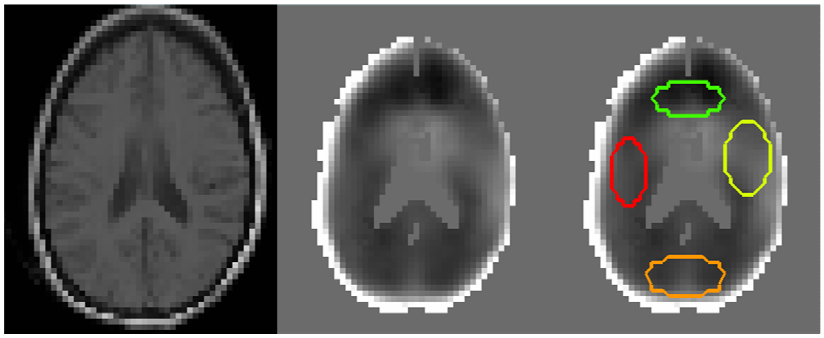

ROI	OEF [%]	std.dev
A	0.61	0.53
B	0.94	0.61
C	1.29	0.31
D	-0.09	0.66

Fig. 51: Apparent OEF map with fixed parameters $R2$ and ξ. The value in ROI A is reasonable. Large differences between the ROIs point to external field inhomogeneities, especially in the frontal area.

For the investigation of OEF changes depending on inflow time, the perfusion weighted difference images need to be calibrated with the apparent tissue OEF. With the assumption that, at high TI, the ASL difference signal originates mainly from tissue space, the same $R2'$ can be expected for the ASL non-selective and slice-selective images. Therefore, the apparent OEF values from the non-selective and slice selective images will be used to normalize the OEF values of the perfusion signal, to yield relative OEF values. With the theoretical assumptions from above, the relative OEF from the ASL difference images will range from zero at $TI = 0$ to one at long TI.

For OEF calibration, the slice-selective and non-selective average of the latest time step with TI =2750 ms has been used. Due to the T1 relaxation, the inflow of fresh labeled blood will be minimal and effects of the ASL preparation can be considered negligible. As above, the apparent OEF has been derived for the last time step average with fixed $R2$ and ξ values. Assuming that, at late time steps, the labeled spins fill all

the tissue and vascular space homogeneously, the same apparent OEF is expected for the corresponding difference image, although with lower SNR. The macroscopic field inhomogeneity effects contribute equally in both images. Therefore, the relative OEF values of the difference image are scaled voxel-wise by division through the corresponding apparent OEF image value of the non-selective and slice-selective mean.

4.4.2 Temporal preprocessing

For a phenomenological look at the signal development over different TI, it is important to get some knowledge about the inflow dynamics first, to eliminate errors from BAT variations. At time steps with $TI < BAT$, blood has not arrived in the voxel yet, and the signal will only contain noise. To look at the change in R^+ over TI, those time steps have to be excluded. As we have already seen in the last chapter, BAT differs from region to region in a wide range over approximately 1000 ms. A first step is therefore to extract a BAT map. This is done with a one-dimensional fit over the data along TI of the first echo. A typical perfusion fit has been shown in Fig. 23. From the fit over all voxels, a BAT map can be extracted. Perfusion and BAT maps of one subject are shown in Fig. 52. After a Gaussian smoothing (sigma=[1.0,1.0,1.0] voxel) the map is used to exclude time steps smaller than BAT. The inflow curve is reparameterized to a temporal time scale $t' = t - BAT$, where BAT has been rounded up to the next greater TI.

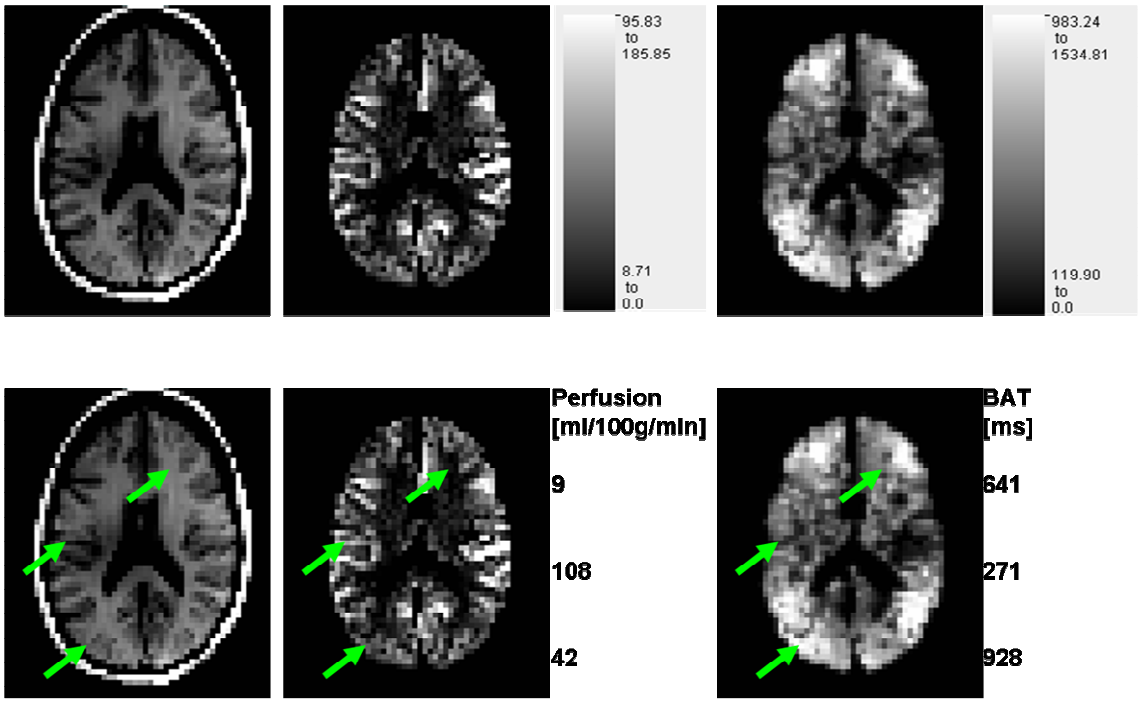

Fig. 52: T1 weighted image, perfusion and BAT maps. There is a strong dependence of perfusion on tissue type (white / gray matter). BAT values differ from 100 to 1500 ms. The lower images indicate typical perfusion and BAT values. The BAT map has been smoothed with a Gaussian filter, sigma = 0.6.

4.5 Results: Dynamic blood oxygenation measurements

In Fig. 53, gradient and spin echo images are shown in direct comparison. Signal loss due to susceptibility inhomogeneities around the frontal sinus can clearly be seen in the gradient echo image. In the spin echo image, the signal has recovered. Due to the short readout echo train length of 200 ms, susceptibility artifacts are minimal.

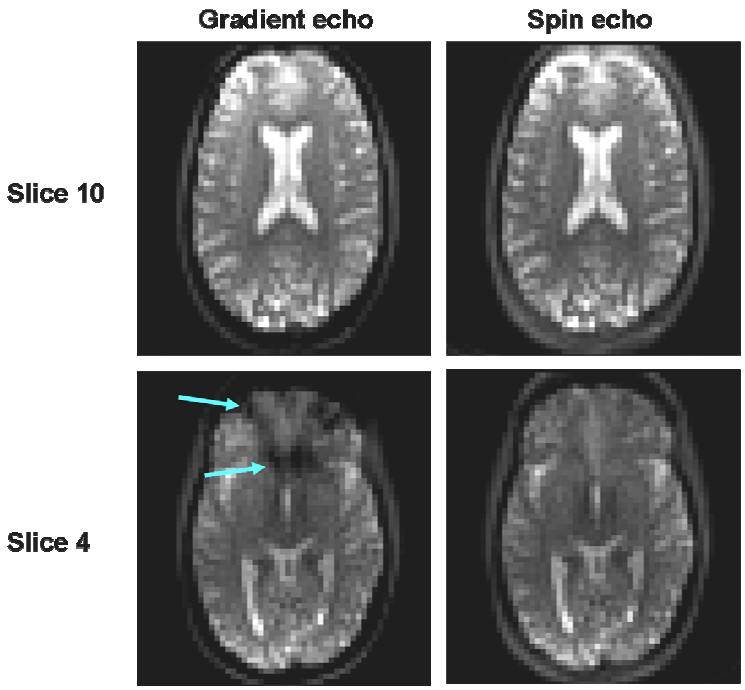

Fig. 53: Gradient and spin echo images from the spin/gradient dual echo double spiral 3D-GRASE (ns+ss average, TI=2000ms). Signal loss due to susceptibility inhomogeneities can be seen at the frontal sinus (blue arrows).

Fig. 54 shows a time series of corrected $R2^+$ of the difference images. The windowing is chosen such that negative values appear blue (corresponding to dominating R2 decay) and positive values appear yellow (corresponding to dominating R2' decay). The $R2^+$ values are stable over the time axis and show only slight changes. In the lower slices, R2' is the dominant process, which is due to the influence of the frontal sinus and the ear canals. The derived $R2^+$ is not homogeneous over the whole brain but shows patterns of dominating R2 or R2'.

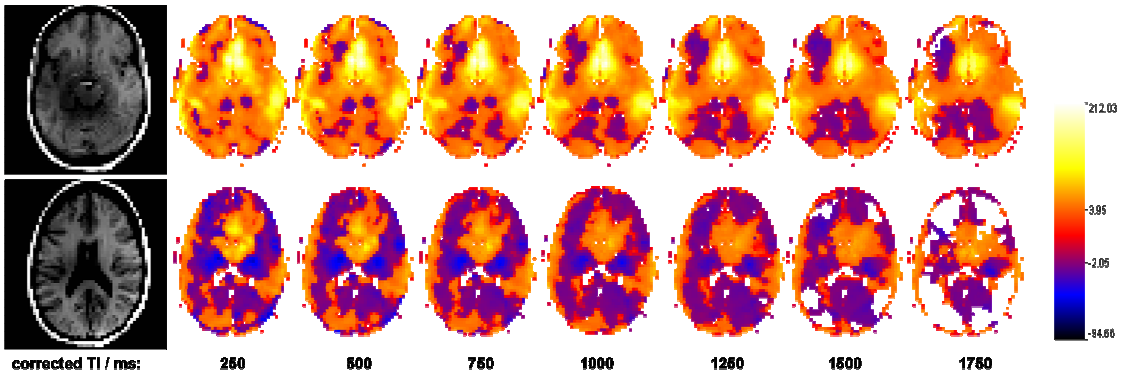

Fig. 54: Typical time series of $R2^+$ values. Two slices are shown. The windowing is chosen such that positive values appear yellow and negative values blue. The data is already corrected for BAT. This leads to the white spots at later time steps where no further signal evolution has been acquired. In the first row, a lower slice has been chosen. High R2' values can be seen in the area of the frontal sinus.

Averages of the temporally preprocessed $R2^+$ data over all relevant time steps are shown in Fig. 55 (3rd row from left). Again, color maps and scaling have been chosen such that zero corresponds to red, negative values appear blue and positive values appear orange to yellow. There is a strong pattern of dominating T2 decay in the areas of the left and right MCA. Also, a lot of tissue areas seem to have stronger T2 decay. While the dominance of susceptibility effects in the frontal sinus area is well known, the unusual high values in the MCA regions strongly point to inflow effects. Because a substantial amount of blood is transported through the voxel, water molecules will experience different local field strengths and might not refocus completely after the refocusing pulse.

Additionally, to investigate the trend of $R2^+$ over TI, a linear regression has been done over all R^+ values on a voxel-by-voxel basis. Maps showing the slope of the linear fits are also shown in Fig. 55 (4th row from left). The colormap and windowing were chosen to show ascending slopes in yellow and declining slopes in blue. For the left and right temporal lobes, a clear upward trend can be seen. In other regions, however, negative slopes dominate.

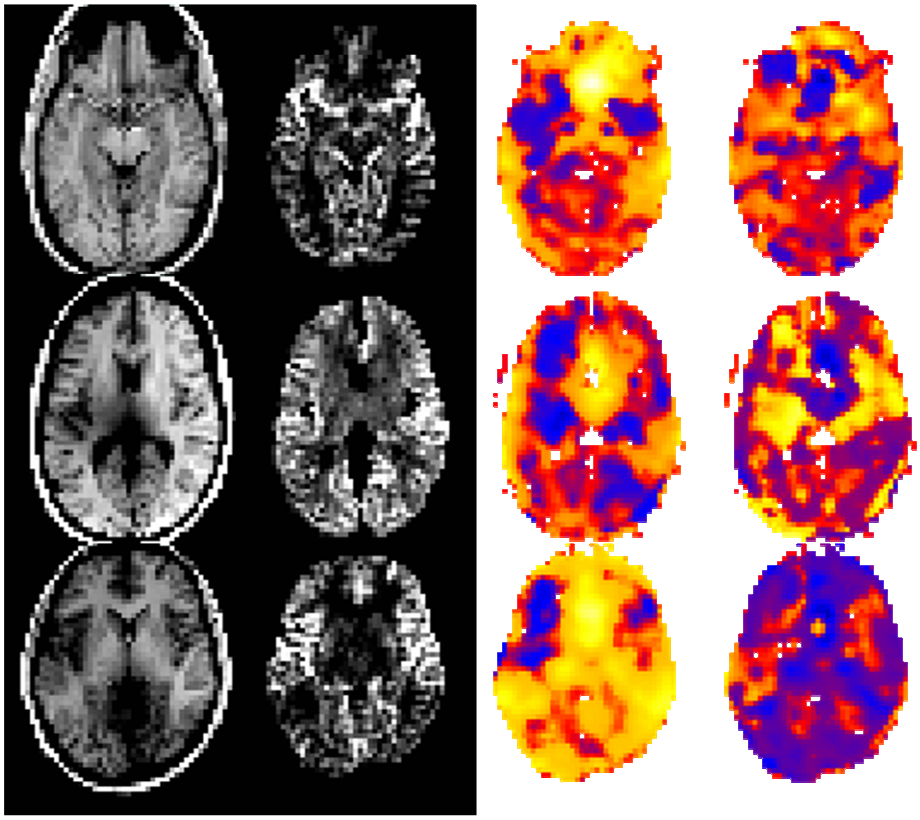

Fig. 55: Typical maps from three subjects; from left to right: T1 weighted anatomical image, ASL fitted perfusion image, $R2^+$ image (yellow: R' dominant), $R2^+$ change over TI (yellow: increase). In the first perfusion image, the MCA and PCA can clearly be seen.

A relative OEF map is shown in Fig. 56 (middle image), and the fitted slopes of temporal OEF development. The OEF values, which are proportional to $R2^+$ (except for an offset), also show an ascending behavior in the right and left MCA areas and the occipital lobe. Fig. 57 shows typical scaled OEF curves and the corresponding perfusion curves of one image slice in one subject. The relative OEF average map shows reasonable values between zero and one for cortical regions in the temporal and occipital lobes. White matter regions appear larger than one, pointing to different underlying $R2$ or ξ values.

The opposing trend is true for large areas of mainly tissue voxel in the lower slices. With ascending inflow time, the T2' governed decay becomes more important relative to T2 relaxation. Under the assumption that flow effects are absent, this could be explained by a larger part of labeled water in the tissue space at later times, where susceptibility is more homogeneous. However, regions with high perfusion potentially correspond to regions with ascending relative OEF (or $R2^+$, cf. Fig. 55). Therefore, values

of relative *OEF* and the trends derived there are more reliable due to SNR consideration.

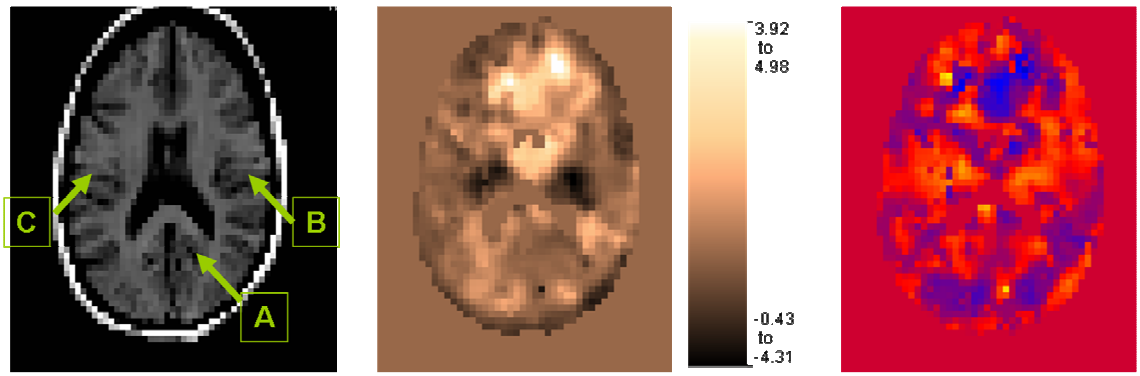

Fig. 56: From left to right: anatomic image, apparent *OEF* averaged over all relevant time steps, linear trend of apparent *OEF* development. Values lie between zero and one in the temporal and occipital lobes and yield reasonable results. In the same areas, the linear regression over TI shows has a positive slope (shown in red).

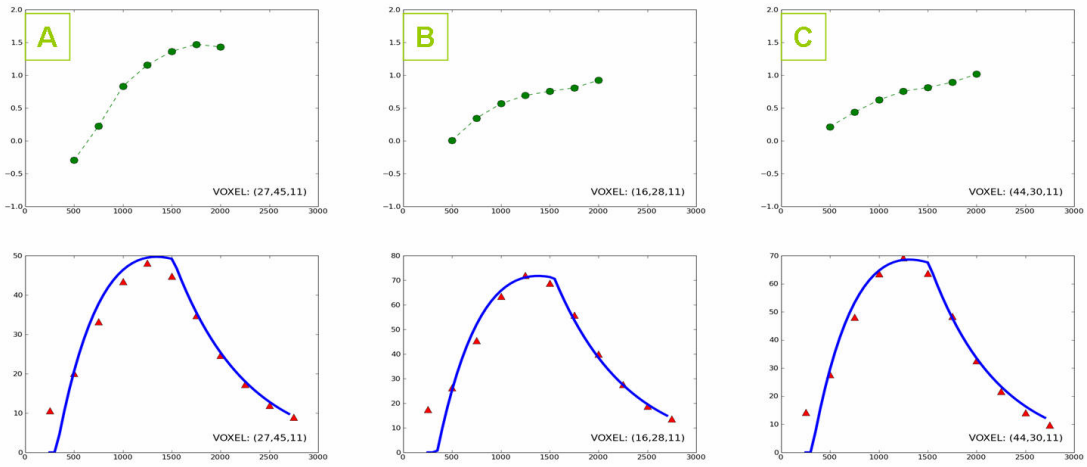

Fig. 57: Typical *OEF* curves (upper) and corresponding inflow curves (lower). *OEF* values are scaled such that zero corresponds to no susceptibility effects due to deoxygenation, and one corresponds to the *OEF* found from the tissue signal. The inflow curves show the perfusion weighted signal. Noise artifacts in the *OEF* estimation are more likely at early and late TI with low SNR.

4.6 Summary

A novel MR imaging sequence, the spin/gradient dual echo double spiral 3D-GRASE, has been developed. It allows the simultaneous acquisitions of a spin and a gradient echo. The readout part is a double spiral-out 3D-GRASE, sampling the spin echo formation with two eco times. Images show good quality and are robust in respect to susceptibility artifacts. The technique has been presented at the ISMRM conference 2009 [Gregori et al. - 2009b].

The presented sequence allows the quantification of R2'. With this parameter, direct information about oxygenation can be derived. The concept relies on the knowledge of R2. With the combination of the technique presented in Ch. 3, the parameter R2 can in principle be acquired simultaneously as well. This would allow a more accurate quantification of the oxygen extraction fraction.

The readout module has been combined with an ASL sequence to map trends of R2' of the perfusion weighted ASL difference signal over inflow time. The rationale was to identify potential susceptibility changes in the direct vicinity surrounding the spins, and thus, getting insight in oxygen consumption dynamics. Although the perfusion signal has very low SNR compared to common anatomic images, the protocol with a measurement time of about 20 minutes yielded stable results. The relaxation rate R2' could be extracted reliably. Possible sources of error have been found, predominantly flow artifacts leading to apparently negative R2' values with the presented acquisition technique. In future experiments, flow artifacts could be suppressed by crusher gradients applied before the readout.

Significant changes in R2' over inflow time TI could be found. However, there is not a clear preference of rising or descending R2'. A rising slope of R2' over TI could point to more deoxygenated hemoglobin in the direct vicinity of the inflowing blood water spins at later TI. There are many regions of rising R2' to be seen in each volume. Some of them can be clearly associated with larger vessel regions, which are prone to flow artifacts especially in early time points. In other areas, descending R2' values can be observed. This could be explained by the fact that the spins diffuse in the tissue space and susceptibility becomes more homogeneous. Still, there are regions which depict the assumed asymptotic relative OEF curve very well. These regions, like temporal and

occipital lobes, show an early blood bolus arrival time and high perfusion values, and therefore large SNR.

Combining the apparent oxygenation of the raw slice selective and non-selective images with the perfusion data, relative oxygenation curves of the inflowing spins could be presented. The hypothesis was that the relative OEF experienced by the inflowing spins starts at zero at low TI, with a rise afterwards up to one compared with the tissue OEF. Such characteristics could be found in well perfused grey matter regions, like in the occipital and temporal lobes.

5 General Summary and Conclusion

Arterial Spin Labeling is by now an important tool in MR imaging and is on the way to get an important role in clinics in the near future. The prospects of ASL are by far not exhausted. The investigation of the ASL signal in respect to the relaxation constants T2 and T2' is an aspect which has not been addressed in detail, so far. These contrasts contain information about physiological aspects like capillary water permeability and oxygenation.

In this work, ASL research has been pushed forward to address these new aspects. The presented results allow deep insight in the underlying physiological mechanisms of blood water transport and oxygen consumption. With these characteristics, they suggest a wide range of clinical applications. The very promising results of the two presented new techniques are a motivation to proceed research in the field of multi-parametric ASL.

5.1 ASL T2: Permeability measurements

An ASL 3D-GRASE sequence has been refined to measure the ASL signal at different echo times TE. This sequence has been used to acquire ASL time series datasets. An analytical model has been derived describing the ASL signal evolution along the echo time axis TE, additional to the inflow time axis TI. Data acquired with the modified readout scheme and preliminary evaluation has been successfully presented at the ISMRM conference 2009 [Gregori et al. - 2009a].

Data evaluation using the proposed model yielded blood water permeability maps of the capillary wall. This is the first technique to derive whole-brain water permeability maps based on ASL T2 measurements. The method could be tested and verified on healthy volunteers. The permeability area surface product found was about 205 ml/100g/min and in the range of values known from PET.

5.2 ASL T2': Oxygenation measurements

A novel spin/gradient dual echo double spiral 3D-GRASE sequence has been developed. The sequence acquires two echo times on a rising edge and on the top of the spin echo, with whole brain coverage in single shot. The data can be used to quantify T2' locally, while the spin echo signal is largely unaffected by susceptibility effects [Gregori et al. - 2009b]. The readout has been combined with an ASL preparation scheme.

ASL time series data sets have been acquired to investigate the dynamic changes of T2' during blood inflow. The rationale was to follow the water molecules on their way through the capillary bed, looking at local susceptibility changes. Quantified T2' could be acquired on an ASL time series measurement. The data showed stable results, verified on healthy volunteers. Clear trends in T2' development over time could be observed, depending on brain region. In the regions with highest SNR, the dominating trend observed was a rise in R2', corresponding to a rising oxygen extraction as the blood flows through the capillary bed. After scaling the OEF values with the pure tissue signal data, reasonable value ranges could be observed, mainly between zero at early time steps (no oxygen extraction) and one (maximal oxygen extraction).

5.3 Outlook: clinical applications

The presented techniques and collected data suggest a wide range of applications. As mentioned in the beginning, blood brain barrier permeability is a crucial factor in many cerebro-vascular diseases, including tumor and multiple sclerosis lesions. By now, dynamic susceptibility contrast is the major diagnosis tool for lesions diagnosis, which accumulate macromolecular contrast agent due to blood brain barrier breakdown. The presented work is a step towards a future possible diagnosis without the necessity of contrast agent.

In the field of functional imaging, BOLD and ASL are both techniques which can be used to investigate brain activation changes. The new technique proposed here can be used to acquire quantified perfusion and T2' values – i.e. BOLD – simultaneously on the same spin echo train. It could therefore be a successful tool in fMRI applications. There, the quantified information can be used to uncouple the perfusion and the oxygenation changes, which both occur during brain activation and are not thoroughly

understood. The simultaneous acquisition promises a better signal to noise ratio because of the temporal correlation of both modalities. Other possible applications lie in the investigation of cerebro-vascular diseases, where the influence on oxygen metabolism can be mapped in affected brain regions.

Appendix A: Physiology

In this chapter a short overview shall be given on the anatomical and physiological backgrounds about the delivery of blood to the brain tissue, the role of diffusion of blood water through the blood brain barrier and the effect of oxygen metabolism on the inflowing blood water signal.

A.1 The vascular tree

Blood is delivered through the neck by three major arterial paths: the Right and the Left Internal Carotid Arteries (ICA) and the Vertebral Artery (Fig. 58). The three arteries deliver about 600 ml blood per min to the brain [Buijs et al. - 1998] where the ICAs support about 40% each and the Vertebralis 20% of the total flow.

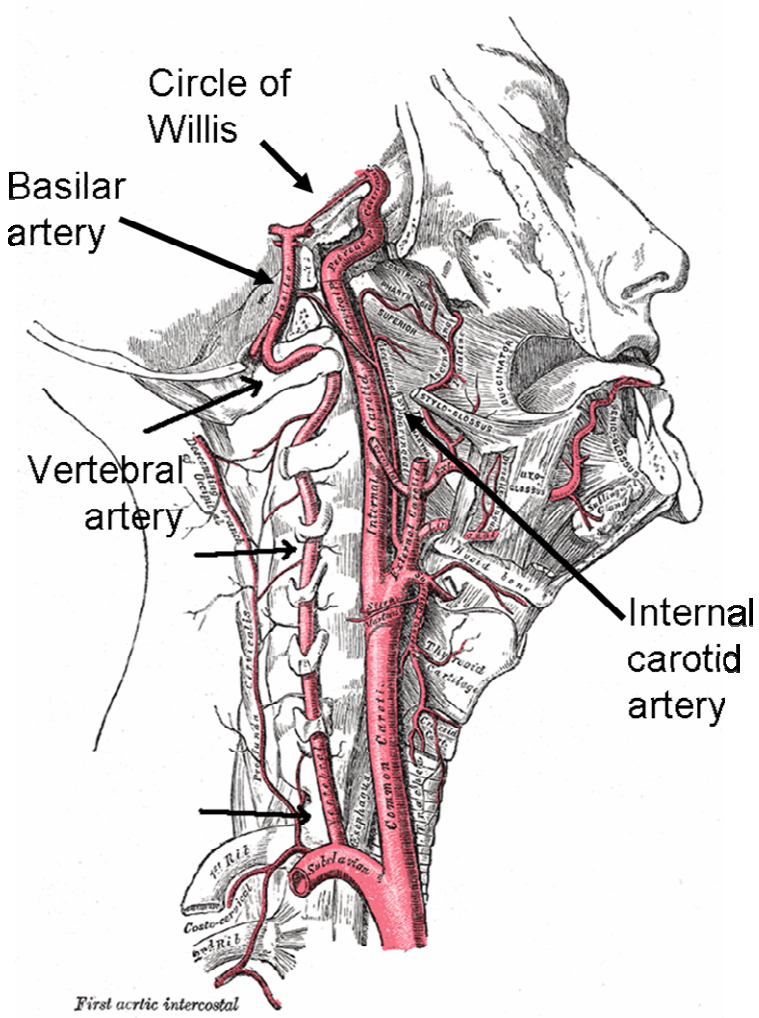

Fig. 58: Arteries of the neck; the right ICA and the Vertebral Artery are interconnected in the Circle of Willis. Image on Wikipedia, from the 20th U.S. edition of Gray's Anatomy of the Human Body, originally published in 1918

The three arteries are connected by the Circle of Willis on the scull base level. Via the Circle of Willis, in case of proximal stenosis or vessel inclusion, blood can be delivered collaterally from the other supplying arteries.

After the Cirle of Willis the ICAs form the left and the right Middle Cerebral Arteries (MCA) and the Vertebral Artery splits up to the Posterior Cerebral Arteries (PCA).

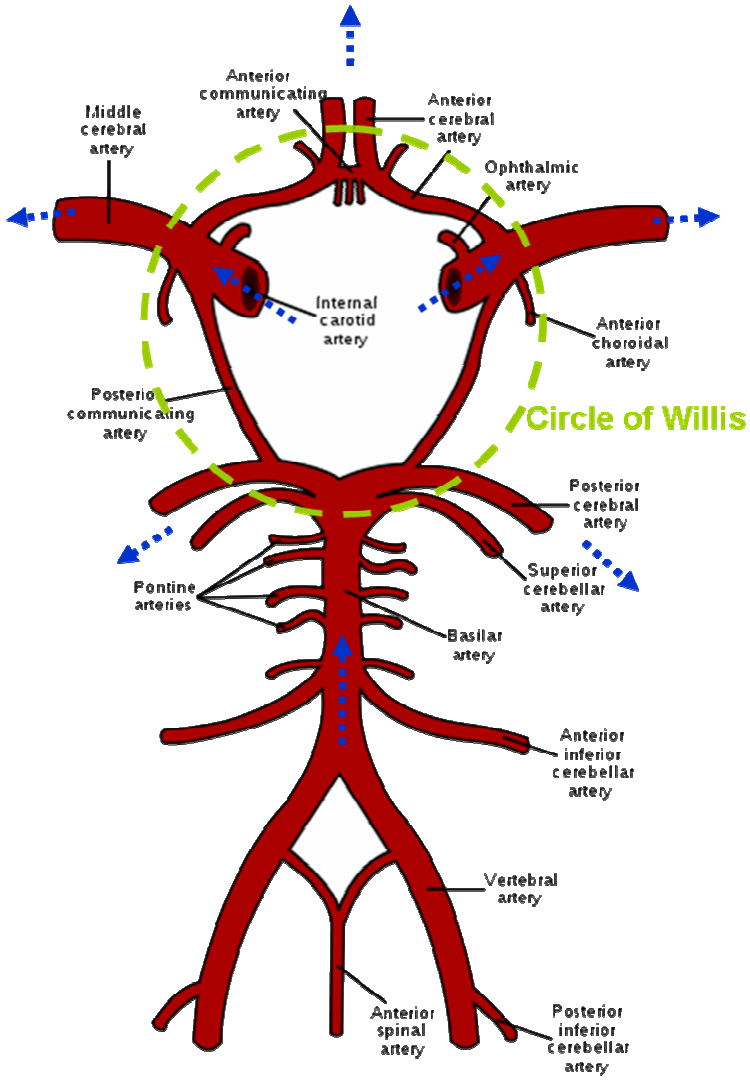

Fig. 59: Schematic diagram of the vascular system around the Circle of Willis. Blood is flowing in through the Vertebral and Basilar arteries and the ICAs. From there it is delivered to the brain by the MCAs and other smaller arteries. Blue dashed arrows indicate blood flow direction. Image from Wikipedia, public domain.

A.2 The Blood Brain Barrier

After passing the arteries and, later on, the smaller arterioles, blood finally reaches the capillary bed. Capillaries are the vessels which penetrate the tissue to deliver nutrients and oxygen to the cells, and to transport off the metabolites and deoxygenated erythrocytes. They are commonly of the size of 5-10 µm in diameter. That is also the diameter of the red blood cells which line up to flow through the capillary one by one.

The capillaries in the central nervous system differ significantly from others: The capillary wall in the brain is surrounded by endothelial cells, connecting to each other with “tight junctions” and thus forming the “blood brain barrier” which restricts the permeability of solables. For many larger molecules it becomes impossible to pass. Smaller hydrophobic molecules like CO_2 or O_2 can pass the blood brain barrier, while for several larger molecules, like glucose, active transport mechanisms exist. Because of their small size, water molecules can pass the blood brain barrier easily.

A.3 Brain tissue

There are two major components which can be distinguished by MRI in the brain: Grey matter and White matter. Grey matter predominantly consists of neural cell bodies connected to each other by axons, dendrites and glia cells. White matter consists of myelated axons which interconnect different areas of grey matter. It is significantly less perfused than Gray matter.

A third modality in the brain which can be distinguished is Cerebrospinal Fluid (CSF). This is the fluid which fills out the ventricles and in the sulci. CSF is a clear fluid, containing approximately 0.3% plasma proteins.

In a typical T1 weighted image, the modalities can be distinguished easily (Fig. 60).

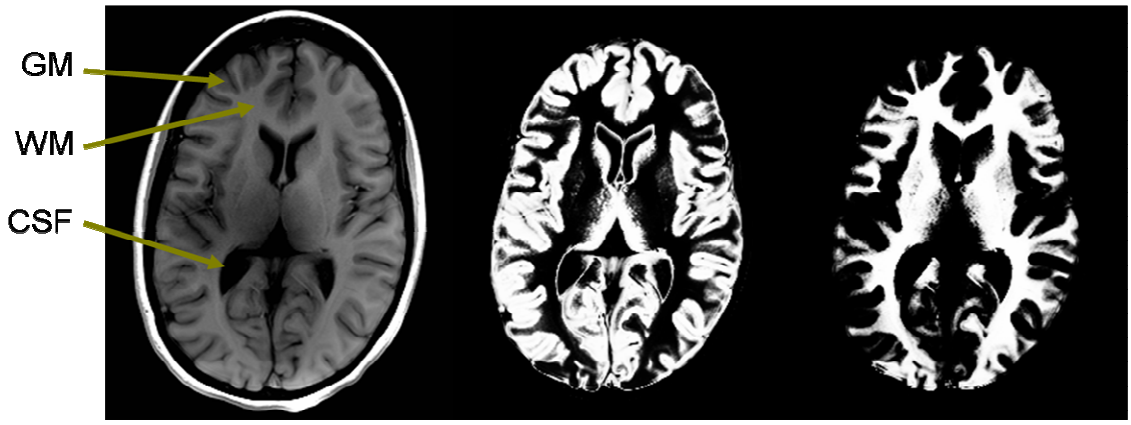

Fig. 60: From left to right: T1 weighted image, segmented Gray matter, segmented White matter. In T1 weighted images, Grey matter appears grey, white matter white, CSF black. Segmentations hve been computed automatically with SPM5 [S – SPM5].

Appendix B: T1, T2 and T2* values

B.1 T1 values

The longitudinal relaxation constant T1 for brain tissue is well investigated and has been published in various articles. T1 can be determined by inversion-recovery experiments. After a 180° inversion, the MR signal is acquired after the "inversion time" TI. The data of several inversion times can be used to calculate T1. T1 depends on the field strength. The following values are for 3 Tesla. Also, there are slight variations of T1 over different brain regions.

Wansapura et.al [Wansapura et al. - 1999] found a T1 average over the brain and several subjects of 832±10 ms for White matter and 1331±13 ms for Gray matter. Clare and Jezzard [Clare, Jezzard - 2001] found a larger range of T1 for Gray matter between 1060 and 1310 ms. The White matter values are in the same range about 850 ms. The values for CSF are much higher, reported here as 3700±500 ms. Stanisz reported unusual high values for Gray matter (1820±114 ms) and White matter (1084±45 ms) [Stanisz et al. - 2005].

T1 / ms at 3T	[Wansapura et al. - 1999]	[Clare, Jezzard - 2001]	[Stanisz et al. - 2005]	[Ethofer et al. - 2003]
Grey matter	1331	~1200	1820	1470
White matter	832	850	1084	1110
CSF		3700		
	[Lu et al. - 2004]	[Greenman et al. - 2003]	[Stanisz et al. - 2005]	
Blood	1526	1550	1932	

Tab. 5: T1 values reported in different publications

ROI	Description	T_1 (msec, ±SE)	T_2 (msec, ±SE)
1	Frontal gray matter	1322 ± 34	110 ± 4
2	Parasagittal frontal gray matter	1392 ± 27	104 ± 2
3	Insular gray matter	1356 ± 33	102 ± 2
4	Parietal gray matter	1276 ± 33	112 ± 4
5	Parasagittal occipital gray matter	1356 ± 29	98 ± 3
6	Occipital gray matter*	1283 ± 37	132 ± 9
7	Frontal white matter*	838 ± 18	74 ± 1
8	Parietal white matter	827 ± 19	80 ± 1
9	Occipital white matter	832 ± 18	84 ± 1

†Relaxation times in nine anatomical regions within the brain, averaged between left and right hemispheres in a total of 36 observations.
*T_2s measured in the ROIs significantly different from the average T_2 for GM or WM, respectively, as established using an ANOVA test. These differences are described in the Discussion section.

Tab. 6: T1 and T2 values from [Wansapura et al. - 1999] regarding different brain regions.

T_1 Measurements in a Set of Grey Matter, White Matter and CSF Regions in the Brain, Obtained From T_1 Maps of 8 Normal Volunteers

Region	T_1 (msec)	Reproducibility %
Centrum semiovale	860 ± 20	1.9
Internal capsule	890 ± 40	3.8
Corpus callosum	820 ± 40	2.8
Thalamus	1060 ± 40	2.2
Putamen	1100 ± 30	2.5
Caudate	1310 ± 60	3.5
Lateral ventricle	3700 ± 500	3.3

Reproducibility measurements are based on 7 independent measurements on a single subject.

Tab. 7: T1 values from [Clare, Jezzard - 2001] regarding different brain regions.

To determine T1 of blood is not as straightforward. Reason for that is the small vessel size which makes partial volume effects inevitable, flow artifacts in the readout, and dependence on other physiological parameters like hematocrit and oxygenation. The most reliable values are obtained in vitro where blood samples are measured in an MR scanner. In [Lu et al. - 2004] bovine blood was used which reportedly has similar properties than human blood. Lu reported arterial (Y=0.99) T1 values of 1526 ms and

venous (Y=0.66) T1 of 1504 ms at 37°C, with errors of 5 ms. As can be seen, there is only a small oxygenation effect on T1.

B.2 T2 values

The transverse relaxation constant T2 is can be assessed in spin echo experiments. After preparation of the transverse magnetization and a refocusing pulse at TE/2, images are acquired on the spin echo at TE. When measuring at different echo times, the signal shows an exponential T2 decay with ascending TE. An effect which complicates T2 measurements is diffusion. Water molecules which diffuse in the time between the preparation pulse and the readout are only refocused if they experience the same local magnetic field. This is not true in reality where there are many sources of local susceptibility change. Especially in cases with large susceptibility inhomogeneities there must be expected an influence not only on T2* but also on T2. This effect however will depend on the time between preparation and readout T2. A “pure” T2 value can therefore be extrapolated.

Reported T2 values also show variations over brain region. Wansapura [Wansapura et al. - 1999] reported 110±2 ms for Gray matter and 79.6±0.6 ms for White matter. Stanisz et.al [Stanisz et al. - 2005] report 99.7±7 and 69±3 ms for Grey and White Matter.

Due to the diffusion effects T2 is much more influenced by oxygenation effects than T1, since deoxygenation is the cause for BOLD susceptibility effect. In T2 blood measurements the oxygen and haematocrit values have to be considered. Lee et al. [Lee et al. - 2003] reported a value of 165.4±3.2 ms for arterial (Y=1) human blood, measured in vitro.

T2 / ms at 3T	[Wansapura et al. - 1999]	[Stanisz et al. - 2005]	[Gelman et al. - 1999]	[Lee et al. - 2003]
GM	110	99.7	71	
WM	79.6	69.3	56	
Blood		(275±50)		165.4±3.2

Tab. 8: T2 values reported in different publications.

B.3 T2* values

T2* is measured in free induction decay (FID) experiments. After preparation of the transverse magnetization, the signal is acquired after the echo time TE. Towards higher echo times, an exponential T2* signal decay is assumed. As a predominantly susceptibility induced effect, T2* values change with local magnetic field changes. This is exploited in BOLD fMRI experiments. Tissue T2* depends on the surrounding vessel's oxygenation and therefore on the local brain activation. Therefore the values given here should be treated with care.

Wasnapura reported 44.7±1.2 and 48.4±4.5 for White matter and 51.8±3.3 and 41.6±2.0 for Grey matter ROIs. Krüger found 49 ms for both GM and WM [Kruger et al. - 2001]. [Blockley et al. - 2008] reported T2*=47ms in vitro (human blood, Y=1).

T2* / ms at 3T	[Wansapura et al. - 1999]	[Kruger et al. - 2001]	[Blockley et al. - 2008]
GM	45.7	49	
WM	46.6	49	
Blood			47

Tab. 9: T2* values reported in different publications

References

Ahn, C. B., J. H. Kim and Z. H. Cho (1986). "High-speed spiral-scan echo planar NMR imaging-I." IEEE Trans Med Imaging **5**(1): 2-7.

Amann, M. (2000). "DREIDIMENSIONALE MAGNETRESONANZ-ANGIOGRAPHIE MIT SPIRALFÖRMIGER AUSLESE (SPIRAL 3D MRA)." Dissertation, Heidelberg University, Department of Physics and Astronomy

An, H. and W. Lin (2000). "Quantitative Measurements of Cerebral Blood Oxygen Saturation Using Magnetic Resonance Imaging." Journal of Cerebral Blood Flow and Metabolism **20**: 1225-1236.

Bernstein, M. A., K. F. King and J. Z. Xiaohong (2004). Handbook of MRI Pulse Sequences.

Blockley, N. P., L. Jiang, A. G. Gardener, C. N. Ludman, S. T. Francis and P. A. Gowland (2008). "Field strength dependence of R1 and R2* relaxivities of human whole blood to ProHance, Vasovist, and deoxyhemoglobin." Magn Reson Med **60**(6): 1313-20.

Botha, C. P. and F. H. Post (2008). "Hybrid scheduling in the DeVIDE dataflow visualisation environment." Proceedings of Simulation and Visualization: 309-322.

Buijs, P. C., M. J. Krabbe-Hartkamp, C. J. Bakker, E. E. de Lange, L. M. Ramos, M. M. Breteler and W. P. Mali (1998). "Effect of age on cerebral blood flow: measurement with ungated two-dimensional phase-contrast MR angiography in 250 adults." Radiology **209**(3): 667-74.

Buxton, R. B., L. R. Frank, E. C. Wong, B. Siewert, S. Warach and R. R. Edelman (1998). "A general kinetic model for quantitative perfusion imaging with arterial spin labeling." Magn Reson Med **40**(3): 383-96.

Buxton, R. B., K. Uludag, D. J. Dubowitz and T. T. Liu (2004). "Modeling the hemodynamic response to brain activation." Neuroimage **23 Suppl 1**: S220-33.

Clare, S. and P. Jezzard (2001). "Rapid T(1) mapping using multislice echo planar imaging." Magn Reson Med **45**(4): 630-4.

Edelman, R. R., B. Siewert, M. Adamis, J. Gaa, G. Laub and P. Wielopolski (1994). "Signal targeting with alternating radiofrequency (STAR) sequences: application to MR angiography." Magn Reson Med **31**(2): 233-8.

Ethofer, T., I. Mader, U. Seeger, G. Helms, M. Erb, W. Grodd, A. Ludolph and U. Klose (2003). "Comparison of longitudinal metabolite relaxation times in different regions of the human brain at 1.5 and 3 Tesla." Magn Reson Med **50**(6): 1296-301.

Gelman, N., J. M. Gorell, P. B. Barker, R. M. Savage, E. M. Spickler, J. P. Windham and R. A. Knight (1999). "MR imaging of human brain at 3.0 T: preliminary report on transverse relaxation rates and relation to estimated iron content." Radiology **210**(3): 759-67.

Greenman, R. L., J. E. Shirosky, R. V. Mulkern and N. M. Rofsky (2003). "Double inversion black-blood fast spin-echo imaging of the human heart: a comparison between 1.5T and 3.0T." J Magn Reson Imaging **17**(6): 648-55.

Gregori, J., M. Günther and N. Schuff (2009a). Assessment of Blood-Brain Water Transfer by Arterial Spin Labeling Based T2 Measurements. Proceedings 17th Scientific Meeting, International Society for Magnetic Resonance in Medicine, Honolulu.

Gregori, J., N. Schuff and M. Günther (2009b). Simultaneous Spin/Gradient Echo Acquisitions in Conjunction with Arterial Spin Labeling For Quantification of T2* by Single Shot 3D Spiral GRASE Imaging. Proceedings 17th Scientific Meeting, International Society for Magnetic Resonance in Medicine, Honolulu.

Günther, M. (2009a). Benefits of Short Bolus ASL. Proceedings 17th Scientific Meeting, International Society for Magnetic Resonance in Medicine, Honolulu.

Günther, M. (2009b). Dispersion of a short ASL bolus along the arterial tree. Proceedings 17th Scientific Meeting, International Society for Magnetic Resonance in Medicine, Honolulu.

Günther, M., K. Oshio and D. A. Feinberg (2005). "Single-shot 3D imaging techniques improve arterial spin labeling perfusion measurements." Magn Reson Med **54**(2): 491-8.

Haacke, E. M., R. W. Brown, M. R. Thompson and R. Venkatesan (1999). Magnetic Resonance Imaging: Physical Principles and Sequence Design.

Hahn, E. (1950). "Spin Echoes." Physical Review Letters **80**: 580.

He, X. and D. A. Yablonskiy (2007). "Quantitative BOLD: mapping of human cerebral deoxygenated blood volume and oxygen extraction fraction: default state." Magn Reson Med **57**(1): 115-26.

Hennig, J. (1988). "Multiecho imaging sequences with low refocusing flip angles." J Magn Res **78**: 397–407.

James, F. and M. Roos (1975). "Minuit: A System for Function Minimization and Analysis of the Parameter Errors and Correlations." Comput. Phys. Commun. **10**: 343-367.

Kim, S. G. (1995). "Quantification of relative cerebral blood flow change by flow-sensitive alternating inversion recovery (FAIR) technique: application to functional mapping." Magn Reson Med **34**(3): 293-301.

Kruger, G., A. Kastrup and G. H. Glover (2001). "Neuroimaging at 1.5 T and 3.0 T: comparison of oxygenation-sensitive magnetic resonance imaging." Magn Reson Med **45**(4): 595-604.

Kwong, K. K., D. A. Chesler, R. M. Weisskoff, K. M. Donahue, T. L. Davis, L. Ostergaard, T. A. Campbell and B. R. Rosen (1995). "MR perfusion studies with T1-weighted echo planar imaging." Magn Reson Med **34**(6): 878-87.

Lee, T., J. A. Stainsby, J. Hong, E. Han, J. Brittain and G. A. Wright (2003). Blood Relaxation Properties at 3T -- Effects of Blood Oxygen Saturation. Proc. Intl. Soc. Mag. Reson. Med. 11.

Li, K. L., X. Zhu, N. Hylton, G. H. Jahng, M. W. Weiner and N. Schuff (2005). "Four-phase single-capillary stepwise model for kinetics in arterial spin labeling MRI." Magn Reson Med **53**(3): 511-8.

Lu, H., C. Clingman, X. Golay and P. C. van Zijl (2004). "Determining the longitudinal relaxation time (T1) of blood at 3.0 Tesla." Magn Reson Med **52**(3): 679-82.

Mansfield, P. and A. A. Maudsley (1977). "Medical imaging by NMR." Br J Radiol **50**(591): 188-94.

Ogg, R. J., P. B. Kingsley and J. S. Taylor (1994). "WET, a T1- and B1-insensitive water-suppression method for in vivo localized 1H NMR spectroscopy." J Magn Reson B **104**(1): 1-10.

Oshio, K. and D. A. Feinberg (1991). "GRASE (Gradient- and spin-echo) imaging: a novel fast MRI technique." Magn Reson Med **20**(2): 344-9.

Parkes, L. M. (2005). "Quantification of cerebral perfusion using arterial spin labeling: two-compartment models." J Magn Reson Imaging **22**(6): 732-6.

Parkes, L. M. and P. S. Tofts (2002). "Improved accuracy of human cerebral blood perfusion measurements using arterial spin labeling: accounting for capillary water permeability." Magn Reson Med **48**(1): 27-41.

Petersen, E. T., I. Zimine, Y. C. Ho and X. Golay (2006). "Non-invasive measurement of perfusion: a critical review of arterial spin labelling techniques." Br J Radiol **79**(944): 688-701.

Purves, M. J. (1972). The Physiology of the Cerebral Circulation.

Raichle, M. E., W. R. Martin, P. Herscovitch, M. A. Mintun and J. Markham (1983). "Brain blood flow measured with intravenous H2(15)O. II. Implementation and validation." J Nucl Med **24**(9): 790-8.

Slichter, C. P. (1978). Principles of Magnetic Resonance, Springer-Verlag Berlin Heidelberg New York.

St Lawrence, K. S., J. A. Frank and A. C. McLaughlin (2000). "Effect of restricted water exchange on cerebral blood flow values calculated with arterial spin tagging: a theoretical investigation." Magn Reson Med **44**(3): 440-9.

Stanisz, G. J., E. E. Odrobina, J. Pun, M. Escaravage, S. J. Graham, M. J. Bronskill and R. M. Henkelman (2005). "T1, T2 relaxation and magnetization transfer in tissue at 3T." Magn Reson Med **54**(3): 507-12.

Thomas, D. L., M. F. Lythgoe, F. Calamante, D. G. Gadian and R. J. Ordidge (2001). "Simultaneous noninvasive measurement of CBF and CBV using double-echo FAIR (DEFAIR)." Magn Reson Med **45**(5): 853-63.

Tofts, P. (2003). Quantitative MRI of the Brain.

Wang, J., M. A. Fernandez-Seara, S. Wang and K. S. St Lawrence (2007). "When perfusion meets diffusion: in vivo measurement of water permeability in human brain." J Cereb Blood Flow Metab **27**(4): 839-49.

Wansapura, J. P., S. K. Holland, R. S. Dunn and W. S. Ball, Jr. (1999). "NMR relaxation times in the human brain at 3.0 tesla." J Magn Reson Imaging **9**(4): 531-8.

Wells, J. A., M. F. Lythgoe, M. Choy, D. G. Gadian, R. J. Ordidge and D. L. Thomas (2009). "Characterizing the origin of the arterial spin labelling signal in MRI using a multiecho acquisition approach." J Cereb Blood Flow Metab **29**(11): 1836-45.

Williams, D. S., J. A. Detre, J. S. Leigh and A. P. Koretsky (1992). "Magnetic resonance imaging of perfusion using spin inversion of arterial water." Proc Natl Acad Sci U S A **89**(1): 212-6.

Yablonskiy, D. A. and E. M. Haacke (1994). "Theory of NMR signal behavior in magnetically inhomogeneous tissues: the static dephasing regime." Magn Reson Med **32**(6): 749-63.

Yablonskiy, D. A. and E. M. Haacke (1997). "An MRI method for measuring T2 in the presence of static and RF magnetic field inhomogeneities." Magn Reson Med **37**(6): 872-6.

Software References

References to software programs and toolkits

[S - DeVIDE]:
http://graphics.tudelft.nl/Projects/DeVIDE

[S - Gnuplot]:
http://www.gnuplot.info/

[S – ITK]:
http://www.itk.org

[S - MAPLE]:
http://www.maplesoft.com/products/Maple/

[S - Minuit]:
http://lcgapp.cern.ch/projects/cls/work-packages/mathlibs/minuit/home.html

[S - Python]
http://www.python.org

[S – SPM5]:
http://www.fil.ion.ucl.ac.uk/spm

[S – VTK]
http://www.vtk.org

Acknowledgements

A lot of people have contributed to this work and I am grateful for all the support that I received. The first one to thank is my supervisor Matthias Günther, who gave me the opportunity to write my thesis in his group and guided me through the last three year's work with competence and ingenious ideas. Second, thanks to Prof. Bille who didn't hesitate to support me as referee. Special thanks to Prof. Hennerici of the University Hospital Mannheim, who provided me a position in his group at the Department of Neurology. His special interest in MR Physics led to hosting a Physics group at his department. During my six months stay in San Francisco, it was Norbert Schuff of the University of California San Francisco, who supported me a lot and always had time and enthusiasm to discuss the advance of our projects: thank you! And thanks to PhD André Bongers who always had an open ear for me when I had no clue on MRI in the beginning.

Thank you to all my colleagues in Mannheim at the University Hospital! Especially to Christina and Achim with whom I shared my workspace and who were accountable for a really enjoyable working atmosphere! Thanks to Rolf and Kristina, and Petra, and all the colleagues in the MR group, who helped me with my research! Especially, thanks to my colleagues and friends Marc and Martin, also for any support other than work.

Thanks to all the crew of the mediri GmbH in Heidelberg! Again to my boss and supervisor Matthias and to executive vice-president André; to our more-than-committed secretary Alice; and to Yo-Huong, Jürgen and Joe: You made Heidelberg an even nicer place to come to! Many thanks also to our external colleagues in Basel, Michael and Jochen, for the fruitful collaboration.

And at last, not least, thanks to all Diploma students and fellow PhD students, for helpful discussions at work and at lunch, and for being there and sharing my fate: to Ina, Natascha and Sofie; and lately, to Nuria and Johanna: it has been and is really fun working with you!